NEW ALGORITHMS FOR OCEAN SURFACE WIND RETRIEVALS USING MULTI-FREQUENCY SIGNALS OF OPPORTUNITY

A Dissertation

Submitted to the Faculty

of

Purdue University

by

Han Zhang

In Partial Fulfillment of the

Requirements for the Degree

of

Doctor of Philosophy

May 2019

Purdue University

West Lafayette, Indiana

THE PURDUE UNIVERSITY GRADUATE SCHOOL
STATEMENT OF DISSERTATION APPROVAL

Dr. James L. Garrison, Chair

School of Aeronautics and Astronautics

Dr. Derek M. Burrage

Naval Research Laboratory

Dr. Authur E. Frazho

School of Aeronautics and Astronautics

Dr. David J. Love

School of Electrical and Computer Engineering

Approved by:

Dr. Weinong Chen

Head of the School Graduate Program

ACKNOWLEDGMENTS

I would like to first extend my sincerest gratitude to my advisor, Professor James L. Garrison, for your guidance and support during my PhD journey. You gave me the chance to come to Purdue and work on the cutting-edge remote sensing technologies. I really appreciate all the opportunities you provided to fund my studies and all the exciting research projects you got me involved. Thank you for your invaluable insight on my research. I'm also truly grateful for the opportunities you offered me to attend various international conferences and research meetings, which gave me the chance to communicate with world-leading experts and present my research on a global stage. Thank you Professor Garrison, I completely enjoyed my time at Purdue and I'm profoundly grateful for all you have done for me.

In addition, I would like to thank my committee member, Derek Burrage, a kind research collaborator who is always ready to give a hand whenever needed. It was really a great time working with you on our flight experiments. I have learned a lot from you about radiometry and oceanography. I would also like to thank you for your help in editing all kinds of my manuscripts. Your guidance is an indispensable part for my success in obtaining the PhD degree. Besides, I would also like to thank my other committee members, Professor Arthur Frazho and Professor David Love, for their questions and comments which helped clarify and improve every detail of my work. I would also like to thank my lab mates, Priyankar Bhattacharjee, Jared Douglas, Soon Chye Ho, Feixiong Huang, Seho Kim, Abi Komanduru, Phillip Lipinski and Benjamin Nold for all of their help.

Finally, I would like to thank my parents, Shishun Zhang and Guiping Wang, for their endless love and encouragement. I'm grateful for all their support of my academic endeavor. Their guidance and advice helped me grow up to be an upright and brave person who keeps following his dreams.

TABLE OF CONTENTS

Page

Page

LIST OF TABLES

LIST OF FIGURES

Figure Page

ABSTRACT

Zhang, Han Ph.D., Purdue University, May 2019. New Algorithms for Ocean Surface Wind Retrievals Using Multi-Frequency Signals of Opportunity. Major Professor: James L. Garrison Professor.

Global Navigation Satellite System Reflectometry (GNSS-R) has presented a great potential as an important approach for ocean remote sensing. Numerous studies have demonstrated that the shape of a code-correlation waveform of forward-scattered Global Positioning System (GPS) signals may be used to measure ocean surface roughness and related geophysical parameters such as wind speed. Recent experiments have extended the reflectometry technique to transmissions from communication satellites. Due to the high power and frequencies of these signals, they are more sensitive to smaller scale ocean surface features, which makes communication satellites a promising signal of opportunity (SoOp) for ocean remote sensing. Recent advancements in fundamental physics are represented by the new scattering model and bistatic radar function developed by Voronovich and Zavorotny based on the SSA (Small Slope Approximation). This new model allows the partially coherent scattering in low wind conditions to be correctly described, which overcomes the limitations of diffuse scattering inherited in the conventional KA-GO (Kirchhoff Approximation-Geometric Optics) model. Furthermore, exploration and practice using spaceborne platforms have become a primary research focus, which is highlighted by the launch of CYGNSS (Cyclone Global Navigation Satellite System) in 2016. CYGNSS is a NASA (National Aeronautics and Space Administration) Earth Venture Mission consisting of an 8 micro-satellite constellation of GNSS-R instruments designed to observe tropical cyclones.

However, in spite of the significant achievements made in the past 10 years, there are still a variety of challenges to be addressed currently in the ocean reflectometry

field. To begin with, the airborne demonstration experiments conducted previously for S-band reflectometry provided neither sufficient amount of data nor the desired scenarios to assess high wind retrieval performance of S-band signals. The current L-band empirical model function theoretically does not also apply to S-band reflectometry. With respect to scattering models, there have been no results of actual data processing so far to verify the performance of the SSA model, especially on low wind retrievals. Lastly, the conventional model fitting methods for ocean wind retrievals were proposed for airborne missions, and new approaches will need to be developed to satisfy the requirement of spaceborne systems.

The research described in this thesis is mainly focused on the development, application and evaluation of new models and algorithms for ocean wind remote sensing. The first part of the thesis studies the extension of reflectometry methods to the general class of SoOps. The airborne reception of commercial satellite S-band transmissions is demonstrated under both low and high wind speed conditions. As part of this effort, a new S-band geophysical model function (GMF) is developed for ocean wind remote sensing using S-band data collected in the 2014 NOAA (National Oceanic and Atmospheric Administration) hurricane campaign. The second part introduces a dual polarization L- and S-band reflectometry experiment, performed in collaboration with Naval Research Lab (NRL), to retrieve and analyze surface winds and compare the results with CYGNSS satellite retrievals and NOAA data buoy measurements. The problems associated with low wind speed retrieval arising from near specular surface reflections are studied. Results have shown improved wind speed retrieval accuracy using bistatic radar cross section (BRCS) modeled by the SSA when compared with KA-GO, in the cases of low to medium diffuse scattering. The last part focuses on the contributions to the NASA-funded spaceborne CYGNSS project. It shows that the accuracy of CYGNSS ocean wind retrieval is improved by an Extended Kalman Filter (EKF) algorithm. Compared with the baseline observable methods, preliminary results showed promising accuracy improvement when the EKF was applied to actual CYGNSS data.

1. INTRODUCTION

Wind is the movement of air and it is driven primarily by the difference between high and low atmospheric pressure systems. Over land, anemometers are used extensively to measure the surface wind speed and direction. But over ocean, measurements of surface wind using such techniques are much more limited, and are primarily obtained from instruments installed at weather stations, on ships, and on buoys. Since the ocean regions are so large, knowledge of the wind characteristics over this vast space is important to weather forecasting, ocean navigation, and climate study. Sustained efforts over recent decades have led to the development of ocean surface remote sensing and wind speed retrieval using microwaves, with the two primary types of instruments being the active microwave scatterometer and the passive microwave radiometer. These have been demonstrated during a series of satellite missions including ASCAT, WindSat, etc.

Global Navigation Satellite System Reflectometry (GNSS-R) measurements have been made within hurricanes for over 10 years. The technique utilizes the fundamental relationship between surface roughness and the spread of the delay-Doppler map (DDM). Assuming a normal distribution of sea surface slope, this roughness is typically parameterized as mean square slope (MSS). Such a relationship between the DDM and MSS has been presented in previous studies [1]. Normally, MSS is obtained by inverting the reflectometry model and then converted to wind speed using empirical models or wave spectrum models. Garrison and Katzberg first demonstrated from an aircraft experiment that the GNSS signal reflections can sense ocean surface roughness and related wind conditions [2]. After that, GNSS-R bistatic radars have been tested in more elaborate campaigns conducted using aircraft [3] [4], stratospheric balloons [5], and even spacecrafts [6] [7]. The most recent and influential spaceborne campaign commenced with the launch of the CYGNSS constellation in 2016, which is

aimed at monitoring the tropical cyclones around the globe using reflectometry techniques [8]. Recent experiments have extended the reflectometry technique to utilize reflected communication satellite transmissions [9]. The higher power of these transmissions and their use of higher frequencies, which may show a stronger sensitivity to smaller scale ocean surface features, makes communication satellites a promising source of signals of opportunity for ocean remote sensing.

There have also been different models developed to relate ocean surface wind speed to MSS. The Cox and Munk model is an empirical model for the relationship between MSS and wind speed developed by analyzing the scattering distribution of sunlight over the ocean surface [10]. The MSSs of both upwind and crosswind directions are modeled as linear functions of the wind speed with a range of validity of 1-14 m/s. Elfouhaily et al. presented a refined wavenumber spectrum model to represent the ocean surface for wind-generated seas [11]. Wind retrieval results from the GNSS-R experiments were also used to develop an empirical model function relating the mean square slope (MSS) to the surface in situ wind speed [12] [13]. This relationship is expressed as a modification to the classical Cox and Munk equation. These observations, which showed sensitivity of GNSS-R retrievals to wind speeds above 40 m/s, were an important foundation for the NASA CYGNSS mission [8].

However, most of the previous experiments were conducted using only L-band GPS signals and based on the widely used KA-GO (Kirchhoff Approximation-Geometric Optics) scattering model which only works for diffuse scattering. The model fitting method was also developed specifically for airborne missions. The unique features of a spaceborne platform, such as CYGNSS, require the development of new retrieval approaches. Therefore, in my research I have focused on analyzing and solving the problems arising from these three aspects of the ocean reflectometry fields: (1) new frequency: assessing the performance of S-band (2.3 GHz) reflectometry for high wind retrievals and developing an S-band geophysical model function; (2) new model: applying the new SSA model to improve low wind retrieval; (3) new algorithm: applying

an EKF-based multi-look DDM processing method to CYGNSS wind speed retrieval. The following sections in this chapter will introduce more details of the three topics.

1.1 Geophysical Model Function

Results from previous GNSS-R experiments have been used to develop an L-band empirical GMF relating the mean square slope (MSS), a measure of surface roughness or sea state, to the surface wind speed. Recent experiments have extended the reflectometry technique to communication satellite transmissions. The higher power of these transmissions and their use of higher frequencies, which may show a stronger sensitivity to smaller scale ocean surface features, make communication satellites a promising source of signals of opportunity for ocean remote sensing. These transmissions also typically have a transmitted power (Effective Isotropic Radiated Power, EIRP) orders of magnitude larger than GNSS (68.5 dBW vs. 26.25 dBW). [9] showed the first demonstration of reflectometry using S-band communication satellite for measuring ocean surface wind. [14] presented the preliminary results from the S-band data collected during the 2014 hurricane season. The existing L-band (GNSS) empirical model function was applied to produce estimates of wind speed, showing the sensitivity of S-band reflectometry measurements to surface winds up to 40-45 m/s.

However, there are currently no existing empirical models developed for S-band reflectometry. The preliminary result in [14] showed certain discrepancies between S-band retrieval and in situ wind speed when applying the L-band model function, and improvement in retrieval accuracy can be expected with a refined model function for S-band. So, the purpose of our work is to present the development of an S-band geophysical model function to characterize the observed MSS at S-band wavelengths as a function of wind speed. Chapter 4 first reviews the 2014 NOAA hurricane campaign and the results. It then details the model development procedures where SFMR was used as the in situ truth. Two different model functions were used to fit

the low wind speed and high wind speed regions. It is shown that with the properly fitted model function, the S-band wind speed retrievals match remote wind speed measurements from other sources. The evaluation of the model by SFMR, HWRF and GPS dropsonde wind speed measurement is presented as well. This confirms the accuracy of the geophysical model at S-band.

1.2 Scattering Model Evaluations

The most widely used bistatic scattering models for GNSS-R are developed under KA-GO, which is only valid for strong diffuse scattering which occurs with a large Rayleigh parameter (roughness scale much larger than the E-M wavelength). Such models give incorrect results for low to medium diffuse scattering that exhibits small Rayleigh parameters. A new scattering model and bistatic radar function was thus developed by Voronovich and Zavorotny using SSA. This allows the transition from partially coherent scattering to completely non-coherent, diffuse scattering to be correctly described [15] [16]. Our goal is to apply the SSA model to actual airborne data and compare the result with retrievals obtained with KA-GO model to evaluate the performance of the new scattering model, especially under low wind speed conditions.

Chapter 5 provides details of the work we have done on application and evaluation of the SSA scattering model. It first presents results from two recent airborne campaigns; the first from March 5-12, 2016 off Maine and the second from May 6-11, 2017 off North and South Carolina. The experiments measured S-band (SDARS) and L-band (GPS) reflections simultaneously in both left and right circular polarization. A reflectometry model based on KA-GO is first used to fit the observed DDMs and estimate MSS. Wind speeds are retrieved from MSS using a published empirical L-band model and our proposed S-band model, which are then compared to in situ buoy observations and, in 2017, with CYGNSS wind speed retrievals. Agreements between wind speed measurements from the aircraft, CYGNSS, and nearby buoys are generally close, but low elevation retrievals showed a strong correlation with flight di-

rection. This is likely due to strong variations in antenna gain pattern with respect to azimuth and elevation at low elevation angles. Possible solutions to this problem are attempted and results are discussed. Chapter 5 then focuses on wind speed retrievals using the SSA model. Elfouhailys model is adopted as the ocean wave spectrum model. Results with KA-GO and SSA are compared for low wind speed scenarios (<5m/s). This shows that, due to the presence of coherent components, the SSA model produced lower wind speed retrievals in low to medium diffuse scattering conditions. In comparisons with NOAA buoy ground truth data, the SSA model achieved better agreement in low wind retrievals than the KA-GO model for both the L- and S-band reflectometry data.

1.3 Wind Speed Retrieval Algorithms for Spaceborne Missions

Over the past 20 years, a significant amount of effort has been devoted to the demonstration and evaluation of the GNSS-R technique using airborne platforms such as balloon and aircraft. These experiments have shown that the shape of the DDM is related to the roughness of the scattering surface. The launch of CYGNSS in 2016 has opened a new era of spaceborne reflectometry. CYGNSS is a NASA Earth Venture Mission consisting of an 8 micro-satellite constellation of GNSS-R instruments. Compared with airborne missions, spaceborne platforms have great advantages including the abilities to provide global coverage and near real-time data products. Furthermore, as autonomous systems, spaceborne platforms need less direct control and are thus more efficient to operate. However, spaceborne GNSS-R measurements of ocean winds also present challenges. In contrast to airborne measurements, the surface wind speed cannot be assumed uniform over the large glistening zone the much higher satellite altitude. As a result, information on multiple wind speed parameters is contained in one DDM, in contrast to a single wind speed parameter in airborne cases. This greatly complicates the inversion of the delay-Doppler map (DDM). New efficient approaches had to be explored for a spaceborne mission, which has strict

time constraints on data processing and product release. One such new approach is the observable method, which derives an observable that is easily computed from samples of the DDM that are shown to have a dependence on the surface wind speed. However, the resolution requirement (25 km in the present study) also limits the usable range of delay and Doppler to only a few samples around the specular point. Baseline wind retrieval algorithms for the CYGNSS estimate a single wind speed, representative of the average conditions within a 25 km resolution cell, using only a small fraction of the DDM (15 out of 187 available delay-Doppler pairs).

In [17], a new method is presented to invert the complete delay-Doppler map (DDM), generating estimates of the wind field within a swath defined by the maximum DDM extent. An extended Kalman filter (EKF) is applied, exploiting the large overlap between sequential DDMs, to estimate the wind speed on a uniformly-gridded ocean surface of observables computed from a set of DDM samples at discrete delay-Doppler coordinates. A batch size of 7 DDMs was found to work best, assuming they measure the same wind field in the glistening zone of the 4th DDM. The state vector is a set of 10 km gridded wind speeds defined in the specular frame on an area of the ocean surface that covers the iso-range ellipses of the 4th DDMs. The calibrated DDMs are provided along with associated meta-data such as direct GNSS signal power, orbit geometry and the antenna gain pattern. Simulated retrievals obtained at the specular point using this method met the CYGNSS measurement requirements and performed better than the baseline algorithms. The 0.1 degree resolution winds also met these requirements for low winds (< 20 m/s) within a swath of 90 km, and for hurricane force winds (> 30 m/s) within 22 km.

Chapter 6 shows that the EKF algorithm has been successfully applied to the actual CYGNSS data and the wind speed retrieval results have demonstrated that the EKF approach substantially improves the wind speed estimation accuracy especially in high wind scenarios. Modification of the EKF algorithm for actual CYGNSS data processing is presented, including the redefined state vectors in latitude and longitude frame, instead of the specular frame used in [17]. Accurate ancillary information

measured and provided by the CYGNSS system, such as specular point locations, antenna gain patterns, GPS EIRP and data quality flags were incorporated into the EKF processing. For statistical analysis, fourteen selected CYGNSS data tracks were processed covering wind speeds up to 40 m/s. For about 80% of the data set categorized as good cases, EKF achieved a mean bias of 0.84 m/s and RMS error of 3.03 m/s, while the two CYGNSS baseline algorithms obtained mean biases higher than 2 m/s and RMSs higher than 4 m/s. It is shown that the new v2.1 antenna pattern improves the retrieval accuracy when compared to the previous version.

2. OCEAN SURFACE WIND RETRIEVALS USING SIGNALS OF OPPORTUNITY

This chapter gives an overview of ocean surface wind retrievals using SoOp in Section 2.1. It then explains the fundamental measurement that is explored in this dissertation in Section 2.2.

2.1 History of Ocean Surface Wind Retrievals Using Signals of Opportunity

Remote sensing of ocean surface wind is a very important tool for the modeling of atmosphere and weather. Several methods have been developed for ocean wind remote sensing using microwave signals, for example, scatterometry and radiometry. One of the methods developed in the last 20 years is reflectometry using signals of opportunity. Reflectometry utilizes the microwave signals reflected off the ocean surface to obtain valuable surface roughness and wind speed information. This technique usually involves a bistatic radar configuration where the transmitter and receiver are separated spatially. The transmitted signal is usually designed for other purposes (such as communication or navigation). Then, a receiver is deployed to re-use these signals for remote sensing purposes. These existing signals are referred to as "signals of opportunity".

The idea of reflectometry was first proposed in 1993. In order to obtain the measurement of ocean surface height , a new concept for bistatic altimetry that uses Global Positioning System (GPS) signals reflected from the sea surface was formulated by Martin-Neira [18]. The European Space Agency (ESA) initialized this project to develop the Passive Reflectometry and Interferometry System (PARIS), which is a wide swath altimeter that receives direct and ocean-reflected signals from several GPS

satellites. Ground-based experiments were also conducted to examine the sensitivity of GPS signals [19]. Since then, a variety of experiments have been conducted in this area exploring a variety of applications including remote sensing of ocean surface wind.

The next few subsections introduce some of the relevant work done in the area of remote sensing of ocean surface wind using reflectometry. Section 2.1.1 describes airborne reflectometry and relevant scattering modeling work, and Section 2.1.2 describes spaceborne reflectometry.

2.1.1 Airborne Reflectometry

Garrison et al. conducted the first airborne ocean reflectometry experiment in 1998 [2] and the results proved that the shape of the correlation waveform of reflected GPS signals contains valuable information about the ocean surface roughness, which can be used to retrieve ocean surface wind speed. Soon after that, more elaborate aircraft and balloon experiments were conducted using GNSS-R to measure wind speed and wind vector above rough seas [4] [20] [21].

The retrieval algorithm used a theoretical bistatic radar equation which related the correlation waveforms to MSS and wind speed [1]. This model was derived based on the geometric optics limit of the Kirchhoff approximation. The waveform depends on a wave-slope probability density function, which in turn depends on the wind speed. This provides a physical basis for ocean reflectometry. A significant amount of GPS reflection data was collected during multiple flights on the NOAA "hurricane hunter" aircraft through tropical cyclones in 2004 [12]. An L-band empirical model was development from the data set, which related MSS to wind speed over a wide range of wind speeds.

Recent airborne experiments have extended the reflectometry technique to utilize communication satellite transmissions [9]. The higher power of these transmissions and their use of higher frequencies, which may show a stronger sensitivity to smaller

scale ocean surface features, makes communication satellites a promising source of "signals of opportunity" for ocean remote sensing. Unlike GNSS signals which have their baseband signals defined by a pseudo-random noise (PRN) code that is available for users, reflectometry with other signals of opportunity usually relies on the cross-correlation between direction and reflected signals. An improved version of scattering model and bistatic radar equation has recently been developed using the small slope approximation, which assumes a much wider range of surface scattering and kinematic regimes than the previous model [15] [16].

2.1.2 Spaceborne Reflectometry

Several spaceborne experiments have also been conducted. The processing of signals collected on the Space Shuttle during the Spaceborne Imaging Radar (SIR-C) mission first demonstrated the reception of reflected GPS signals in space [6]. The first intentional spaceborne GNSS-R experiment was conducted during the UK Disaster Monitoring Constellation mission (UK-DMC) in 2004. A number of GPS reflections have since been observed from the satellite [7]. The feasibility of spaceborne reflectometry for Earth remote sensing was demonstrated in [22] [23] [24] [25], and remote sensing of ocean surface wind using this technique was validated in [26]. Spaceborne reflectometry was further studied using the measurements of TechDemoSat-1 launched in 2014 [27].

Finally, the technology is being rapidly developed with the launch of NASA's Cyclone GNSS (CYGNSS) mission in 2016 [28]. CYGNSS is the first NASA Earth science mission to use a constellation of 8 small satellites. Its primary science objective is the measurement of wind speed in hurricanes and tropical cyclones. The goal is a better understanding and improved forecasting of hurricane formations. Measurements are made of Global Positioning System (GPS) navigation signals reflected from the Earth surface. The baseline Level 2 retrieval algorithm uses developed GMFs to map the DDM observables to estimated wind speed [29]. In this algorithm, the sea

state was divided into two different regimes "fully developed sea" (FDS) and "young sea limited fetch" (YSLF). The fully developed sea is independent of the wind forcing extent (fetch) and duration, and then the limited fetch sea is typical for situations with varying wind speed and direction, such as in hurricanes.

2.2 Fundamental Measurement

The fundamental principle of measuring ocean surface roughness with reflectometry is based on fitting a scattering model to the delay-Doppler map (DDM), which is generated through the cross-correlation of the transmitted signal, $s(t)$, and the reflected signal, $s_r(t)$.

$$|Y(\tau, f_c; P_{\vec{v}})|^2 = |\frac{1}{T_i}\int_{T_i} s(t)s_r^*(t-\tau, f_c)dt|^2 \tag{2.1}$$

at delays, τ, and Doppler frequencies, f_c. For GPS, the tranmitted signal can be generated locally in the receiver. However, for communication satellites, the transmitted data bits are not known a priori, so the direct signal is used as the reference in place of locally generated code. The reflected signal and reference signal are cross-correlated over increments in Doppler frequency. The fundamental measurement is the cross-correlation power vs. delay and Doppler, or delay-Doppler map (DDM), which is demonstrated as being dependent on the probability density function (PDF) of the slopes of the sea surface, $P_{\vec{v}}$. The PDF can be estimated by matching the the DDM shape to a scattering model, which takes the form of a convolution [30]:

$$\langle Y^2(\tau, f_c; P_{\vec{v}})\rangle = |\Lambda^2(\tau)| * \wp_1(\tau, f_c; P_{\vec{v}}) \tag{2.2}$$

where Λ is the auto-correlation function of the baseband signal, and $\wp_1$ is a function of the PDF. The convolution operation is performed in the delay dimension. The region of the surface of the ocean that reflect the incident signal toward the direction of the receiver is referred to as the glistening zone.

3. SCATTERING MODEL THEORY

This chapter explains basic concepts of the geometry, the bistatic measurements and the scattering model. The geometry in the problem is defined in Section 3.1. Section 3.2 introduces the fundamentals of the ocean surface scattering and the statistical representation of the rough surface. Section 3.3 discusses two ocean scattering models, KA-GO (Kirchhoff Approximation-Geometric Optics) and SSA (Small Slope Approximation). Section 3.4 explores the different PDF models of the sea surface slopes.

3.1 Geometry

A reflectometry system is a bistatic radar configuration, which, in contrast to monostatic radar, has a seperate transmitter and receiver. Unlike back scattering in a scatterometer, a bistatic system receives reflected signals in a forward scattering mode. As a result, the bistatic system has a more complex geometry as the incident and the reflected vectors are not parallel in this case.

3.2 Coordinate System

To illustrate the forward scattering scenario, this thesis uses a local coordinate system which is fixed with respect to the reflecting and the scattering plane. Figure 3.1 shows the structure of this coordinate system where. The specular point is the point where reflection angle is equal to the incidence angle. In this coordinate system, the origin is the specular point, and the z-axis is the normal direction of the horizontal sea surface. The transmitter, receiver and specular point together define the yz-plane. The positive y-axis points to the transmitter and the direction of positive x-axis complies with the right-hand rule of y and z axis.

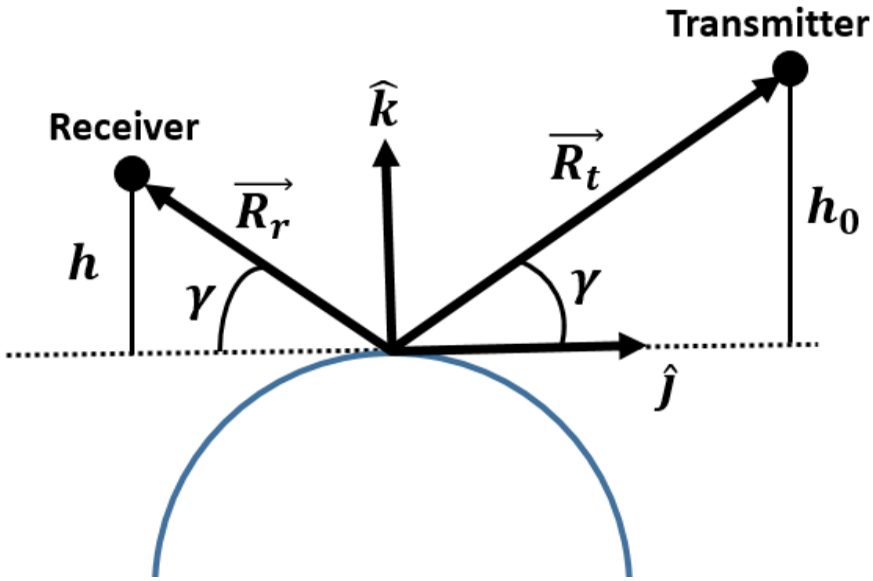

Figure 3.1. Definitions of the coordinate system.

Figure 3.2 shows the definition of relevant vectors in the geometry defined above. The positions of the transmitter, $\vec{R}_t$, receiver, $\vec{R}_r$, and each scattering point, $\vec{R}_s$, are defined as follows:

$$\begin{aligned} \vec{R}_t &= 0\hat{i} + h_0\ cot(\gamma)\hat{j} + h_0\hat{k} \\ \vec{R}_r &= 0\hat{i} - h\ cot(\gamma)\hat{j} + h\hat{k} \\ \vec{R}_s &= x\hat{i} + y\hat{j} + \zeta(\vec{\rho})\hat{k} \end{aligned} \tag{3.1}$$

where, $\vec{\rho} = [x, y, 0]^T$ is a position vector used to represent the location of any scattering point on the sea surface, in other words, the x-y plane, and $\zeta(\rho)$ is represents the ocean surface surface height relative to the mean value at location $\vec{\rho}$.

The unit vectors in the incident direction $\hat{m}$ and the scattering direction,$\hat{n}$, are defined as

$$\begin{aligned} \hat{m} = \Delta\ R_0 = \frac{\vec{R}_0}{R_0} &= \frac{\vec{R}_s - \vec{R}_t}{|\vec{R}_s - \vec{R}_t|} \\ \hat{n} = \Delta\ R = \frac{\vec{R}}{R} &= \frac{\vec{R}_r - \vec{R}_s}{|\vec{R}_r - \vec{R}_s|} \end{aligned} \tag{3.2}$$

where, $R_0 = |\vec{R_s} - \vec{R_t}|$ represents the distance between the transmitter and the scattering point, and $R = |\vec{R_r} - \vec{R_s}|$ defines the distance between the receiver and the scattering point. The scattering vector is expressed as:

$$\vec{q} = \frac{2\pi}{\lambda}(\hat{n} - \hat{m}) = k(\hat{n} - \hat{m}) \tag{3.3}$$

where λ is the wavelength and $k = 2\pi/\lambda$ is the wave number. The scattering vector, $\vec{q}$, can be expressed as

$$\vec{q} = \vec{q_\perp} + q_z\hat{k} \tag{3.4}$$

where $\vec{q_\perp}$ is the component in the x-y plane which can be further represented as

$$\vec{q_\perp} = q_x\hat{i} + q_y\hat{j} \tag{3.5}$$

3.3 Rough Surface Scattering

The scattering features of electromagnetic waves are strongly affected by the surface roughness. Rayleigh proposed the most commonly used criterion to determine if the surface can be modeled as rough [31]:

$$\sigma_z > \frac{\lambda}{8cos\theta} \tag{3.6}$$

where σ_z is the variance of the sea surface height, λ is the wavelength and θ is the incidence angle.

If a surface is perfectly smooth with zero σ_z, only a coherent reflection will appear in the specular direction, with the ratio between the incident and scattered energy being equivalent to the Fresnel reflection coefficient [32]. As the scattering surface gets rougher, a diffuse scattering component appears. Then, for example, if the surface is slightly rough but still meets the Rayleigh criterion, some of the incident power is now radiated back in other direction. In this case, the coherent scattering and diffuse scattering coexist with the coherent scattering still being the dominant component.

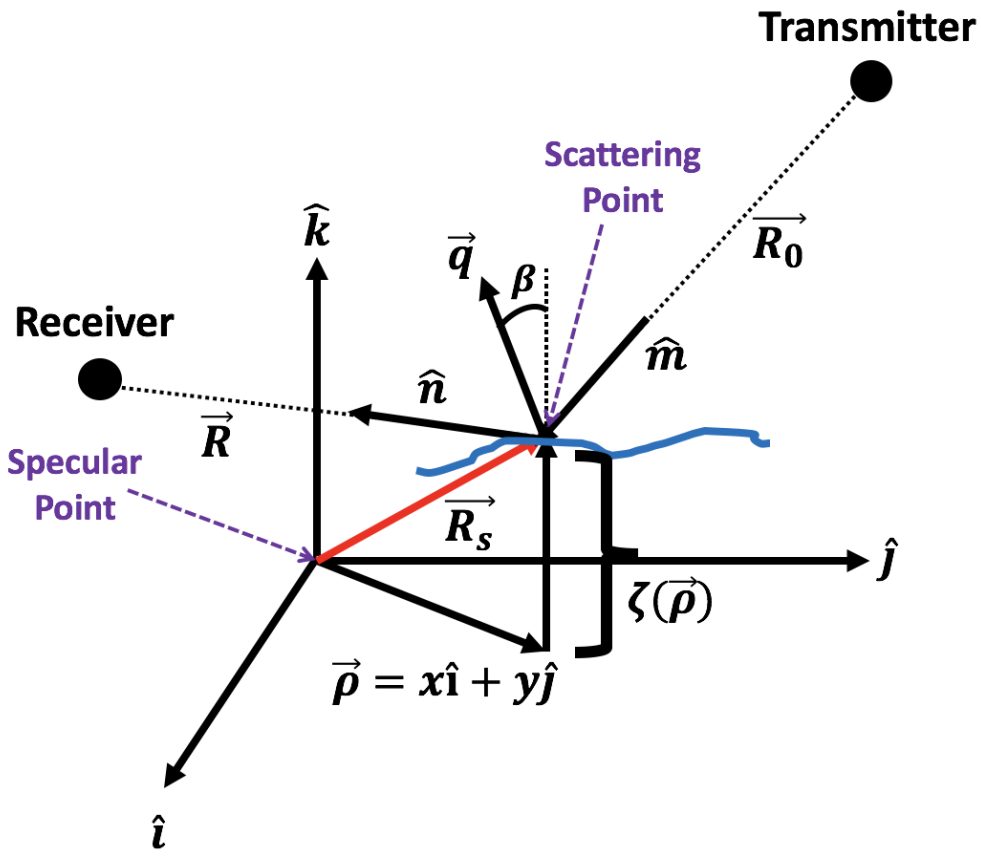

Figure 3.2. Definitions of the vectors.

Furthermore, if the surface is very rough, most of the energy is diffusely scattered and the coherent component becomes negligible. The surface roughness with respect to the wavelength determines the portion of energy being diffusely scattered.

The following subsections give a review of ocean scattering models with insights into the specular and diffuse scattering component of the surface roughness, as well as ocean surface roughness models, including both the PDF model of ocean wave slopes and models addressing the relationship between ocean surface roughness parameter and wind speed.

3.3.1 Ocean Scattering Model

This section will introduce ocean scattering models. The total scattering power measured by a bistatic radar receiver P_r can be expressed as the sum of the power of the coherent component P_c and incoherent component P_i in [33]:

$$P_r = P_c + P_i \tag{3.7}$$

where P_c and P_i are the power of the coherent and incoherent components, respectively.

(1) Coherent Scattering Component:

The power of the coherent scattering component, P_c, can be expressed as [33]:

$$P_c = \frac{P_t \lambda^2 G_t G_r |\overline{V}|^2}{(4\pi)^2 (R_{sp} + R_{0,sp})^2} \tag{3.8}$$

where $\overline{V}$ is the average reflection coefficient of the sea surface, $R_{0,sp}$ and R_{sp} are the distances from the transmitter and receiver to the specular point, respectively. The coherent component also depends on the transmitter and receiver antenna radiation patterns, G_t and G_s, respectively. These variables are assumed to be constant near the specular point.

(2) Non-coherent Scattering Component:

The non-coherent component of the total scattered power, assuming a bistatic radar cross section σ_0, is expressed by the bistatic radar equation:

$$P_i = \frac{P_t \lambda^2}{(4\pi)^3} \int \frac{G_t G_r}{R^2 R_0^2} \sigma^0 dA \tag{3.9}$$

The computation of the scattering power requires a model of bistatic radar scattering, which is obtained by using different approximations describing the scattering of the incident electromagnetic field on a random surface. The narrowband signals used in the study of this thesis, such as GNSS and regular communication signals, can usually be considered as quasimonochromatic, phase-modulated, spherical waves [1]. Thus the scattered field can be solved from the Helmholtz equation if the boundary conditions are known. However, expressing the exact boundary condition is difficult

for scattering from random surfaces, so some approximations have to be made in order to simplify the problem. The common approaches in bistatic scattering from sea surface include the Kirchhoff Approximation (KA) under the Geometric Optics (GO) and the recently developed model based on Small Slope Approximation (SSA). The difference between them lies in specific constraints applied to wavelength, geometry and parameters describing roughness.

KA-GO

The Kirchhoff approximation (KA) under geometric optics (GO), is one of the commonly used approaches to represent the rough surface scattering. The KA-GO model represents the fields at any surface point by fields that would be present on the tangent plane at that point. The model is also based on the assumption that the field at any surface point is the sum of incident and reflected fields.

The calculation of the reflected field is based on the assumption that the local surface can be considered as a tangent plane with respect to the wavelength of the incident microwaves. In other words, the KA-GO is limited to the cases of large correlation scales and large average curvature radii, compared to the wavelength of the signal. These conditions will become invalid if the roughness includes sharp peaks [34]. This assumption can be expressed as:

$$4\pi r_c cos\vartheta >> \lambda \tag{3.10}$$

where r_c is the curvature radius, λ is the wavelength and ϑ is the incidence angle.

Other limitations include the fact that the Kirchhoff Approximation cannot reproduce the Bragg resonant scattering accurately. Also, it is applicable only for incidence angles far away from grazing when the scattered waves can be considered as plane waves. The bistatic scattering model based on KA-GO [1] is designed only for strong diffuse scattering that takes place at a large Rayleigh parameter $R_a = kcos\theta\sigma_h$. The Rayleigh parameter involves the EM wavenumber k, the r.m.s. of surface roughness σ_h, and the incidence/scattering angle θ. In this case, the scattered field is totally

diffuse, because it is formed by the summation of a large number of uncorrelated field contributions originated from a large surface area.

SSA

The classical methods to analyze the scattering process, such as small perturbations (MSP) [35] and the Kirchhoff approximation (KA), are constrained by the assumption on the scale of the roughness compared to the EM wavelength, and thus cannot cover the entire range of practical problems. Their combination, i.e. the two-scale model [35], extends the potential of these calculations but relies on a more or less arbitrary parameter arises that divides roughness into two classes, large scale and small scale.

The Small Slope Approximation (SSA) method is a more accurate approximation and is free of this disadvantage [35]. It bridges the gap between these two classical approaches. In contrast to these methods, the SSA is applicable regardless of the radiation wavelength, given that the slopes of roughness are relatively small compared with the incidence and scattering angles. For Neumann and Dirichlet problems, the second-order expression for scattering amplitude under the high frequency limit is identical to the KA's formula. For low frequency cases, the MSP results are reproduced automatically.

The derivation of the SSA model is based on the transformation properties of scattering amplitude w.r.t. spatial shifts of rough boundaries [36]. Scattering amplitude is expressed as a product of two factors; the first one is a "Kirchhoff-type" factor which represents required transformation properties, and the second one is an integral-power series. The slope of roughness becomes the small parameter in this expansion, which is independent of wavelength. The statistical moments of the scattering amplitudes are directly related to the mean-reflection coefficient and scattering cross sections, which are usually determined experimentally.

There are two approximations of the SSA: the SSA of the first order (SSA1) and the more accurate one, the SSA of the second order (SSA2). This thesis focuses on the implementation and evaluation of SSA1, which suffices for calculations of the forward-scattering L-band LHCP BRCS and S-band RHCP BRCS used in this research. The SSA1 gives the BRCS expression in the form of a 2D surface integral that is similar to that obtained in the KA model, but with a more accurate pre-integration factor [35]. The most important difference between the SSA1 and KA is that, for SSA1, the correlation function of the surface wave height is not assumed to be slowly varying and may contain small scale components that are responsible for Bragg scattering.

In addition, as mentioned above, the KA-GO model is designed for strong diffuse scattering that happens at a large Rayleigh parameter R_a, i.e., when the coherent component can be neglected. However, in reality, the coherent component would appear or even dominant in the scattering process when R_a is small. As the value of R_a grows, the diffuse scattered field becomes stronger, whereas the coherent specular component rapidly decays. The SSA model considers both the coherent and non-coherent components of the scattered waves, which allows the transitions of non-coherent to partially coherent scattering to be correctly described.

3.4 Surface Roughness Model

The strength of the signal bistatically scattered from the ocean surface is mostly affected by the surface roughness. Ocean surface roughness is mainly driven by wind, although there can be other non-local factors, such as swell. For linear surface gravity waves, the slope PDF, $P(s)$, can be usually approximated by a bivariate Gaussian distribution. The distribution either depends upon an ocean wave spectrum model and assumed cutoff wavenumber [11] or some empirical model. These models are often parameterized in terms of wind vectors (typically measured at a height of 10 m, U_{10}) . Some models also include other parameters such as wave age.

3.4.1 PDF of Sea Surface Slopes

The simplest PDF is a Normal distribution, described by the MSS of the surface waves, if an isotropic surface is assumed, or by upwind and crosswind slopes, if a bi-direction surface is assumed. The Gram-Charlier PDF is a more complex model that includes skewness parameters in the Gaussian distributions as introduced in [10]. In our case, we just assume that the skewness effects can be neglected. Thus, the Gaussian PDF used in this thesis is obtained as:

$$P_{\vec{v}}(-\frac{\vec{q_\perp}}{q_z}) = \frac{e^{-\frac{1}{2}(\xi^2+\eta^2)}}{2\pi\sigma_c\sigma_u} \tag{3.11}$$

where ξ and η are related to the root mean square slope, upwind, σ_u, and the crosswind, σ_c, and the scattering vector, $\vec{q}$, by:

$$\xi = \frac{q_x/q_z}{\sigma_u}, \quad \eta = \frac{q_y/q_z}{\sigma_c} \tag{3.12}$$

For an isotropic Gaussian distribution, the variances in upwind and crosswind directions are the same $\sigma_u = \sigma_c$

$\sigma_{u,c}$ depends on wind, and by theory can be derived from a surface elevation spectrum, $\Psi(k)$, which is largely influenced by the wind speed. This computation is done by integrating the spectrum over wave numbers, k, smaller than a dividing parameter, κ. Another approach is obtaining an empirical model for MSS versus wind speed from multiple GNSS-R measurements of GNSS waveforms performed under a wide range of wind conditions. The following sections introduce the different models which addresses the MSS-wind relationship.

3.4.2 Cox and Munk's Model

Cox and Munk developed an empirical model relating the MSS of the sea surface to wind speed using the data extracted from sun optical measurements [10]. In this

model, the root mean square slopes, i.e., upwind, σ_u, and crosswind, σ_c, have a linear relationship with the wind speed, U_{10}:

$$\sigma_c^2 = 0.003 + 1.92 \times 10^{-3} U_{10}$$
$$\sigma_u^2 = 3.16 \times 10^{-3} U_{10} \tag{3.13}$$

It is noted that the larger MSS or upwind and crosswind slopes correspond to a higher wind speed that generates a rougher surface.

In order to approximate the effect at microwave wavelengths, which in our work includes GNSS and XM signals, Wilheit proposed a correction to this model which reduces the variances [37]:

$$\sigma^2(f) = (0.3 + 0.02f)\sigma_m^2 \quad f < 35GHz$$
$$\sigma^2(f) = \sigma_m^2 \qquad\qquad\qquad\quad f > 35GHz \tag{3.14}$$

where f is the microwave frequency in GHz and σ_m^2 is the total MSS $\sigma_m^2 = \sigma_u^2 + \sigma_c^2$. For the case of L1 GPS signal with the center frequency of 1.57542 GHz, this model gives a reduction of 0.33. For XM signal, one of the frequencies is 2.342 GHz, giving a reduction of 0.35. Upon later comparisons with a larger data set, a preliminary value of 0.45 was found to give better agreement between data and surface truth (buoys) at low wind speeds ($<$ 10 m/s).

3.4.3 Katzberg's Model

This section describes the L-band empirical model developed by Katzberg et al. based on the data collected during NOAA hurricane experiments [12]. Katzberg et al. presented the results of GPS reflection calibration for winds up to 46 m/s, along with a model function relating MSS to surface wind speed. This model defined the upwind and crosswind MSS, respectively, as:

$$\sigma_u(U_{10}) = 0.45 \cdot (0.00 + 0.00316 \cdot f(U_{10}))$$
$$\sigma_c(U_{10}) = 0.45 \cdot (0.003 + 0.00192 \cdot f(U_{10})) \tag{3.15}$$

where

$$\begin{aligned} f(U_{10}) &= U_{10} && 0 < U_{10} \leq 3.49 \\ f(U_{10}) &= 6 \cdot ln(U_{10}) && 3.49 < U_{10} \leq 46 \\ f(U_{10}) &= 0.411 \cdot U_{10} && 46 < U_{10} \end{aligned} \tag{3.16}$$

3.4.4 Elfouhaily's Model

The Elfouhaily model, proposed in [11], describes wind-driven waves under diverse wave age ("fetch") conditions. According to the Elfouhaily model, the elevation spectrum of a well-developed sea surface can be expressed as a product of the azimuthal part and the radial part of the spectrum. The azimuthal part is a two-sided function; it does not distinguish between up- and down-wind directions. The radial part reproduces two main features of the spectrum: its anisotropy and the wavenumber dependence of the angular spectral width. There are other situations when wind direction does not coincide with the peak of the spectrum, for example, when waves generated by a local wind are superimposed with a swell, or when gravity waves undergo refraction. Such complicated cases are not covered by the Elfouhaily model.

Ocean Wave Spectral Definitions and MSS Derivations

In this section, we give a summary of relevant spectral definitions and MSS derivations. The elevation spectrum is the Fourier transform of the autocovariance function of the surface displacements:

$$\Psi(\vec{k}) = FT\langle\eta(\vec{r_0})\eta(\vec{r_0} + \vec{r})\rangle \tag{3.17}$$

where FT is the Fourier transform operator, the angle bracket is the ensemble average operation, η is the zero-mean surface elevation, and $\vec{r}$ is the horizontal lag over the surface. The omnidirectional spectrum, $S(k)$, is:

$$S(k) = \int_{-\pi}^{\pi} \psi(k, \phi) k d\psi \tag{3.18}$$

If this is integrated over the entire wavenumber range, it produces

$$\sigma_\eta^2 = \langle \eta^2 \rangle = \int_0^\infty S(k)dk \tag{3.19}$$

σ_η is the standard deviation of surface elevations, $\psi(k,\phi)$ is the directional spectrum. The wind is assumed to be blowing in the positive x axis. The MSS in the upwind direction is:

$$\sigma_u^2 = \int_\infty^\infty \int_\infty^\infty k_x^2 \Psi(k_x,k_y)dk_x dk_y = \int_o^\infty \int_\pi^\pi k^2 cos^2\phi \Psi(k,\phi)kdkd\phi \tag{3.20}$$

while in the crosswind direction it is:

$$\sigma_c^2 = \int_\infty^\infty \int_\infty^\infty k_x^2 \Psi(k_x,k_y)dk_x dk_y = \int_o^\infty \int_\pi^\pi k^2 sin^2\phi \Psi(k,\phi)kdkd\phi \tag{3.21}$$

The total MSS in the omnidirectional context is:

$$\begin{aligned}\sigma_m^2 = \sigma_u^2 + \sigma_c^2 &= \int_\infty^\infty \int_\infty^\infty (k_x^2 + k_y^2)\Psi(k_x,k_y)dk_x dk_y \\ &= \int_o^\infty \int_\pi^\pi k^2 \Psi(k,\phi)kdkd\phi = \int_0^\infty k^2 S(k)dk\end{aligned} \tag{3.22}$$

The factor in the integral ($k^2 S(k)$) is called the omnidirectional slope spectrum. To obtain the slope variances, the spectrum needs to be integrated over wave numbers. As pointed out above, the MSSs that determine the BRCS through the PDF of slopes are not full wave slopes. Even though the sea surface contains wave components both larger and shorter than the incident electromagnetic waves, the short waves can be disregarded in a process of forward quasi-specular reflection under the GO model. Therefore, the full surface spectrum should be cut off near the high end of the wavenumber range. The cutoff number is essentially the bandwidth of a low pass filter, passing only the surface roughness with a longer wavelength than some fraction of the signal wavelength. The parameter k_* is somewhat arbitrary. The commonly used expression for the cutoff number is given as [4]:

$$k^* = \frac{2\pi sin(\gamma)}{3\lambda} \tag{3.23}$$

where γ is the satellite elevation angle and λ is the signal wavelength. Therefore, the variances are:

$$\sigma_{u,c}^2 = \int_{k \le k_*} k_{u,c}^2 S(k) \tag{3.24}$$

4. GEOPHYSICAL MODEL FUNCTION DEVELOPMENT FOR REMOTE SENSING OF HIGH OCEAN SURFACE WINDS USING S-BAND REFLECTOMETRY

This chapter describes the development of an S-band geophysical model function (GMF). First, the NOAA hurricane flight campaign for S-band data collection will be described in Section 4.1. Then, the criterion for selecting proper calibration and validation data sets will be illustrated in Section 4.2. The three kinds of in situ truths (SFMR, HWRF and GPS dropsonde) used in GMF development will be introduced in Section 4.3. Section 4.4 will detail the model development process including the approaches, algorithms and final results, and Section 4.5 will show the evaluation of the new S-band GMF by comparing the retrievals with different kinds of in situ truths. The conclusions will be presented in Section 4.6.

4.1 2014 NOAA Hurricane Experiment Description

Data used for this work were collected on flights of a NOAA P-3 Hurricane Hunter aircraft during the 2014 Hurricane season between 2-Jul-2014 and 17-Sep-2014, a period covering 4 named storms (Arthur, Bertha, Cristobal and Edouard). A wideband recording system, based upon the commercially available Universal Software Radio Peripheral (USRP), operated at a sample rate of 4 MHz, a center frequency of 2.343125 GHz and 8-bit complex quantization, was flown during this experiment. Its bandwidth is sufficient to capture one transmitted channel from each satellite in the XM-Radio system, XM3 (Rhythm) located at 85^{o}W and XM4 (Blues) located at 115^{o}W. A left-hand circularly polarized antenna (Antcom 3M23L-A-XT2) was installed on the top of the fuselage to receive the direct signal and a RHCP antenna

(Antcom 3M23R-A-XT2) was installed on the bottom to capture the reflected signal. Data were recorded to a hard disk for 1 min. every 6 min. (i.e. with 5 min. gaps between recordings). All data were downloaded at the end of the campaign and post-processed following the procedure in [9] to generate the cross-correlation between the direct and reflected signals, commonly referred to as the "waveform" or delay-Doppler map (DDM).

Wind speed was estimated by fitting a forward model, based upon the standard scattering model [1], to the crosscorrelation waveform shapes. A least-squares approach [4] [38] was used with the formulation of the forward model as a convolution [30]. A purely bi-variate Gaussian function was incorporated as the slope probability density distribution of the ocean waves, where the MSSs for upwind and crosswind directions were constrained by the Cox and Munk model. Interpolated HWRF wind directions were imported as a priori known truth and used for training data. MSS values were also transformed from the wind direction to the scattering plane.

Although derived from reflections of GNSS L-band signals (1575.42 MHz), the empirical model from [12] was first applied to provide a corresponding wind speed for each MSS estimate. This allowed a preliminary comparison with wind speeds obtained from in-situ measurements on board the aircraft. Some of the results are shown in Figure 4.1. At different times, the reflectometry-derived winds appear to lead or lag the Fight-Level Wind (FLW). There also appears to be a bias between the retrieved winds and FLW for some of the data. A possible source for these discrepancies is the lack of a calibration of the existing L-band empirical model for these measurements to account for the frequency difference. However, this data set covers a wide range of wind speed conditions. Wind speed measurements from other sources such as FLW, SFMR, HWRF and GPS dropsonde are also available to serve as in-situ references. This offers an ideal opportunity to develop an empirical S-band geophysical model function.

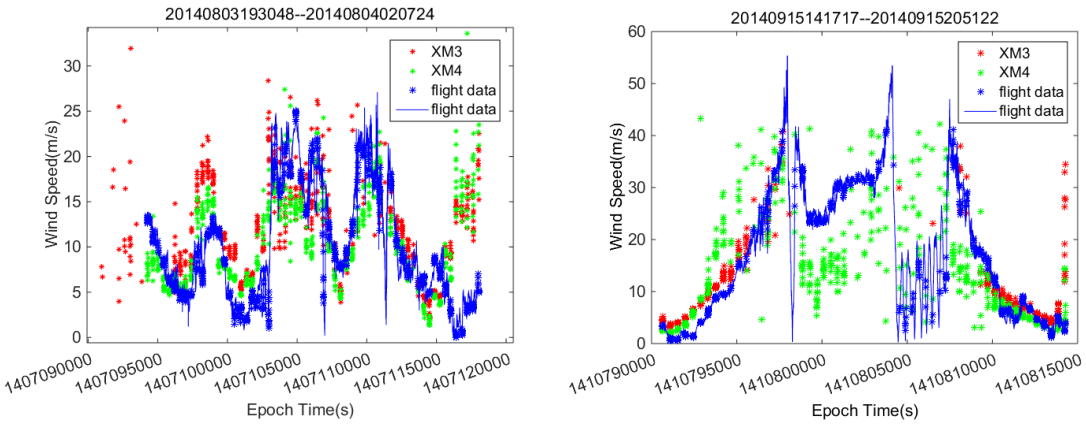

Figure 4.1. Wind speed retrievals 08/03/2014 and 09/15/2014 flights.

4.2 Selection of Calibration and Validation Data

Wind speed retrieval using reflectometry relies on measuring the ocean roughness induced by surface winds. However, surface roughness can also be potentially affected by other environmental factors, such as the presence of land. Moreover, the shape of signal correlation waveforms can be distorted by unsteady aircraft motion. For model development, we categorized three conditions which can cause expected anomalies in wind speed retrievals. Data acquired under these conditions were removed from the data set. As an example, Figure 4.2 marks the areas of the three anomalous conditions along the flight path using circles of three different colors.

1. Close to/over the land. The land will exert a significant effect on the ocean waves in areas closer to the shore, leading to deviations in the retrieved wind. Obviously, the reflectometry technique would not apply to wind speed retrieval over land. To eliminate land effects, data collected at least 15km away from the coast were selected for model development.

2. In the storm eye. The surface roughness does not decrease greatly due to the rapid drop of wind speed in the storm eye, since the local sea is impacted by waves propagating from the nearby eye wall. However, flight-level wind speed measurement is still able to track wind variations in this region. For this work, the locations of

hurricane centers are provided by estimations of HWRF model estimates and a radius of 25km around hurricane centers is used to determine the area of hurricane eyes.

3. During aircraft banking. The large pitch and roll angles in this process can also modify the projection of the downward-looking antenna pattern over the ocean surface, introducing distortions in the correlation waveforms due to antenna pattern variations.

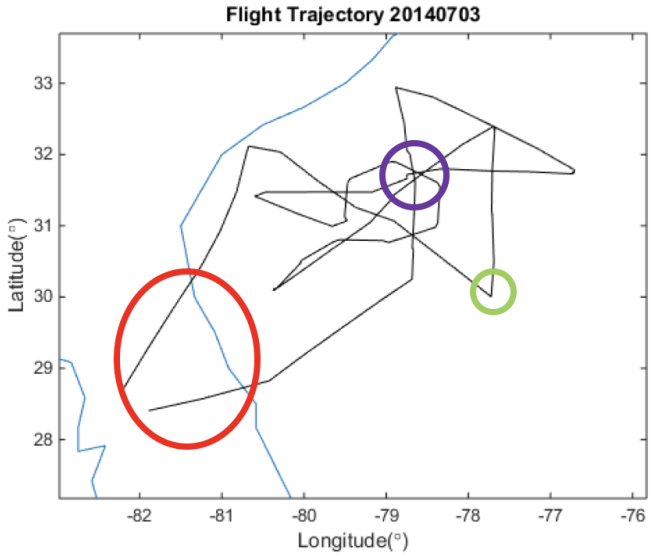

Figure 4.2. Flight trajectory of 07/03/2014 in Hurricane Arthur. The red, purple and green circles represent the areas close to/over the land, in the storm eye and during aircraft banking respectively.

In addition, in this analysis, XM4 data were ignored because the XM4 satellite has a much lower elevation angle than that of XM3. That leads to a larger sensitivity to wind direction and imperfect antenna patterns. The sensitivity to wind direction has been detailed in many of previous studies [12]. Recent work has found that the rapid variations of antenna pattern in low elevation region can also affect the wind speed retrievals [39]. As a result, the simplified isotropic antenna pattern often used in reflectometry models can induce large bias in the retrieved wind speed for data from low elevation satellites. Future work will continue to try to resolve this issue

by incorporating a more accurate antenna pattern and will also be focused on more thorough analysis of the combined effects of the elevation angle and antenna pattern.

4.3 Selection of the In Situ Truth

Three data sources of ocean surface wind speed for the 2014 hurricanes are selected as the in situ truth for either model development or evaluation, which includes SFMR, HWRF model and GPS dropsonde data.

The SFMR measures C-band brightness temperatures (T_b) of the ocean surface and an inversion algorithm is used to retrieve wind speed. After the initial GMF (geophysical model function) development work performed in 2007 [40], a significant overestimation of surface wind speeds is found in lower wind speeds, particularly in heavy precipitation. An updated set of GMF coefficients was then determined to tackle this issue. The revised SFMR wind speed retrievals showed that the new GMFs largely reduced the bias at weaker wind speeds [41]. Recently the NOAA group has reprocessed all the SFMR data using the updated algorithm and the new wind speed product. This new product was used in situ data for the model development [42].

The Hurricane Weather Research and Forecasting (HWRF) model is a specialized version of the Weather Research and Forecasting (WRF) model and is used to forecast the track and intensity of tropical cyclones. The HWRF has the advantage of accurately reproducing the wind field detail quite near the core of a tropical storm. The atmospheric model is run with three telescopic atmospheric domains. The parent domain covers an $80^o \times 80^o$ latitude$-$longitude area with a grid spacing of 27 km, the intermediate nest domain covers $11^o \times 11^o$ with a 9-km grid spacing, and the innermost nest covers $6.5^o \times 7.2^o$ area of the storm core with 3-km grid spacing. The nests move to follow the storm. The model runs every 6 hours and forecasts up to 126 hours in advance with 3-hour interval in each run [43].

The GPS dropsonde is a device employed by the NOAA hurricane campaign to measure the wind speed profile of hurricanes. During the time of descent, it continues

measuring wind speeds at different altitudes. [44] shows the wind speed profile of different hurricanes from GPS dropsondes. The WL150 algorithm has been widely accepted as the best one to estimate the sea surface wind speed from dropsonde data. In this algorithm, the surface wind speed is derived by adjusting the average wind speed from the lowest 150-m portion of the dropsonde profile using a dropsonde-based mean eye wall profile [44] given by:

$$R(z) = 1.0314 - 0.00407z + 2.465 \cdot 10^{-5}z^2 - 5.446 \cdot 10^{-8}z^2 \tag{4.1}$$

where $R(z)$ is the ratio of the dropsonde 10-m wind speed to the WL150 wind speed, and z is the mean altitude of the 150-m layer.

For the NOAA hurricane experiments, SFMR wind speed is reported every second during the flight period covering the whole flight path, so it provides abundant reference data for S-band reflectometry. HWRF has a good 3-km spatial resolution for forecasting the wind speed in the innermost core. However, the 3-hour updating period becomes a limitation for temporal resolution considering the relatively rapid variation of conditions in hurricanes, especially in the storm core. GPS dropsonde wind speed has the best accuracy in measuring the 10m-level wind, but it also has obvious disadvantages such as the limited number of employed dropsondes as well as the deviation from the locations of S-band measurements during descent. Thus, the fairly promising reliability and adequate data rate make SFMR wind speed the ideal reference of the S-band GMF development. In addition, for model verification purpose, half of the pairs of S-band retrieval and SFMR wind speed were applied to model development and the rest were used as independent testing data sets for model evaluation. HWRF forecast and GPS dropsonde wind speed obtained through the WL150 algorithm, as two other independent data sources, are also incorporated to validate the model function.

4.4 Model Development

Wind speed was estimated by fitting a well-established forward model [1], to the crosscorrelation waveform shapes, using a least-squares approach [4] [38], minimizing the cost function

$$J(M) = |\mathbf{Y} - \mathbf{Y}_{m2}(\sigma_u^2, \sigma_c^2, \theta, \mathbf{C})|^2 \tag{4.2}$$

between a vector of waveform samples $\mathbf{Y}$ generated at zero delay in a batch of 50 waveforms. Each waveform was generated with 1-ms coherent integration and 100-sec incoherent average. A bi-variate Gaussian slope probability density is assumed, in which the upwind and crosswind slope variances (σ_u^2 and σ_c^2) were constrained by the Cox and Munk model.

The adjusted Cox and Munk model is

$$\begin{aligned} \sigma_u^2 &= 0.45 \cdot (0.00 + 0.00316 \cdot U_{10C\&M}) \\ \sigma_c^2 &= 0.45 \cdot (0.003 + 0.00192 \cdot U_{10C\&M}) \end{aligned} \tag{4.3}$$

where σ_u^2 and σ_c^2 are represented as a function of wind speed $U_{10C\&M}$. Thus, a relationship between σ_u^2 and σ_c^2 can be derived from the adjusted Cox and Munk model, which is shown as follows.

$$\sigma_u^2 = 0.06076 \cdot \sigma_c^2 + 0.00135 \tag{4.4}$$

The constraint above was incorporated in the process of MSS estimation. Wind direction, θ, was not estimated, but was obtained from HWRF and then interpolated to the time of the measurement and location of the specular point, due to the low sensitivity of waveform shape to wind direction. A vector of additional model parameters, $\mathbf{C}$, includes the aircraft altitude and the transmitting satellite positions. After estimating the MSS for all selected data within the training set, the empirical model developed for GNSS L-band signals (1575.42 MHz) [12] was applied to produce a corresponding wind speed estimate.

The idea of the new S-band geophysical model is to develop a calibrated correction model to the adjusted Cox and Munk model. So, retrieved wind speed from S-band

reflectometry obtained using the adjusted Cox and Munk model, $U_{10C\&M}$, are plotted against in situ truth, U_{10}, as shown in Figure 4.3. It can be observed that $U_{10C\&M}$ increases dramatically as U_{10} goes up in the low wind region, approximating a linear relationship, and then the sensitivity gradually decreases at higher wind speeds. As a result, for the model fitting, the data was split up into two parts with 8 m/s in situ truth wind speed as the boundary. A linear model is used to fit data in the low wind speed region and a logarithm function is applied in the high wind speed region. The two functions intersect at 3.11 m/s.

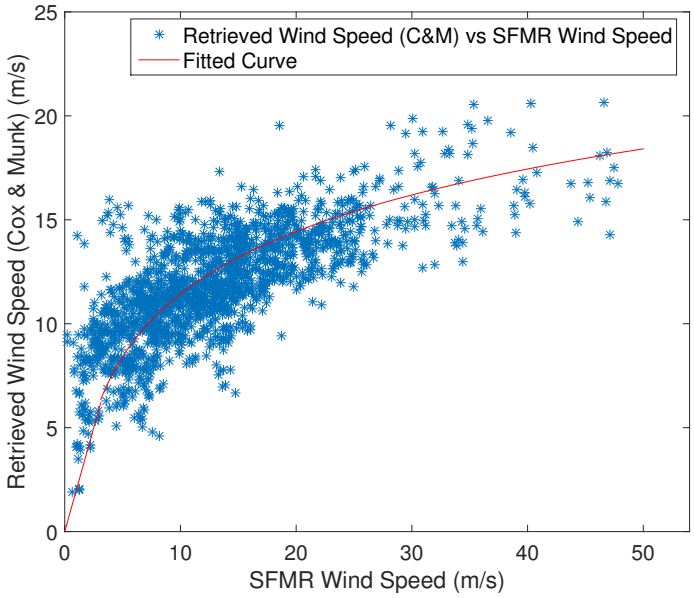

Figure 4.3. Retrieved wind speed (Cox and Munk) vs in-situ truth and the fitted model.

Note that in this fitting process, we also excluded some samples that are far away from the fitted curve to prevent accuracy degradation of model fitting caused by a few abnormal data samples. σ_u^2 estimates higher than 0.035 were removed from the data set. The linear function and the logarithm function intersect at a wind speed

of 3.11m/s. The final S-band model is then obtained as (4.5) and shown as the red curve in Figure 4.3.

$$\begin{aligned} U_{10C\&M} &= 1.994 \cdot U_{10} && 0 < U_{10} < 3.11 m/s \\ U_{10C\&M} &= 4.342 \cdot ln(U_{10}) + 1.426 && 3.11 < U_{10} < 48.33 m/s \end{aligned} \tag{4.5}$$

4.5 Model Evaluation

4.5.1 SFMR

As noted above, half of the pairs were used as test sets for model verification. For this data set, wind speed retrieved from MSS using the S-band model are compared with SFMR wind speed, as shown as the left plot in Figure 4.4. A linear-least-squares fit line with slope of 1.113 and y-intercept 0.6025 m/s is also plotted and the standard deviation around the unity line is 9.73 m/s. It can be observed that the bias between S-band retrievals and SFMR tends to be larger in high wind speed conditions. The result of removing retrievals higher than 50 m/s is shown as the fight plot in Figure 4.4. A least squares fit performed on this data yielded a slope of 0.8202 and a y-intercept of 3.446 m/s. A smaller standard deviation of about 6.59 m/s was obtained in this case.

This shows high consistency between the retrievals processed with the S-band model and the SFMR in situ truth. The larger deviation of the retrievals in the high wind speed region is apparent considering the fact that the increasing rate (slope of the tangent line) of the $ln(U_{10})$ function drops with higher U_{10}. As a result, the uncertainty of wind speed retrieval becomes more sensitive to noise in MSS estimates in higher wind speed regions.

4.5.2 HWRF

The NOAA P-3 flights from which data sets were collected generally take approximately eight hours, spanning multiple forecast steps for the HWRF model. Once the

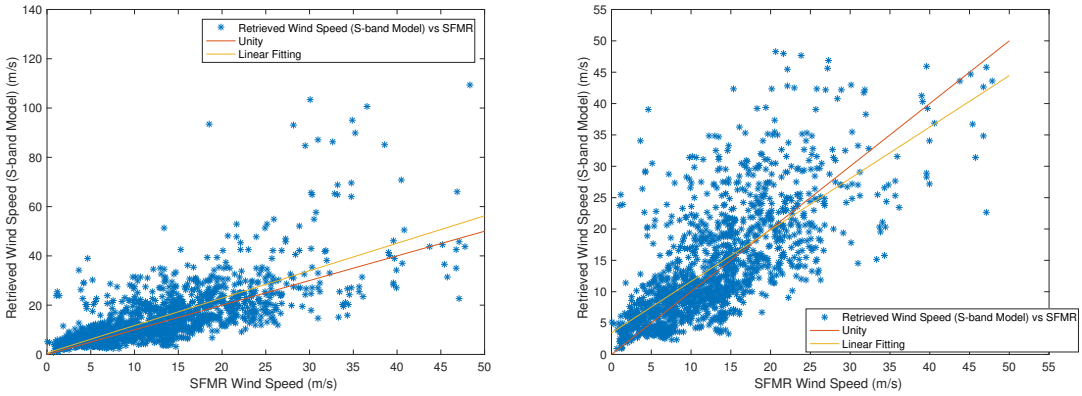

Figure 4.4. Retrieved wind speed vs SFMR wind speed (test set); Left (all data samples): fitted curve is $y = 1.113 \cdot x + 0.6025$, standard deviation around the unity line is 9.73m/s, standard deviation around the fit is 9.45m/s; Right (retrieved wind speed higher than 50m/s were removed): fitted curve is $y = 0.8202 \cdot x + 3.446$, standard deviation around the unity line is 6.59m/s, standard deviation around the fit is 6.33m/s.

model run (6-hour interval) and prediction product (3-hour interval) closest in time to each data sample was selected, the location of S-band wind speed retrieval was used to match the point in the HWRF grid in longitude and latitude to give the reference wind speed at 10-meter height (U_{10}). The P-3 flights were typically arranged to examine the storm core, and the flight pattern usually consists of multiple times of penetrations into the storm center from different directions. The benefit is that the majority of the S-band data were collected in the innermost nest of HWRF, where the model provides the best spatial resolution of 3 km.

The linear-least-squares fit is performed and the standard deviation is calculated for two cases: (1) all samples included and (2) anomalously high wind retrievals removed. The fitting results and statistics are shown in Figure 4.5. As can be seen, the linear fits are very close to the unity line, and the standard deviations are generally less than 7 m/s. The large deviation of the retrievals from the unity line in high wind speed can also be observed. Standard deviation reduces to around 5 m/s

after removing the wind retrievals higher than 60 m/s. This result validates the new S-band model using HWRF wind speed as a reference.

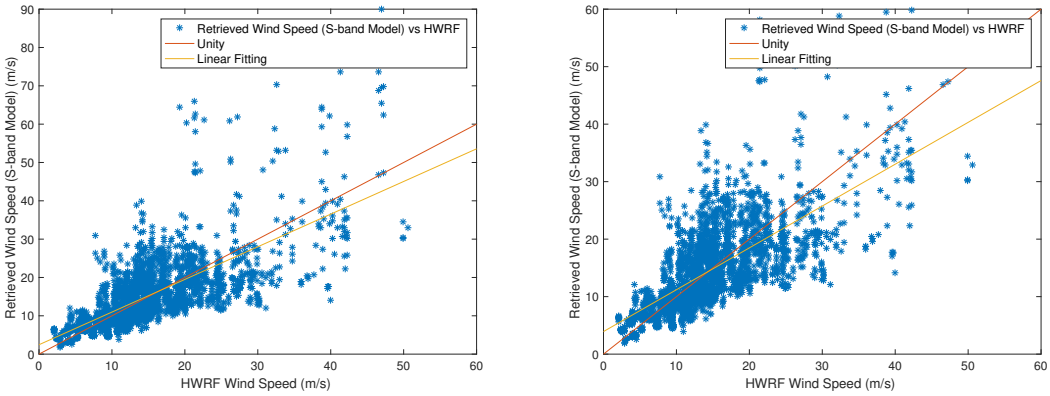

Figure 4.5. Retrieved wind speed vs HWRF wind speed; Left (all data samples): fitted curve is $y = 0.8518 \cdot x + 2.454$, standard deviation around the unity line is 6.69 m/s, standard deviation around the fit is 6.67 m/s; Right (retrieved wind speed higher than 60 m/s were removed): fitted curve is $y = 0.7277 \cdot x + 3.925$, standard deviation around the unity line is 5.71 m/s, standard deviation around the fit is 5.36 m/s.

4.5.3 GPS Dropsonde

GPS dropsonde data are incorporated as another set of ground truth to further investigate and test the S-band geophysical model. GPS dropsonde data are available for 7 days of the hurricane period. As shown in Figure 4.6, the dropsonde data present a close match with measurements from other sources including S-band reflectometry measurements. Compared with other data sources, there is a small deviation in dropsonde wind along the time axis, which is caused by the location deviation of dropsonde measurements. The dropsonde data were aligned with other data sets through the time tag of its measurements. However, due to the time it takes for dropsondes to fall onto the sea surface from the aircraft as well as its horizontal movement

in the process, locations of dropsonde measurements normally do not coincide with the simultaneous measurements from other sources.

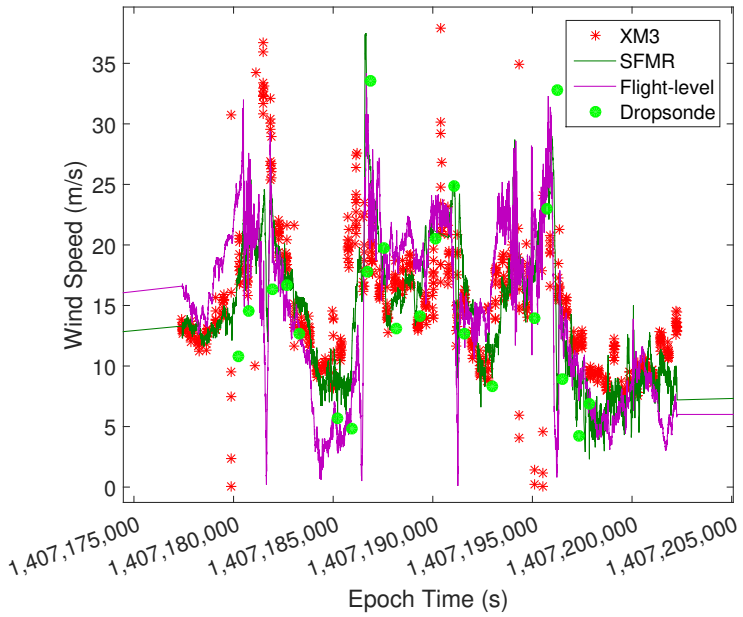

Figure 4.6. Comparison between S-band wind speed retrievals and wind speed measurements from other sources (SFMR, flight-level and GPS dropsonde), date: 08/04/2014.

Another problem is that the signal collection system used in the experiment was not configured for the continuous data collection mode. In every period, it recorded data for 1 minute and slept for 5 minutes. This setting was a trade-off between limited data storage space and wide area coverage. The drawbacks were, however, that for many of the dropsonde data, there was a large deviation in locations with the reflectometry measurements. The solution was setting a spatial constraint to select the appropriate S-band data for comparison. Figure 4.7 plots the locations for the S-band and dropsonde measurements from one days worth of data. The plot at the right side is the zoomed one focused on one specific dropsonde measurement, where a clear location deviation can be seen between the dropsonde and nearby S-band measurements. The red circle centered at the specific dropsonde represents the imposed

spatial constraint. The S-band data inside the circle were picked up to compare with corresponding dropsonde measurement for the model function evaluation.

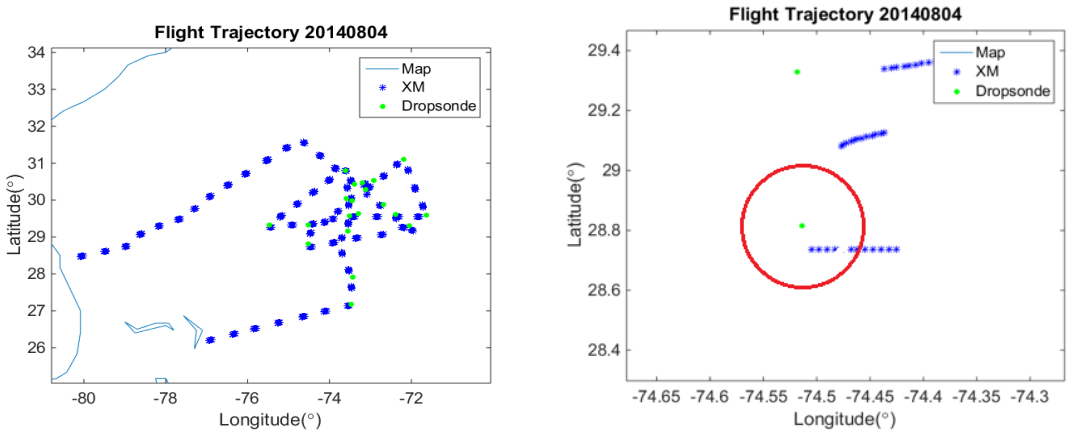

Figure 4.7. Locations of the S-band and dropsonde measurements along the flight path on 08/04/2014. The figure on the right side is the zoomed plot focused on one specific dropsonde and the red circle represents the spatial constraint.

For quantitative validation, a comparison was made between the retrieved S-band wind speed using the new model function and the dropsonde data. Figure 4.8 represents the result of removing dropsonde and Bistatic S-band retrieval pairs over land, inside the tropical cyclone eye and outside the 20000-m distance constraint (with respect to the corresponding dropsonde location). The x axis represents dropsonde data and y axis the retrievals. A linear-least-squares fit line with slope of 0.9501 and y-intercept 2.37 m/s is shown in the left plot in Figure 4.8 with the standard deviation being 7.89 m/s. As noticed, there are a few anomalously high wind speed retrievals located above 35 m/s, mostly associated with two specific dropsondes. The fit becomes $y = 0.7545 \cdot x + 4.028$ and the standard deviation is reduced to 4.95 m/s after these data were removed.

The result of applying the 10000-m distance limit is shown in Figure 4.9. Two plots are also shown for the case. After removing the anomalous wind speed retrievals

higher than 35 m/s (right plot), a least squares fit performed to this data yielded a slope of 0.8009, a y-intercept of 3.419 m/s and a standard deviation of 4.84 m/s is obtained. This shows that the agreement between the S-band retrieval and dropsonde data is generally good and confirms the S-band model developed previously. In addition, minimizing effects of advection by applying a smaller distance threshold could yield improved comparisons.

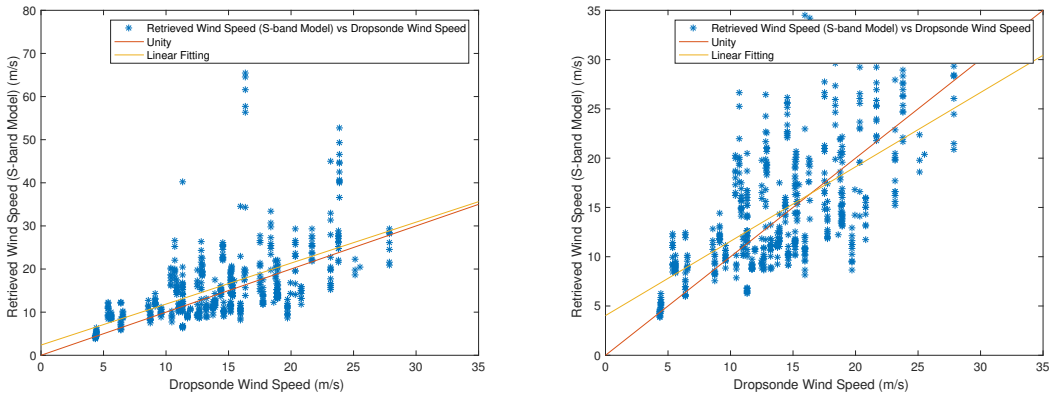

Figure 4.8. Retrieved wind speed vs dropsonde wind speed (distance < 20000 m); left (all data samples): fitted curve is $y = 0.9501 \cdot x + 2.37$, standard deviation around the unity line is 7.89 m/s, standard deviation around the fit is 7.71 m/s; right (retrieved wind speed higher than 35 m/s were removed): fitted curve is $y = 0.7545 \cdot x + 4.028$, standard deviation around the unity line is 4.95 m/s, standard deviation around the fit is 4.82 m/s.

4.6 Conclusions

Recently, reflectometry methods have been extended to utilize communication satellite transmissions in other bands. The 2014 Hurricane mission provided a large volume of useful S-band reflectometry data covering a wide range of wind speed, allowing for the development of an empirical S-band geophysical model function. Data collected in anomalous conditions were removed. Using SFMR wind speed as in situ truth, a new geophysical model for S-band reflectometry has been developed, which

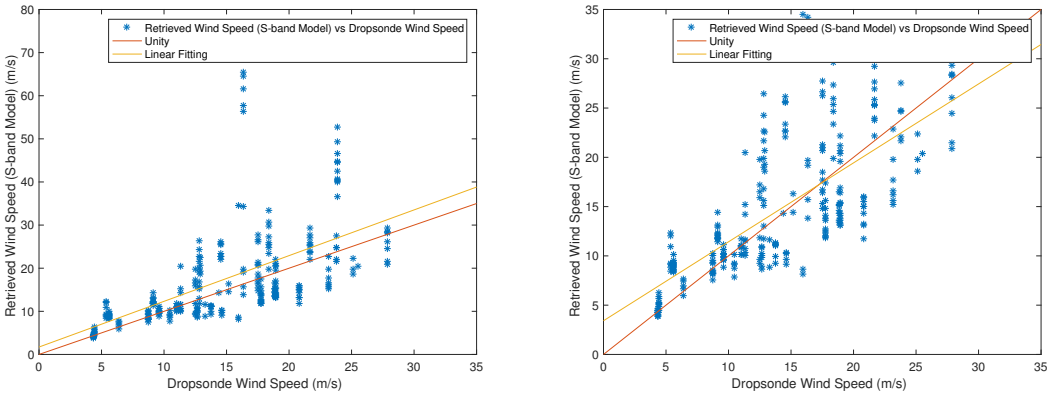

Figure 4.9. Retrieved wind speed vs dropsonde wind speed (distance $<$ 10000 m); Left (all data samples): fitted curve is $y = 1.06 \cdot x + 1.718$, standard deviation around the unity line is 9.85 m/s, standard deviation around the fit is 9.50 m/s; Right (retrieved wind speed higher than 35 m/s were removed): fitted curve is $y = 0.8009 \cdot x + 3.419$, standard deviation around the unity line is 4.84 m/s, standard deviation around the fit is 4.64 m/s.

relates MSS to winds from $<$ 2 m/s to 48.33 m/s. The S-band geophysical model function was evaluated using wind speed from the SFMR test set, HWRF model as well as that from 140 GPS dropsondes. Tolerances were set for selecting the appropriate S-band reflectometry measurements for comparison with the corresponding GPS dropsonde. Improved comparisons can be obtained with a smaller distance constraint. The good agreement between S-band retrievals and both SFMR, HWRF and dropsonde wind speeds validated the S-band geophysical model function. Future work will be focused on the variations of the MSS-wind speed relationships in different regions inside a hurricane.

5. OCEAN ROUGHNESS AND WIND MEASUREMENTS WITH L- AND S-BAND SIGNALS OF OPPORTUNITY (SOOP) REFLECTOMETRY

Chapter 5 will present the wind speed retrieval results of the Purdue-NRL L- and S-band SoOp experiment as well as the application of the Small Slope Approximation (SSA) model for improving low wind retrieval. First, the wind speed retrievals (obtained with the KA-GO model) and comparisons with buoy data for the 2016 Maine and 2017 Carolina Offshore airborne experiments will be shown in Section 5.1. In Section 5.2, the anomalies found in the retrievals will be discussed, the effect of antenna gain patterns on MSS estimation will be analyzed and possible corrections will be tested. Section 5.3 will review the two widely known bistatic scattering models (KA-GO and SSA). Section 5.4 will present the DDM equations derived from the two scattering models and plot example waveforms. Section 5.5 will apply the SSA model to the NRL data set and demonstrate improvement of low wind retrievals compared with the results obtained with the conventional KA-GO model.

5.1 Wind Speed Retrieval And Comparison

5.1.1 2016 Maine and 2017 Carolina Experiment Results

The 2106 Maine and 2017 Carolina Offshore airborne experiment was conducted jointly by Purdue University and NRL to overfly NOAA weather data buoys and underfly CYGNSS. The goal was to obtain high resolution reflectometer and radiometer data for combined retrieval of MSS, Sea surface salinity and wind speed on the continental shelf. Airborne instruments included a custom-built 4-channel dual-pol L-band (GPS) and S-band (XM Radio) signal collection system for reflectometry.

The system recorded 14-bit complex samples at a sample rate of 4 MHz using a center frequency of 2.343125 GHz. It used four Universal Software Radio Peripheral (USRP) devices to digitize the signal and rack-mounted servers to stream the data to high capacity hard disks. A software defined radio (SDR) approach was used in post-processing. A digital filter was first applied to separate the signals from two satellites transmitting within the receiver bandwidth, then separate files were generated for XM3 (2344.045 MHz) and XM4 (centered at 2342.205 MHz). Filtered signals were cross-correlated using code developed to utilize an NVIDIA Tesla Graphics Processing Unit (GPU) for higher numerical performance. The cross-correlation waveforms were then fitted to the scattering models based on KA-GO, which produced surface wind speed retrievals.

Figure 5.1 presents aircraft track examples from the 2016 and 2017 experiments. These are of two main types; straight flights over buoys, and multiple buoy crossings from different angles. The 2016 trajectories are also color-coded by wind speed to show retrieved wind variations along the flight track. Red dots mark locations of nearby CYGNSS measurements (lower right plot, Figure 5.1).

Figure 5.2 shows wind speeds retrieved during four flights from S-band and L-band reflectometry, and nearby buoys. Several anomalous spikes appear in the XM wind retrievals in Figure 5.2, which are associated with certain flight heading angles. GPS results showed no such dependence. Excluding the anomalies, retrieved winds agree with nearby buoy data.

5.1.2 Comparison with Buoys and CYGNSS

Airborne data meeting the spatial constraint of distance < 10 km were selected for comparison with buoys. Buoy wind speed data were linearly interpolated to the time of corresponding airborne data. Empirical L- and S-band GMFs were used for wind speed retrievals. For each CYGNSS measurement, the airborne measurements that meet the constraint of time difference < 3600 s were first selected, and then the

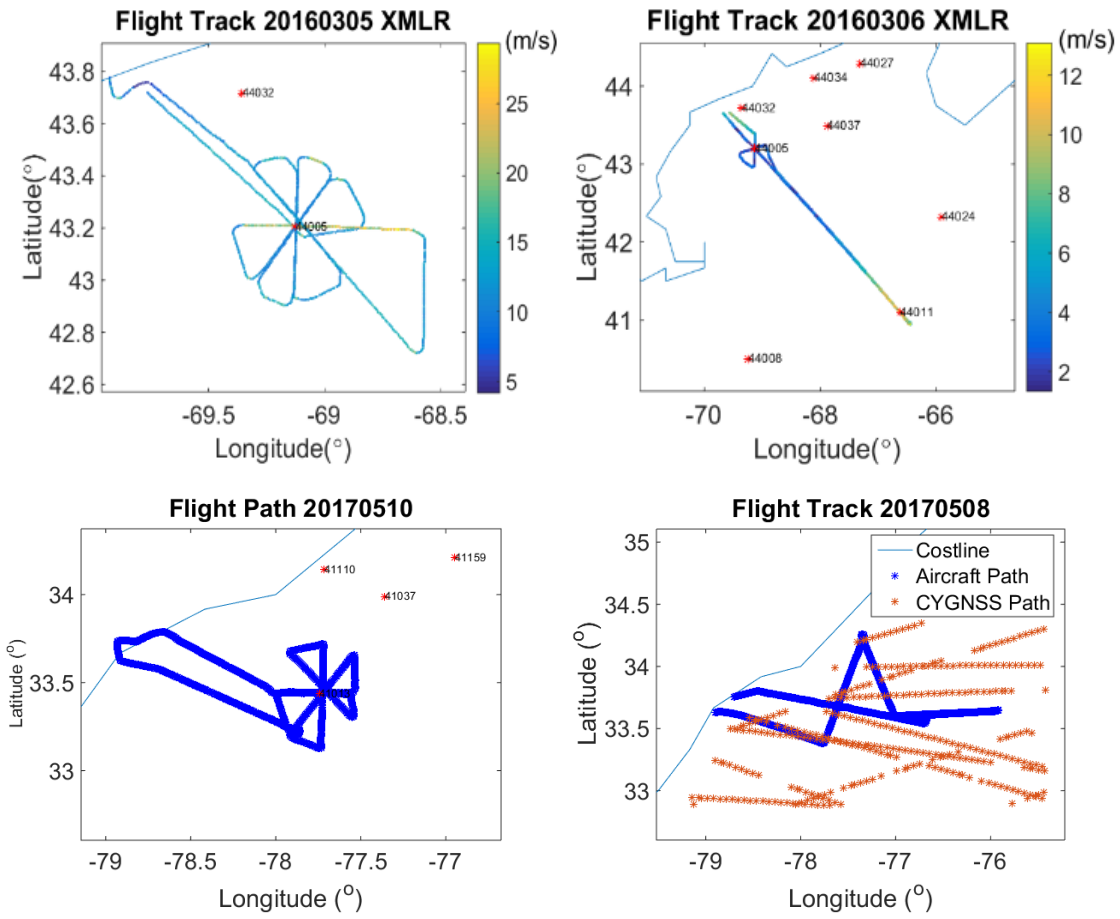

Figure 5.1. Flight track examples (top: 2016 experiment; bottom: 2017 experiment).

one closest in space was used for comparison (within a few kilometers). The CYGNSS wind speeds used were derived from both the NBRCS (Normalized Bistatic Radar Cross Section) and the LES (Leading Edge Slope) observables [45].

Excluding the anomalous measurements associated with certain heading angles, the S- and L-band measurements are generally close to buoy data (bias mean: 0.59 m/s; RMS: 1.33 m/s), as shown in Figure 5.3. This validates the new S-band geophysical model function. Figure 5.4 shows that the retrieved airborne and CYGNSS wind speeds are also generally consistent.

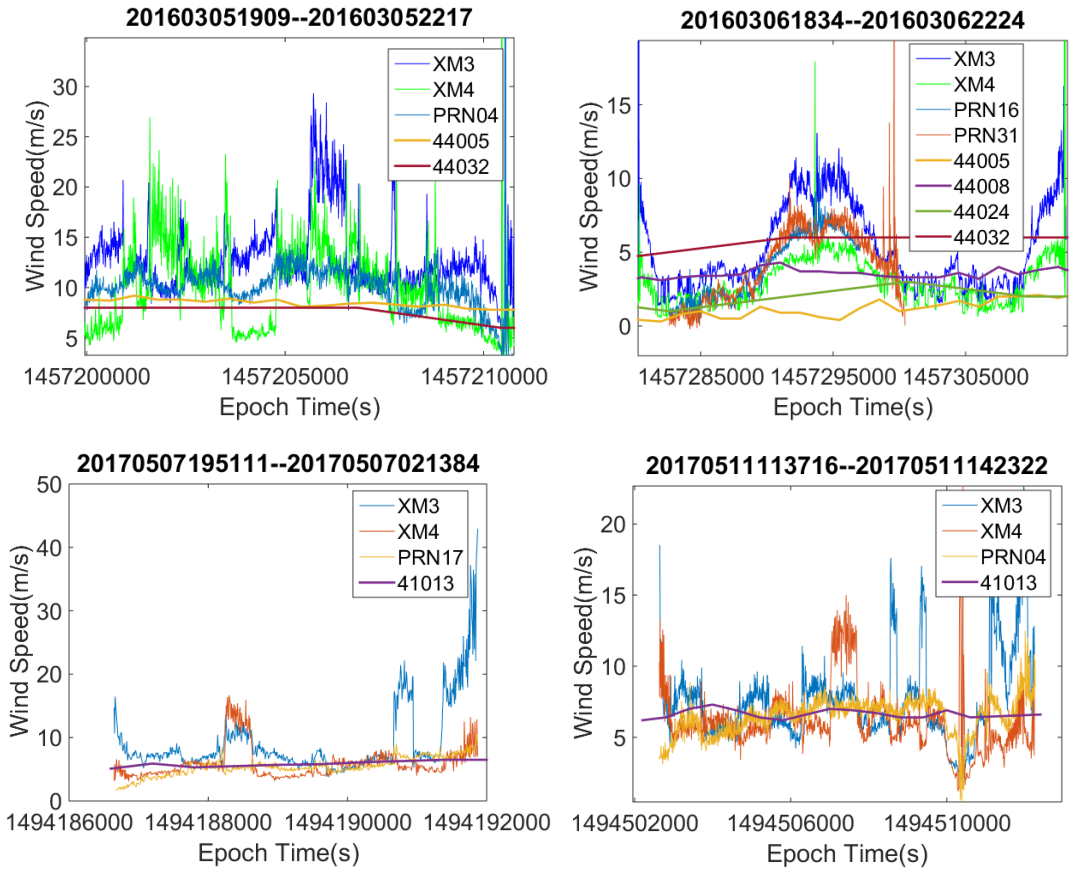

Figure 5.2. Wind speed retrieval and comparison with nearby buoys (top: 2016 experiment; bottom: 2017 experiment).

5.2 The Effect of Antenna Gain Patterns on MSS Estimation

5.2.1 Azimuth Dependence of MSS Measurements

In addition to the anomalous wind speed retrievals observed in Figure 5.2, Figure 5.5 presents a clear dependence of MSS measurements on flight heading. This anomalous azimuthal dependence could result from strong antenna pattern gradients in regions of low elevation angles. The metal antenna mounting plates might also contribute to antenna gain anisotropy in both elevation and azimuth. To analyze these effects and correct the MSS estimate, two approaches were adopted in char-

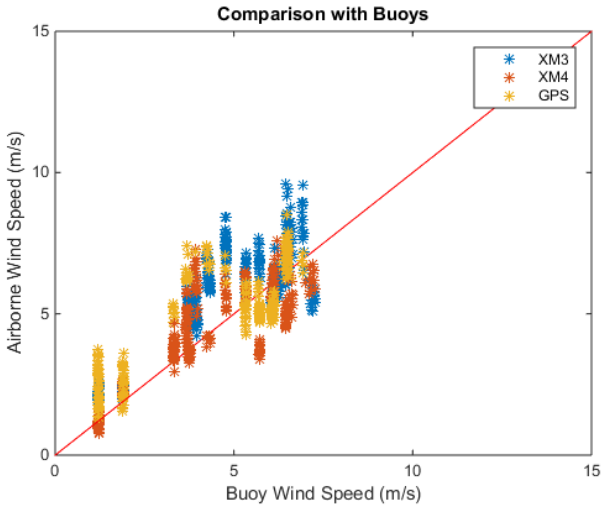

Figure 5.3. Comparison between the wind speed measurements of airborne reflectometry and nearby buoys.

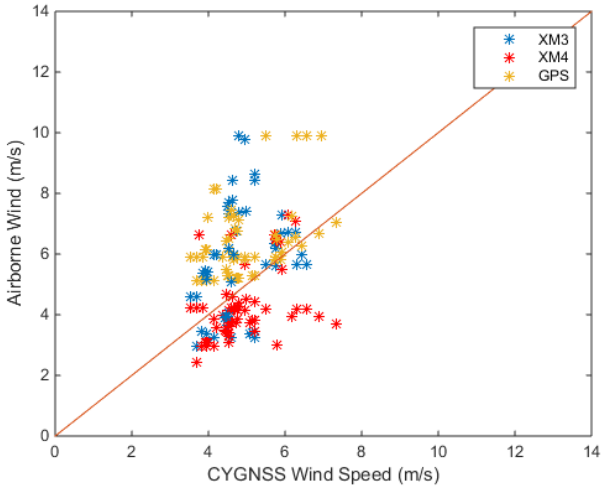

Figure 5.4. Comparison between the wind speed measurements of airborne reflectometry and CYGNSS.

acterizing the antenna gain pattern. These included computational estimation and experimental testing.

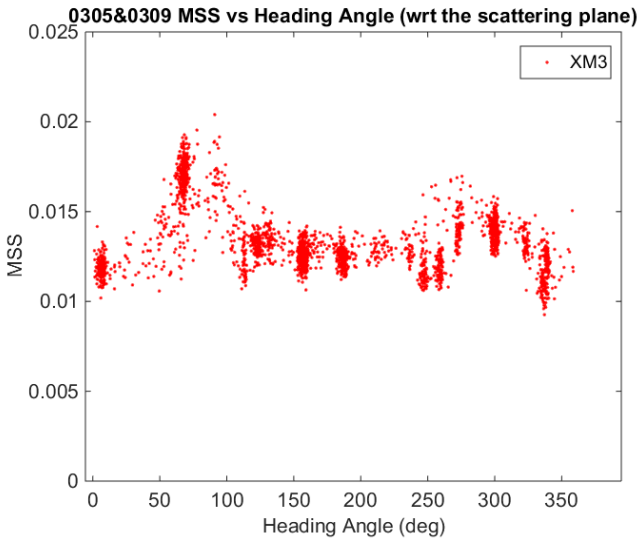

Figure 5.5. Azimuth dependence of MSS measurements.

5.2.2 Antenna Gain Pattern Estimation and Evaluation

Using our S-band GMF, MSSs can be directly derived from true wind speed measurements of nearby buoys. This provides a way to estimate the antenna gain pattern by following the same model inversion approach used in MSS estimation. For this purpose, a 3rd-order Fourier series with unknown coefficients was applied to construct the antenna gain model.

$$D(\phi, \theta) = 1 + A(\phi)[cos(2\theta) - 1] \tag{5.1}$$

where

$$A(\phi) = a_0 + \sum_{i=1}^{3}[a_i cos(\omega\phi) + b_i sin(\omega\phi)] \tag{5.2}$$

ϕ and θ are azimuth and elevation angles respectively, and a_i, b_i and ω are unknown coefficients.

MSS values converted from buoy wind speed data were used as a priori ground truth to estimate the coefficients of the gain model, by minimizing the differences between modelled and observed correlation waveforms. As Figure 5.6 shows, only the data collected close to the corresponding buoy were included in the estimation.

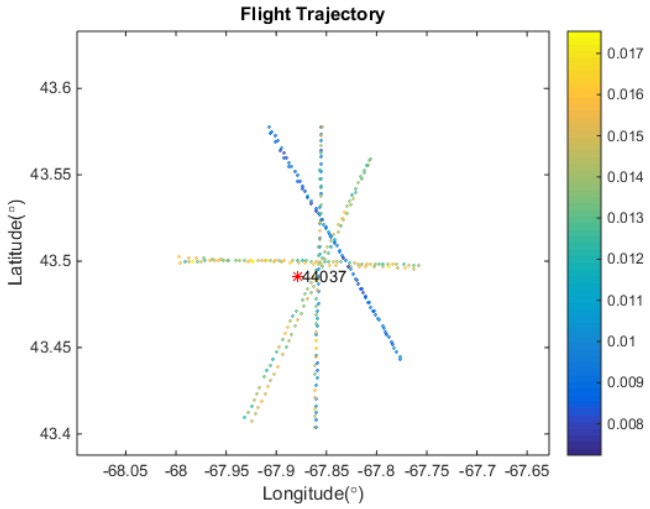

Figure 5.6. Data samples along the flight track around the buoy.

Estimated gain pattern variations with respect to elevation and azimuth are plotted in Figure 5.7. These estimates were also used to correct the MSS estimates and evaluate the performance. Figure 5.8 compares the MSS obtained with and without the antenna gain pattern correction. The results show significant reduction of the MSS dependence with flight direction/azimuth angle when using the estimated antenna gain model.

5.2.3 Antenna Gain Pattern Measurement and Evaluation

In addition to the pattern estimation, the antenna gain patterns, both with and without mounting plates, were also measured in a chamber by a third-party antenna testing company [https://antennatestlab.com/]. As an example, Figure 5.9 shows the measured XM RHCP antenna patterns with and without mounting plate (vertical cut of 80 deg. azimuth angle). Strong variations of the antenna gain pattern with respect to the azimuth can be observed in the low elevation regions. The results show a significant contribution of the mounting plate to the antenna pattern irregularities.

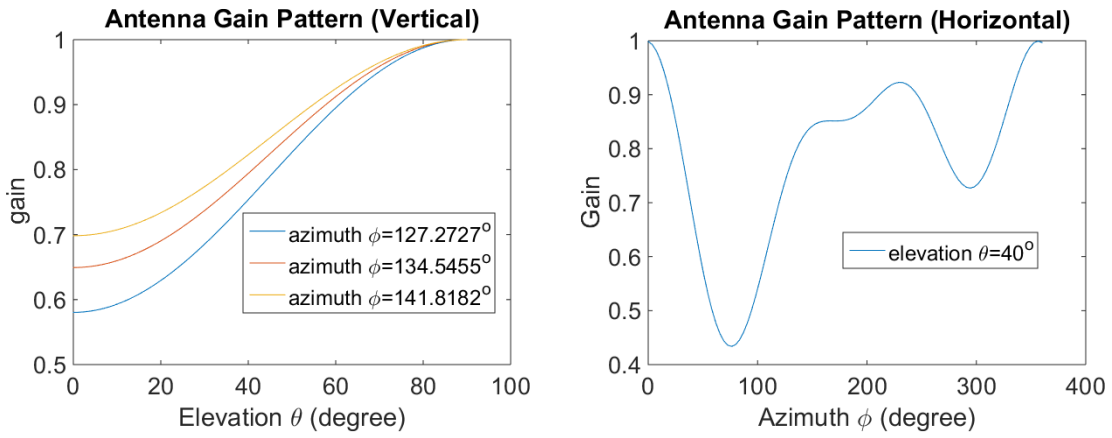

Figure 5.7. Vertical (left) and horizontal (right) cuts of the estimated antenna gain pattern.

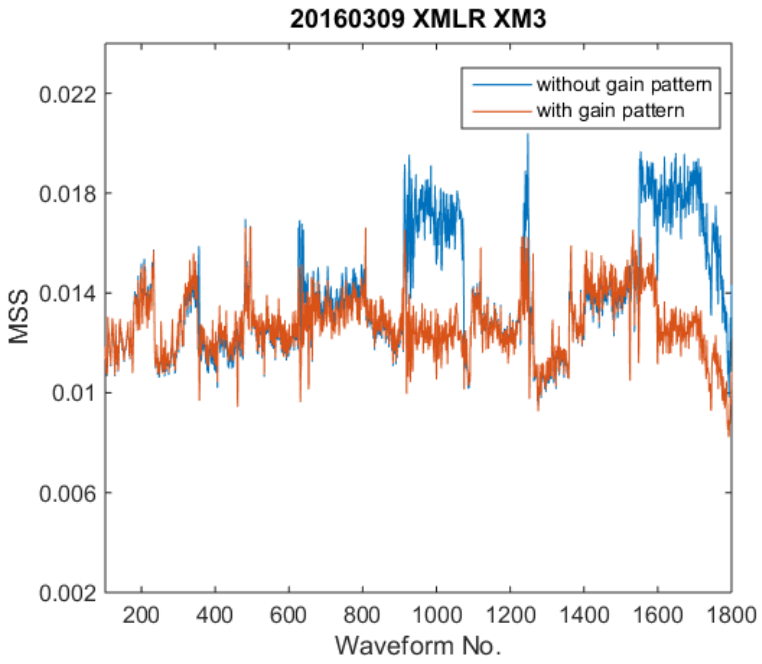

Figure 5.8. MSS estimates with and without the estimated antenna gain pattern.

These measured antenna gain patterns were incorporated in the forward model for MSS retrieval and the results were analyzed. Data associated with certain elevation angles show a good error mitigation with the gain pattern corrections, while others

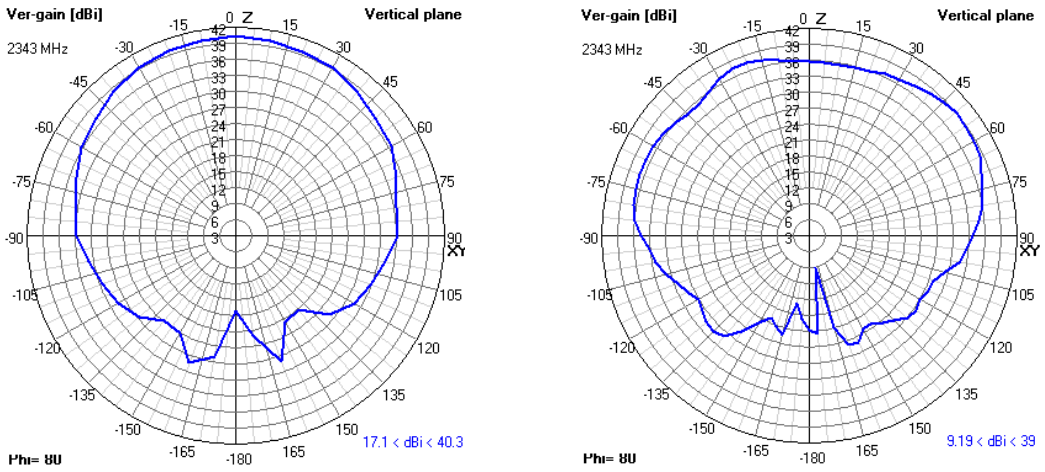

Figure 5.9. XM RHCP antenna patterns (80 deg. azimuth angle cut; left: without plate; right: with plate).

didn't behave as expected. Figure 5.10 shows some examples of the results. Possible reasons for the unpromising results include: (1) the orientations of the aircraft, especially the yaw angle associated with the wind were not measured; (2) installation misalignment between the antennas and the aircraft; (3) the effects of other external factors (such as electrical properties of nearby devices and the aircraft itself), which could also distort the antenna gain patterns.

5.3 Bistatic Scattering Models

The commonly used KA-GO model for GNSS-R is derived based on the assumption of strong diffuse scattering. This model would produce an incorrect result for the case of weak diffuse scattering, or in the presence of coherent reflection. A new scattering model and bistatic radar function was thus developed by Voronovich and Zavorotny using the SSA, which allows the transition from partially coherent scattering to non-coherent, strong diffuse scattering to be correctly described. This section describes details of the KA-GO and SSA bistatic scattering models, gives their expressions for bistatic radar cross sections (BCRS) and compares the BCRS values generated under different wind speed conditions.

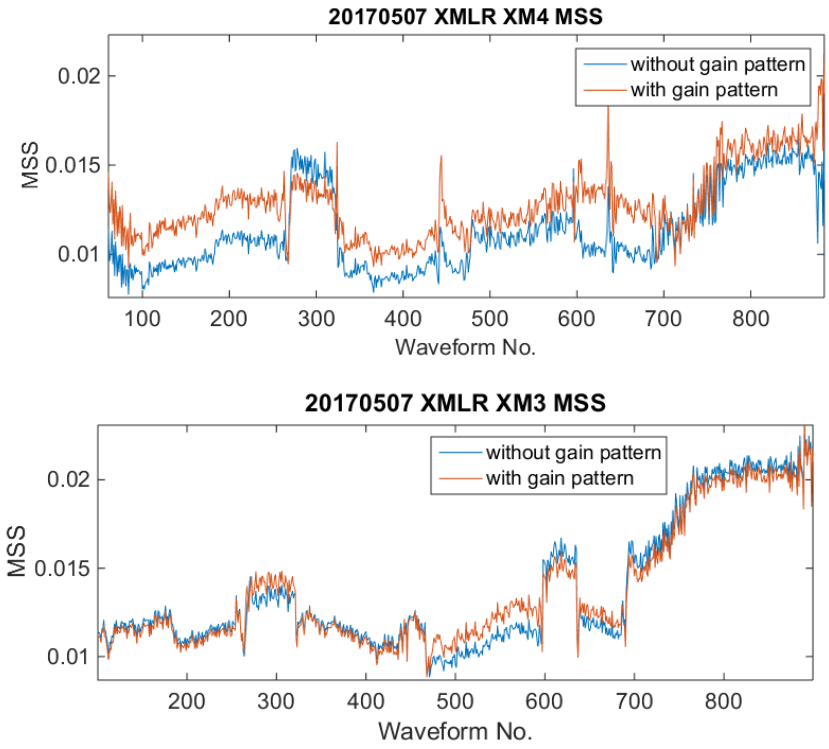

Figure 5.10. Wind speed retrievals with and without measured patterns (top: promising result, 37.5 deg. elevation; bottom: unpromising result, 50 deg. elevation).

5.3.1 Geometric Optics (KA-GO)

The KA-GO model was derived based on the geometric optics limit of the Kirchhoff approximation. The DDM waveform constructed with the KA-GO model depends on a wave-slope PDF, which in turn depends on wind speed. This model is only valid in the case of the diffuse scattering regime, which ignores the contribution of the coherent bistatic scattering component. The expression for the diffuse scattering cross section in the KA-GO model is:

$$\sigma_{GO}(\vec{\rho}) = \frac{\pi |\Re|^2 q^4(\vec{\rho})}{q_z^4(\vec{\rho})} P_{\vec{v}}(-\frac{\vec{q_\perp}}{q_z}) \tag{5.3}$$

where $|\Re|^2$ is the local Fresnel coefficient, $\vec{q}$ is the scattering vector and $P_{\vec{v}}$ is the probability function of ocean surface slopes. More details about this expression are included in [1].

5.3.2 Small Slope Approximation (SSA)

The SSA model defines an expression for BRCS using a formulation based on the small slope approximation of the first order (SSA1). Unlike most currently used bistatic scattering models (e.x. KA-GO), the SSA model is not constrained by the regime of strong diffuse scattering or large Rayleigh parameter R_a. In fact, this model can describe the transition from partially coherent scattering to completely non-coherent, strong diffuse scattering. The situation of weak diffuse scattering may occur for scattering of GNSS signals or other SoOps from a rough ocean surface under low winds, so it is expected that the SSA model can provide better accuracy for low wind speed retrievals. In this thesis, the expression for the diffuse scattering cross section in the SSA1 model is

$$\varepsilon(\vec{k},\vec{k_0}) = |\overline{V}(\vec{k})|^2\delta(\vec{k}-\vec{k_0}) + \frac{1}{4\pi q_k q_{k0}}\sigma_{SSA}(\vec{k},\vec{k_0}) \tag{5.4}$$

This expression contains both the coherent component (the first term) and the non-coherent component (the second term) which take the following forms.

$$\overline{V}(\vec{k}) \approx e^{-2R_a^2}V_F(\vec{k}) \tag{5.5}$$

where $V_F(\vec{k})$ is Fresnel coefficient, R_a is the Rayleigh parameter and for large values of R_a,

$$R_a = q_k\langle h^2\rangle^{\frac{1}{2}} \tag{5.6}$$

and

$$\sigma_{SSA}(\vec{k},\vec{k_0}) = |B(\vec{k},\vec{k_0})|^2\frac{4q_k^2q_{k_0}^2}{\pi(q_k+q_{k_0})^2}\times e^{-(q_k+q_{k_0})^2W(0)}\int e^{-i(\vec{k}-\vec{k}_0)\vec{\rho}}\times(e^{(q_k+q_{k_0})^2W(\rho)}-1)d\vec{\rho} \tag{5.7}$$

where $\bar{V}(\vec{k})$ is the average reflection coefficient and $\sigma_{SSA}(\vec{k},\vec{k_0})$ is the diffuse scattering cross section.

The expression for σ_{SSA} (5.7) contains the same integral as the expression for σ_{GO} (5.3) obtained with the KA-GO, but the pre-integral factor is different. The greatest difference between the KA-GO and the SSA1 is that the correlation function $W(\vec{\rho})$ in

(5.7) is not considered to be slowly varying and may include small-scale components responsible for Bragg scattering. More discussions and comparisons related to the two models can be found in [35] [46] [47].

Figure 5.11 plots the S-band bistatic radar cross sections for 34 deg. and 50 deg. elevation angles. The wave vector $[kx/k, ky/x]$ defined in [15] was represented by a 512×512 gridded map covering values from [0, 0] up to [1, 1]. The non-coherent part of BRCS modeled with SSA shows a bimodal phenomenon in the case of small Rayleigh parameters.

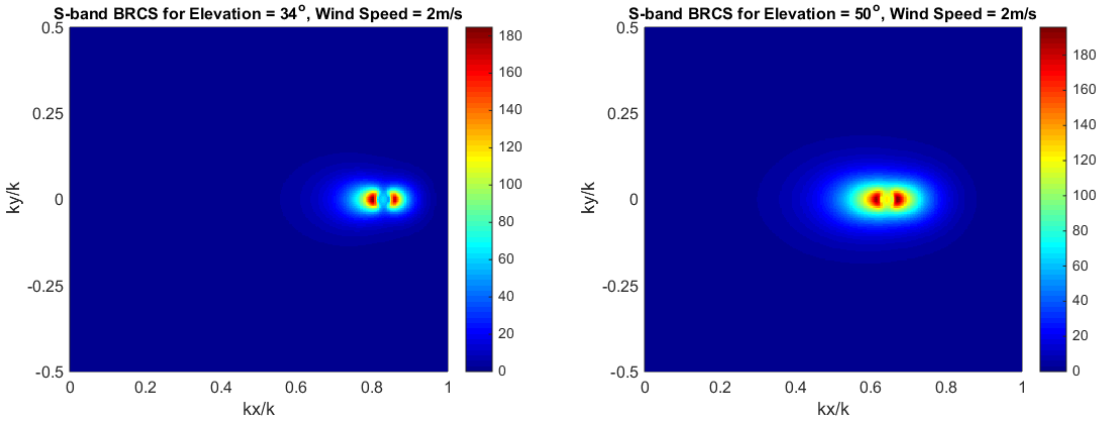

Figure 5.11. Bistatic radar cross section (S-band BRCS for elevation 34 deg. and 50 deg.).

5.3.3 BCRS Comparison

Figure 5.12 shows the comparison of BCRS in the specular direction between KA-GO and SSA under different wind speed conditions. The incident angle is 30 deg. and the receiver altitude is 5000 m. The dielectric constant ϵ of sea water for L-band signals was chosen as $74.44 + i49.88$. The incidence plane and the wind direction are aligned, although it does not matter in this case as the BCRS in the specular direction is not sensitive to the wind direction. The ocean surface roughness was assumed to

obey the Elfouhaily wave spectral model discussed in Section 3.4.4. Comparison of BCRS shows a smooth transition from KA-GO to SSA at $U_{10} > 6$ m/s.

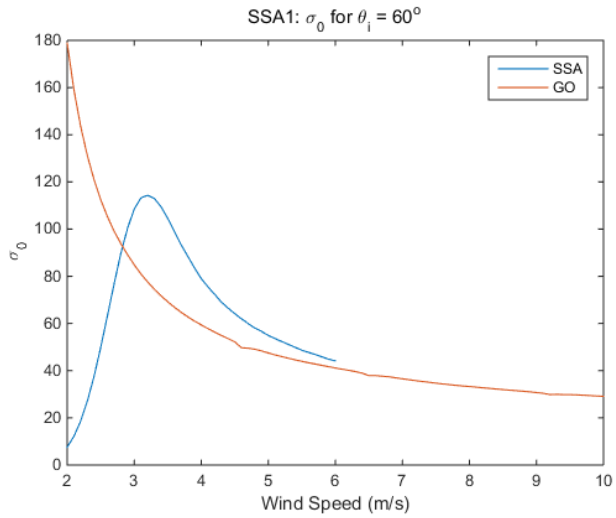

Figure 5.12. Comparison between BRCSs of SSA and KA-GO.

5.4 DDM Simulation and Comparison

The difference between the BCRS expressions for the two models defines different DDM shapes that will eventually influence the retrieved MSSs and wind speeds. This section simulates and compares the DDMs derived with KA-GO and SSA models respectively, under a highly simplified scenario. The detailed derivations of the DDM expressions for KA-GO and SSA can be found in [1] and [16].

5.4.1 Implementation Details

The basic parameters for the implementation have the same settings as those used in the BRCS simulation. The incidence angle is 30 deg., the receiver altitude is 5 km and seawater dielectric constant is $74.44 + i49.88$. The incidence plane and the wind direction are aligned. Additionally, for simplicity, the transmission power and antenna gain pattern are both set to unity. The GPS satellite and receiver are

assumed static. Expressions of the DDM will be introduced below. More details of related derivations and notations can be found in the Appendix.

SSA

The total correlation waveform with the SSA model is a combination of two components: coherent and non-coherent.

$$\overline{|Y(\tau,\omega_D)|^2} = \overline{|Y(\tau,\omega_D)|_c^2} + \overline{|Y(\tau,\omega_D)|_{nc}^2} \tag{5.8}$$

The coherent part is expressed as:

$$\overline{|Y(\tau,\omega_D)|_c^2} = P_{tr}|D_{tr}(\vec{n}_*,\omega_0)D_{rec}(\vec{m}_*,\omega_0)|\times < |\chi(\tau - \frac{R_*}{c},\delta w_*,\beta_*)|^2 > \frac{|\bar{V}(\vec{n}_{*\perp},\omega_0)|^2}{R_*^2} \tag{5.9}$$

As mentioned above, the transmission power and antenna gains are both set to unity, i.e., $P_{tr} = D_{tr} = D_{rec} = 1$. The GPS satellite and receiver are considered static. The waveforms are centered at zero delay. Also, $R_* \approx R_0$, where R_0 is the distances between the scattering element and the transmitter. So for the coherent part, the actual function was implemented in the following form:

$$\overline{|Y(\tau)|_c^2} =< |\chi(\tau)|^2 > \frac{|\bar{V}(\vec{n}_{*\perp})|^2}{R_0^2} \tag{5.10}$$

The non-coherent part is expressed as:

$$\overline{|Y(\tau,\omega_D)|_{nc}^2} = \frac{P_{tr}}{4\pi}\int\int \frac{|D_{tr}(\vec{m}_\perp,\omega_0)D_{rec}(\vec{n}_\perp,\omega_0)|}{R_0^2R^2}\times \tag{5.11}$$

$$< |\chi(\beta\tau - \frac{R_0+R}{c},\delta w,\beta_*)|^2 > \sigma_0(\vec{n}_\perp,\vec{m}_\perp;\omega_0)d\vec{\rho} \tag{5.12}$$

With the same configurations as described for the coherent component, the actual function for the coherence part was implemented in the following form:

$$\overline{|Y(\tau)|_{nc}^2} = \frac{1}{4\pi}\int\int \frac{1}{R_0^2R^2} < |\chi(\tau)|^2 > \sigma_{0(SSA)}d\vec{\rho} \tag{5.13}$$

KA-GO

Assuming $P_{tr} = D_{tr} = D_{rec} = 1$, the KA-GO waveform takes the following form:

$$\overline{|Y(\tau)|^2_{nc}} = \int\int \frac{1}{R_0^2 R^2} < |\chi(\tau)|^2 > \sigma_{0(GO)} d\vec{\rho} \tag{5.14}$$

5.4.2 Results

Comparison of the DDM peak values obtained using SSA and KA-GO showed that, at low wind speed, the KA-GO model inaccurately predicts the behavior of the DDM, giving lower peak values compared to the results from the SSA model. Thus, theoretically, the SSA model will produce higher wind speed estimates with the DDMA wind retrieval approach developed for CYGNSS, which converts the absolute scattering powers around the reflection point to wind speeds.

The left plot in Figure 5.13 shows the waveforms of the SSA coherent part under low to medium wind speed conditions. It can be observed that the coherent part increases dramatically when the wind speed reduces to 2 m/s. This is expected, given the exponential term in the expression for the coherent part of BRCS. The right plot in Figure 5.13 shows the SSA waveforms of the non-coherent components for different wind speeds. The waveforms generally have the behaviors of increased power with respect to reduced wind speed. This can be explained by the rapid decrease in the BRCS when wind speed drops below about 3 m/s. The left plot in Figure 5.14 shows the KA-GO and SSA waveforms together for comparison. In order to make the comparison clearer, only 2 m/s and 5 m/s waveforms were shown in the right plot in Figure 5.14.

As can be seen in these plots, the SSA and KA-GO models are generally in close agreement. The KA-GO peak power is always higher than the SSA even though the KA-GO produces lower BRCS values than SSA in specular directions. This is because the value of each point in the DDM is essentially obtained by an integration over an area on ocean surface, which does not rely on single BCRS values in a certain direction.

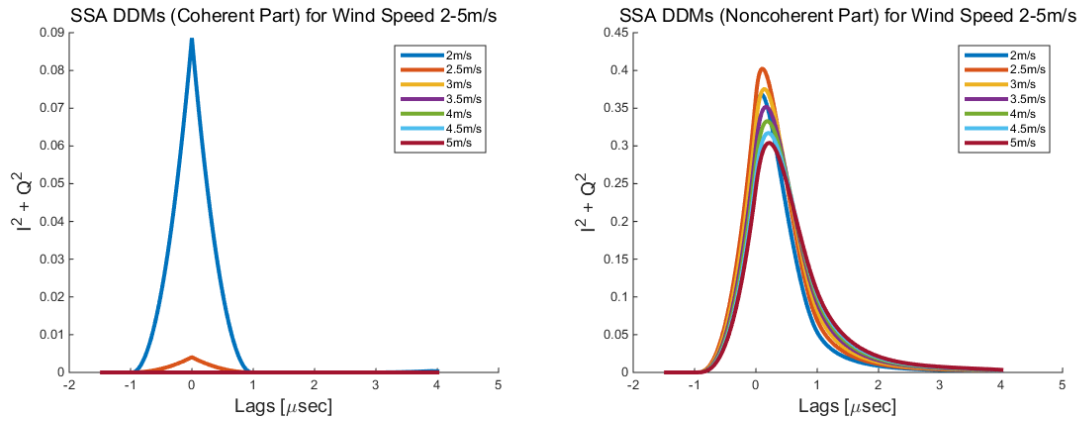

Figure 5.13. SSA DDMs (coherent part and non-coherent part).

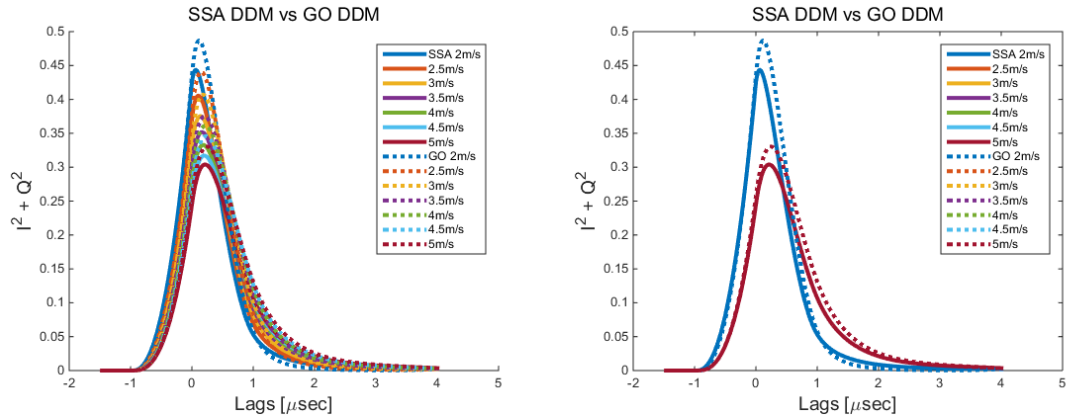

Figure 5.14. SSA DDMs vs KA-GO DDMs for wind speeds 2-5m/s.

5.5 Wind Speed Retrieval and Comparison

SSA bistatic radar cross sections for L-band GPS signals and S-band XM3 and XM4 signals were firstly generated independently and saved as a lookup table that covers wind speeds from 1 to 5 m/s with a 0.1 m/s increment. For each point on the ocean surface, the wind speed retrieval program calculates the wave vector in the scattering plane, finds the closest grid point from the lookup table then take the corresponding BRCS value into computation. For this thesis, the KA-GO model assumes

an isotropic Gaussian distribution of surface slopes and the SSA model assumes a wind direction aligned with the scattering plane.

Figure 5.15 shows comparisons of wind speed retrievals between KA-GO, SSA and in situ data. The linear fits of retrievals vs in situ measurements are also plotted. It can be noticed that generally the retrievals at low wind speeds under KA-GO are higher than the in situ measurements. The SSA model produces lower wind speed retrievals than those obtained with the KA-GO model. The statistics of the retrieval performance are summarized in Tables 5.1 and 5.2. It shows that SSA has improved the accuracy of low wind speed retrievals as indicated by the linear fit, mean bias and root-mean-square error (RMSE).

Table 5.1. Mean bias comparisons between KA-GO and SSA wind speed retrievals.

	KA-GO	**SSA**
XM3	1.38m/s	1.03m/s
XM4	1.73m/s	1.18m/s
GPS	0.74m/s	0.37m/s

Table 5.2. RMS comparisons between KA-GO and SSA wind speed retrievals.

	KA-GO	**SSA**
XM3	1.44m/s	1.10m/s
XM4	1.81m/s	1.32m/s
GPS	0.86m/s	0.75m/s

5.6 Conclusions

This chapter described the results of two L- and S-band reflectometry experiments conducted in 2016 and 2017. Comparisons showed that the airborne wind speed retrievals are generally close to those obtained from buoys and CYGNSS measurements. This demonstrated the effectiveness of our proposed S-band model and provided a preliminary validation of CYGNSS. MSS estimates also showed a strong azimuthal dependence with respect to the flight heading angles, which was determined to be induced by the irregularity of the antenna pattern. Both computational and experimental approaches were attempted to estimate the antenna patterns. The results showed the mounting plate has a significant effect on these patterns. Pattern corrections produced promising wind speed retrievals in several cases, while reasons for unpromising results using the measured patterns were discussed. Retrieved wind speed were obtained using the SSA model and the results showed improved retrieval performance in low-wind regime.

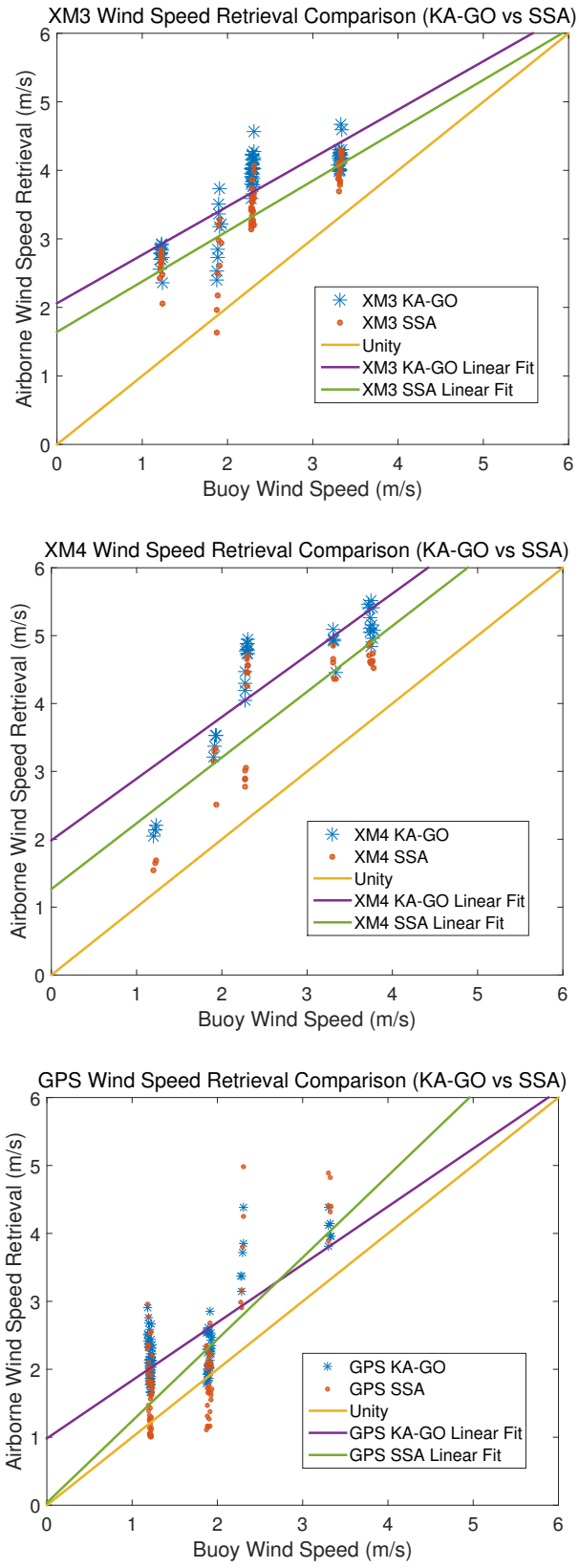

Figure 5.15. Wind speed retrieval comparison between SSA and KA-GO for XM3, XM4 and GPS.

6. CYGNSS WIND SPEED RETRIEVAL WITH AN EXTENDED KALMAN FILTER

Chapter 6 will present the results of the EKF-based multi-look DDM processing method for CYGNSS spaceborne wind speed retrievals. The problem will be formulated and the EKF-based algorithm will be described in Section 6.1. Modifications of the EKF algorithm and forward model for actual CYGNSS data processing (w.r.t. simulated cases) will be discussed in Section 6.2. The results obtained by processing actual CYGNSS data will be shown in Section 6.3. Section 6.4 will discuss possible error sources for the EKF-based multi-look DDM processing algorithm. Section 6.5 will conclude this chapter.

6.1 Problem Formulation

The EKF-based wind speed retrieval method utilizes the orbital motion of the GPS satellites. As the glistening zoom moves with the GPS satellites, each point on the ocean surface is actually covered by a sequence of consecutive DDMs. Therefore, if we treat the gridded ocean wind field as a set of state vectors, the DDMs can be considered as observation vectors which provide innovations to the states. This is the general idea of the EKF-based wind speed retrieval method. More detailed derivation can be found in [17]. For the actual EKF implementation, the state vector X comprises batches of 7-sec DDM sequences. The observation vector Y contains the 10-km gridded wind field in a 120×120 km area (144 states). The observation matrix H is the discretized scattering model.

The flow chart is shown as Figure 6.1. CYGNSS L1a data are the measured DDMs y_k. The wind speed values estimated from the CYGNSS MV (Minimum Variance) observable method is applied to initialize the state vector which is the gridded wind

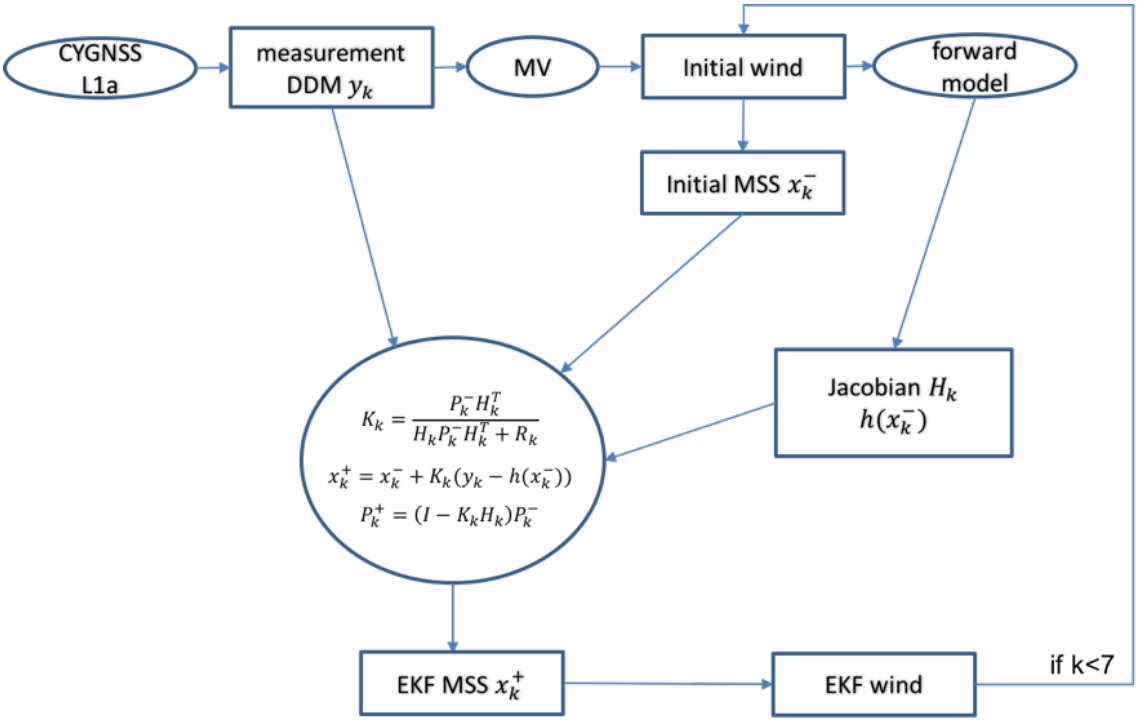

Figure 6.1. EKF flow chart.

field in the glistening zone. Sea surface roughness parameter, MSS, was obtained from wind speed using Katzberg's L-band empirical model. The MSS states defined in the Lat/Lon frame, X_{kll}, are converted to those defined in the specular frame, X_{ksp}, by linear interpolation, which are then incorporated into the EKF processing. The Jacobian matrix H is calculated using the discretized scattering model and evaluated with the current states. Updated state vector, X_{ksp}^+, defined in the specular frame is obtained from the EKF algorithm. At the last step of the first iteration, X_{ksp} is used to update the state vector in the Lat/Lon frame, X_{kll}, using the nearest neighbor method. At the time of each succeeding DDM, the motion of glistening zone and specular frame defines a new coordinate transformation between state vectors in the Lat/Lon frame and those in the specular frame. The final MSS estimates are obtained by continuing this process for up to 7 iterations, after which they are converted to a wind speed field using Katzberg's model.

6.2 Modifications of EKF and Forward Model for Actual CYGNSS Data Processing

(1) Redefined state vectors in the latitude/lontitude (Lat/Lon) frame

The simulation work performed in [17] was done with state vectors defined in the specular frame. In this case, as the EKF algorithm iterates, the wind speed estimate for each grid point actually becomes an averaged wind speed over the area swept by the grid point. A more precise representation of the problem can be obtained through use of a redefined state vector in the Lat/Lon frame, which is, instead, fixed with respect to the Earth. In this way, each grid point in the Lat/Lon frame becomes a separate individual state, without any overlaps with other grid points.

There are two ways to accomplish this conversion. The first method has already been illustrated in Section 6.1. This method involves the conversion of the specified grid between the Lat/Lon frame and specular frame. In each iteration, the wind speed values of the grid points in the two frames are connected using the nearest neighbor method. The second method requires no transformations between the grids in the Lat/Lon and specular frames. Instead, the specular frame coordinate of each Lat/Lon-frame grid point is directly calculated and used in EKF processing. The Jacobian matrix obtained is directly related to each grid point in the Lat/Lon frame. This thesis is focused on the first method.

(2) Obtaining the geographic locations of specular points from L2 data instead of calculating them locally

The CYGNSS post-processing program calculates the geographic locations of specular points using a more accurate method and this information is contained in the CYGNSS L1 and L2 data sets. So, instead of computing the coordinate locally, the value of this parameter is directly obtained from the CYGNSS data and incorporated into the EKF processing. The estimation of the specular point location involves

an iterative method performed using the geometry of the relative locations of the transmitting satellite and the receiving one. The L2 estimation method additionally incorporates the ocean surface height information, which makes the calculation of specular points more accurate.

(3) Using updated full antenna patterns and Fresnel coefficient at specular point

Since the launch of the CYGNSS satellites, the lack of adequate power calibration has been a major constraint on the retrieval accuracy, especially for the baseline observable method which is established using the power-wind relationship. The estimates of GPS transmission power and the CYGNSS antenna gain patterns have been continuously refined using ground instrument measurements and various data processing techniques. The latest released antenna gain pattern (v2.1) is believed to have accurately captured the in-orbit CYGNSS satellite gain pattern properties. It has also demonstrated that this v2.1 CYGNSS antenna pattern has improved the retrieval performance of both the baseline and EKF methods.

The dielectric constant of the sea surface is another important parameter affecting the reflection power of the GPS signals. However, instead of dielectric constant, which depends primarily on the sea surface temperature and salinity, CYGNSS data set only provides a single Fresnel coefficient calculated in the direction of the specular reflection. Given the fact that the Fresnel coefficient generally varies very slowly across the glistening zone for regular dielectric constant values, the same Fresnel coefficient value is applied to all grid points/all reflections, in order to simplify the problem.

(4) Removing anomalous measurements

The L1 and L2 quality flags indicate various anomalous conditions that could degrade the observations. These include anomalous attitudes of CYGNSS satellites,

signal quality, and mismatch of wind speed retrievals from two major observable method−MV (Minimum Variance) and LES (Leading Edge Slope), which may indicate some level of non-ideal signal characteristics are present. The new Block IIF set of GPS satellites, manufactured by Boeing, have a different transmission power control mechanism in comparison with previous generations. More specifically, ground power monitoring experiments have shown that the GPS transmission power of Block IIF satellites can be adjusted on-board at any time, presenting an abrupt rise and drop in the transmission power at certain points in time. This causes great difficulties in estimating and calibrating the effect of GPS transmission power on the amplitude of DDMs, which will eventually induce uncertainties in our EKF-based retrievals. As a result, DDM measurements from GPS Block IIF satellites were excluded from our data processing.

6.3 CYGNSS Results

The EKF approach has been applied to actual CYGNSS data. Figure 6.2 shows wind speed retrievals from CYGNSS data collected druing a hurricane on 1/16/2018. Wind speed from 3 different sources are presented including HWRF, the observable method and EKF method. The top row shows the entire areas of the wind speed retrievals while the bottom focuses on the hurricane center. It can be observed that the EKF approach produced more accurate wind speed estimates in hurricane regions and more clearly tracked the high wind in the hurricane core than did the observable method. Another example resulting from the CYGNSS data 2/12/2018, shown in Figure 6.2, proves that the EKF-based retrieval method can produce more detailed structure in the hurricane core than the observable method.

Data from 14 tracks were selected and processed to perform statistical analyses. An example track is shown in Figure 6.4. Firstly, wind speed retrievals obtained from the three methods were compared for each track. The results were categorized into three groups: promising results, partially promising results and unpromising results.

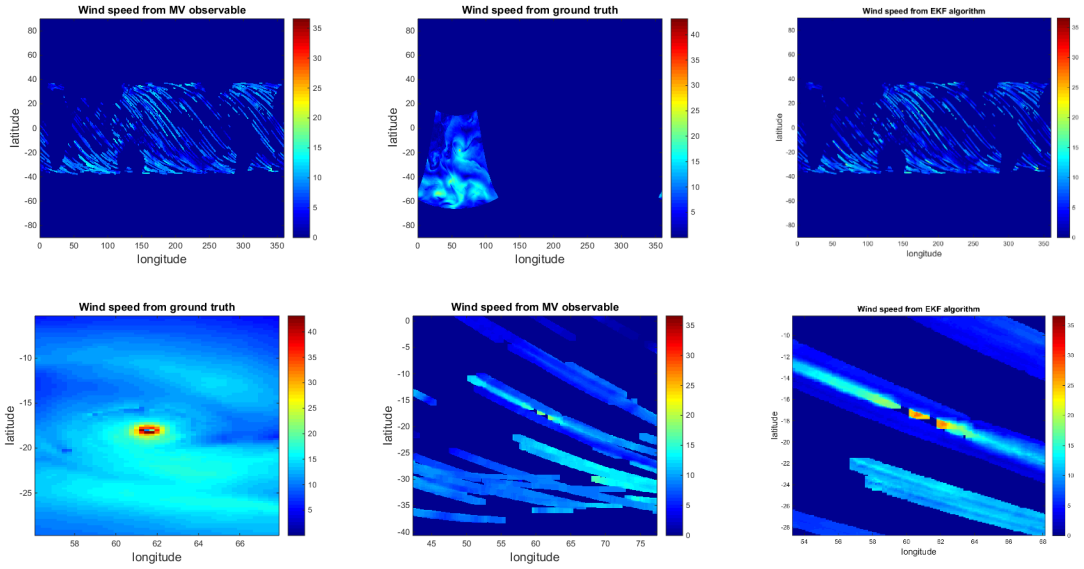

Figure 6.2. CYGNSS wind speed retrieval results with EKF (1/16/2018 data).

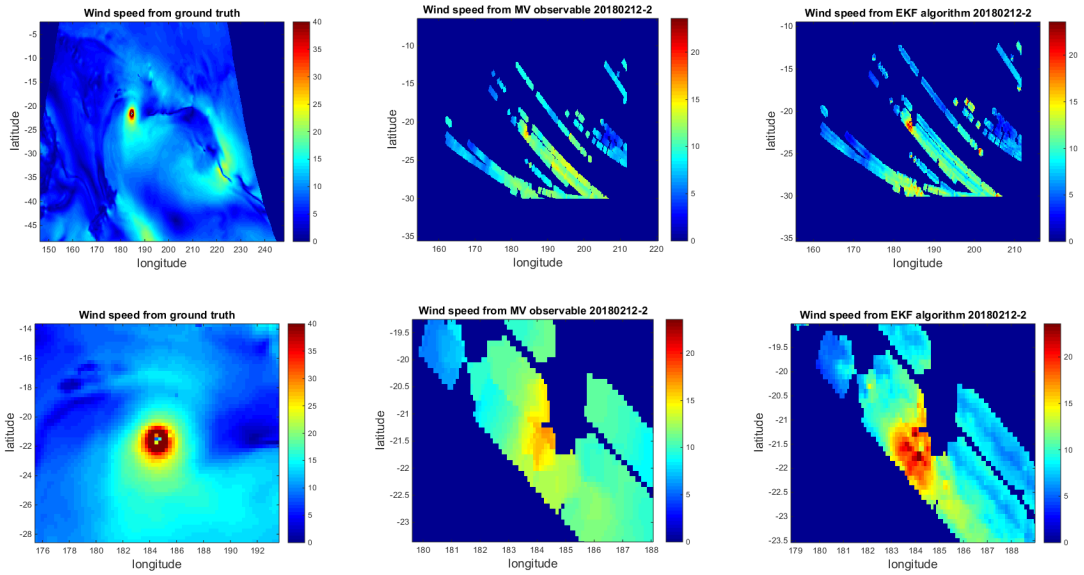

Figure 6.3. CYGNSS wind speed retrieval results with EKF (2/12/2018 data).

Figure 6.5 shows the promising results. Figure 6.6 shows the partially promising results for which some of the wind speed retrievals obtained using the EKF approach show a good match with the ground truth. For example, for the case shown in Figure

6.6, only the EKF-based results of the first about 100 seconds have a high consistency with the ground truth. The total of all promising results, including all the data in the first category and the promising part in the second category, occupies about 80% of the entire data set. Figure 6.7 shows the total EKF wind speed retrievals of the promising results compared with results from the observable method. Figure 6.8 shows that the EKF approach has a mean bias of 0.84 m/s and RMSE of 3.03 m/s and linear fit of $y = 0.9448 \cdot x + 1.639$, while the other two approaches have biases higher than 2 m/s and RMSEs higher than 4m/s.

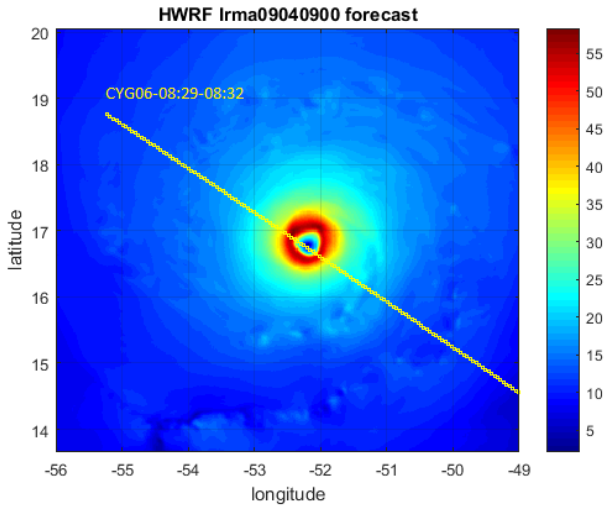

Figure 6.4. Example CYGNSS track (9/4/2018).

6.4 Error Source

6.4.1 CYGNSS Calibration

Estimations of GPS transmission power (EIRP) and CYGNSS antenna gain patterns are still the primary error sources for either the baseline observable method and the EKF method, and they are also being continuously refined to acquire improved accuracy. Great power calibration improvements have been observed in the latest v2.1 data set, which is demonstrated by improvement in the wind speed retrieval

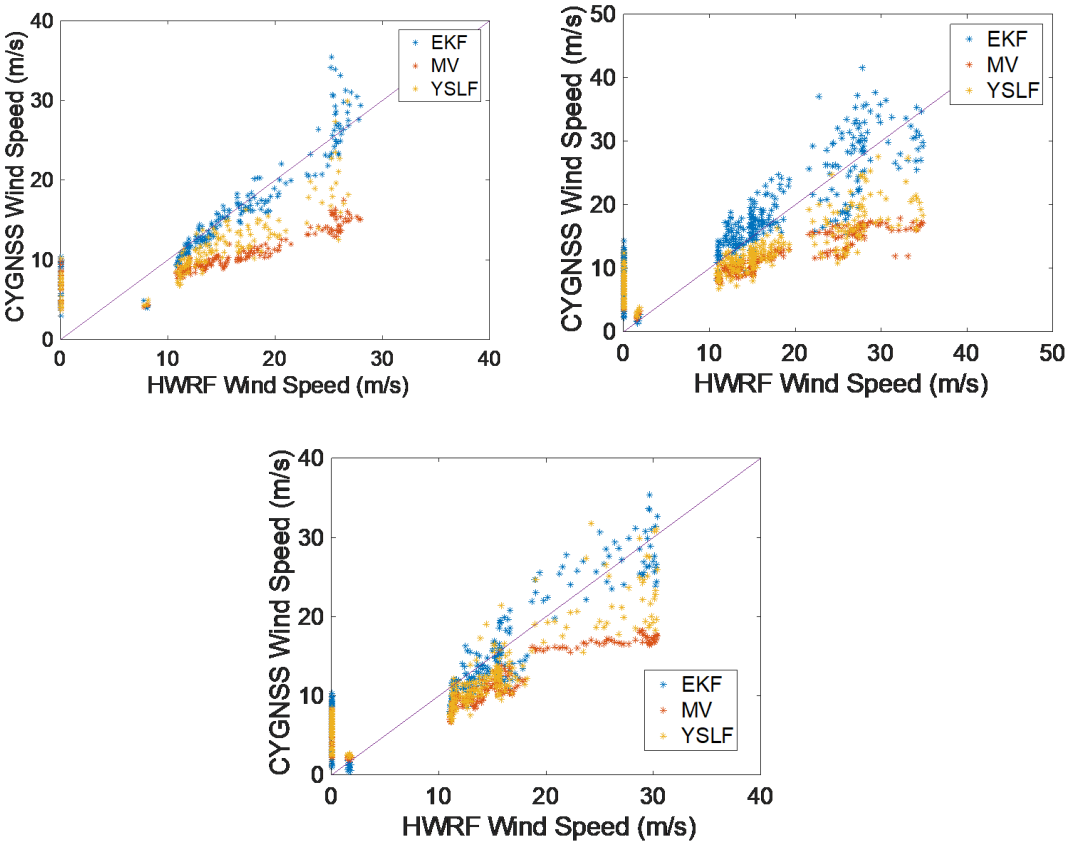

Figure 6.5. Wind speed retrieval comparison between EKF, MV and YSLF (promising results).

performance of both the observable and EKF method. The future v3.0 data plan to use signals received by the direct antenna to obtain real-time measurement of GPS EIRPs, which is expected to produce a data set which is more precisely calibrated. Estimation of DDM specular point positions is another major calibration error source for CYGNSS, which refers to the precise index (floating point number) of the specular point on each DDM. Hardware limitations introduce biases to the estimation of specular point index which directly affect the H matrix generated from the scattering model in the EKF algorithm and brings errors to MSS estimates. Another potential method to solve this problem in post processing is to add new parameters to the state vector of the EKF algorithm, to adjust the offsets in DDM power, delay and

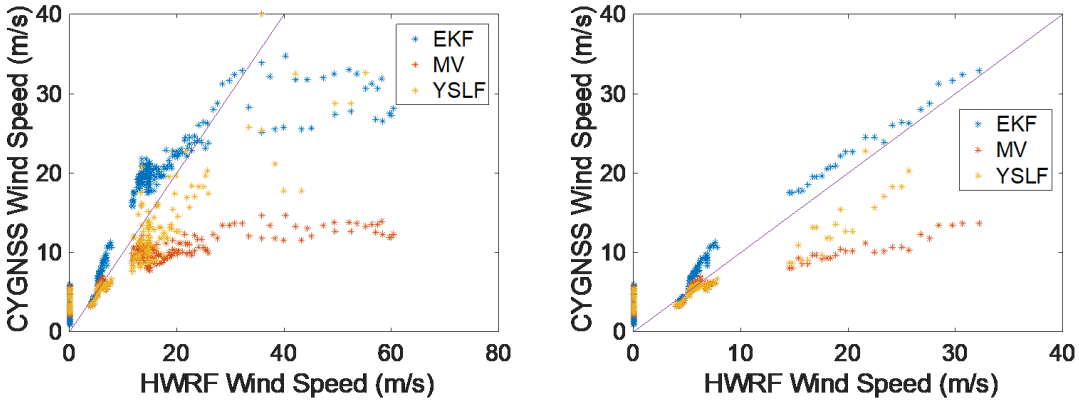

Figure 6.6. Wind speed retrieval comparison between EKF, MV and YSLF (partially promising result).

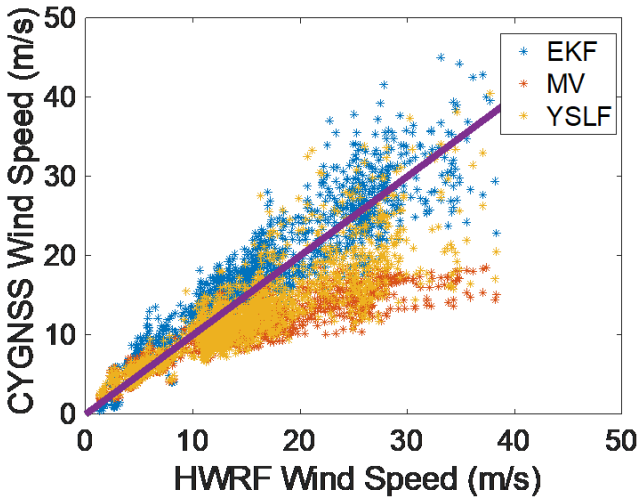

Figure 6.7. Comparison of all the good cases (about 80 percent of the entire data set).

Doppler. Computation of the updated Jacobian matrix in this case would require deriving equations to describe the partial derivatives of the discretized scattering model function with respect to the new state parameters (power, delay and Doppler). This will be incorporated in our future work.

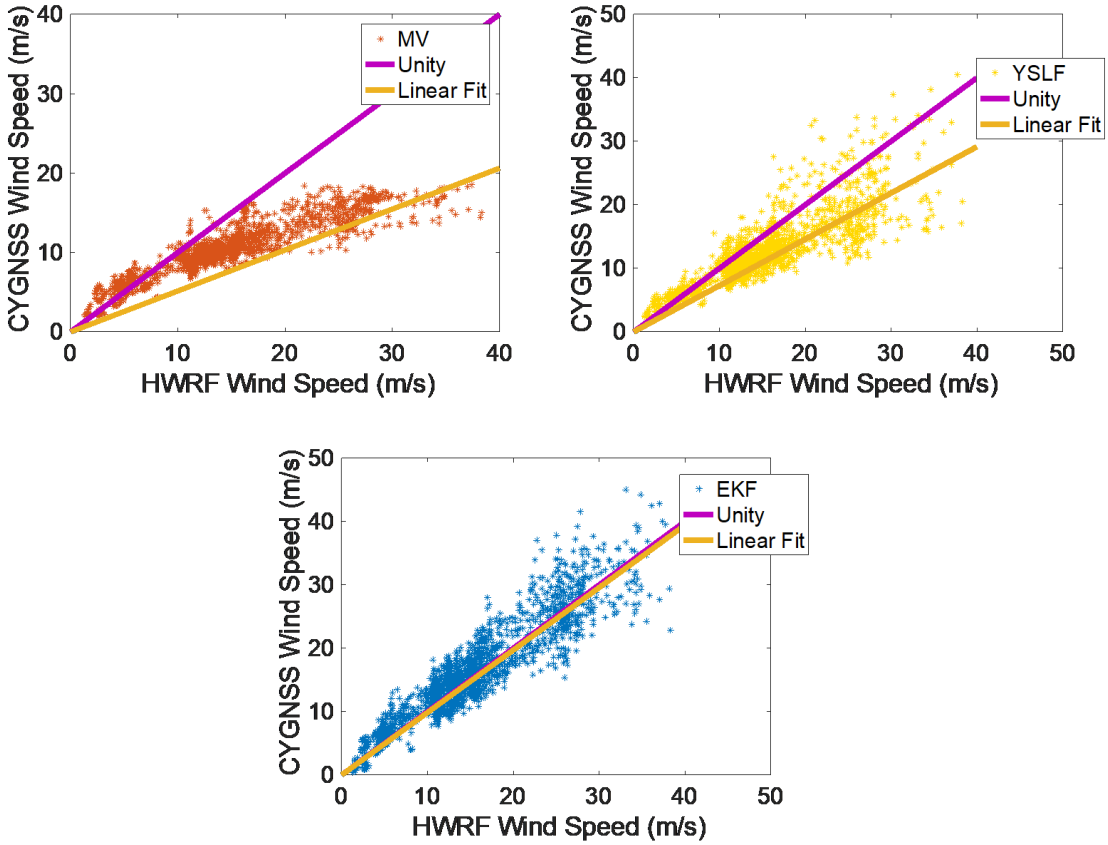

Figure 6.8. Wind speed retrieval comparison between EKF, MV and YSLF (promising results).

6.4.2 HWRF Accuracy

In this work, the HWRF model is used as the ground truth providing references for comparisons of wind speed retrievals. However, as a numerical weather prediction and assimilation model, HWRF also suffers from its own accuracy limitations. In addition, the HWRF model uses ground truth measurements, such as buoys and radars, as input to initialize the wind field. Due to the fact that the US coastal areas have the most abundant in situ measurements, HWRF can achieve the best accuracy for the part of oceans close to these areas. However, CYGNSS data used in this work were mostly collected in winter and spring, which is a period when hurricanes form

mostly in regions far away from the US. This definitely degrades the accuracy of the HWRF model.

On the other hand, the HWRF model produces gridded wind speed with a 3-hour time interval, and three types of telescopic atmospheric domains and associated grid sizes. The parent domain covers an $80^o \times 80^o$ latitude/longitude area with a grid spacing of approximately 27 km, the intermediate nest domain covers $11^o \times 11^o$ with a 9-km grid spacing, and the innermost nest, focusing on the hurricane core, covers $6.5^o \times 7.2^o$ with a 3-km grid spacing. The nests move to follow the storm. Thus, interpolation methods need to be applied in order to obtain match-ups in locations and times between HWRF and CYGNSS wind speed data. In this work, a very simple 2-D linear interpolation method was used to get the wind speed on a specific point on ocean surface from the four closest surrounding grid points. This is basically an interpolation technique commonly seen in image processing. It is expected that better accuracy can be achieved with more sophisticated interpolation techniques that take into account the second and third order derivatives of the data.

6.4.3 Wave-wind relationships

The wave-wind relationship is a challenging topic to address in the ocean reflectometry field. The reflectometry technique directly senses and estimates the ocean surface roughness using scattering models. Wind speed measurements are then indirectly calculated from ocean wave parameters using wind speed retrieval models. All the models were developed either empirically or semi-analytically under certain assumptions or restricted conditions, and thus are incapable of responding accurately to the complexity of real-world scenarios. Firstly, the scattering model currently used for GNSS-R was derived under the KA-GO which assumes strong diffuse scattering typical of very rough surfaces. This equation would be invalid for the case of weak diffuse scattering with coherent reflections in low wind speed conditions. As to wind speed retrievals models, Katzberg's empirical model and Elfouhaily's semi-analytical

ocean wave spectrum model are two models commonly used to convert MSSs to wind speed, but they both have accuracy limitations. The Katzberg model is an empirical and simplified retrieval model which relates MSS to wind speed by a unified function that does not take various ocean wave conditions into account. The semi-analytical Elfouhaily model is based on the assumption that the sea is fully developed with infinite fetch. However, in reality, ocean surface conditions exhibit significant variations that are nearly unpredictable, so this assumption is actually only valid for very limited circumstances. Furthermore, the Elfouhaily model only considers locally generated waves, overlooking waves generated elsewhere that propagate from far away, such as swells. These swells always appear in the low wavenumber region of the ocean wave spectrum, and in some circumstances can not be distinguished and separated from locally generated waves.

Recent development in both ocean wave modeling and scattering modeling have provided new ideas that have the potential to solve some of these problems. In [15] and [16], a new scattering model and bistatic radar function was developed by Voronovich and Zavorotny using the SSA (Small Slope Approximation), which allows the transition from partially coherent scattering to completely non-coherent diffuse scattering to be correctly described. The performance of the revised SSA model in the case of weak scattering was also evaluated using reflected signals collected over the ocean near South Carolina. Results with KA-GO and SSA were compared for low wind speed scenarios. The results showed that the SSA model produced lower wind speed retrievals in low to medium diffuse scattering conditions. In addition, an excess MSS method was proposed which uses WaveWatch III data to estimate the low-frequency swell spectrum so as to remove the effect of swells in ocean surface roughness measurements and wind speed retrievals [48]. It is anticipated that these new approaches will improve accuracy in future work.

6.5 Conclusion

An updated EKF-based wind speed retrieval method was presented for processing actual CYGNSS data. This method highlights the conversion from specular frame-based to Lat/Lon frame-based state vectors. The modified EKF algorithm was first verified using simulated DDMs where Lat/Lon frame-based and specular frame-based approaches were compared and analyzed. Lat/Lon frame-based approach showed a better response to rapid wind speed changes in hurricane centers. Results from actual CYGNSS data processing have demonstrated that, in comparison with observable methods-FDS (Fully Developed Sea) and YSLF (Young Sea Limited Fetch), the EKF inversion algorithm improved the sensitivity and accuracy for high wind retrieval in spaceborne applications. Statistics of wind speed retrievals from 14 selected CYGNSS data tracks showed that the EKF-based method has a mean bias of 0.84 m/s and an RMS error of 3.03 m/s, while the two CYGNSS baseline algorithms have mean biases higher than 2 m/s and RMS errors higher than 4 m/s. The error sources for the EKF were also analyzed and possible solutions were proposed and discussed. Future work in this area may include: (1) develop an improved L-band GMF for CYGNSS wind speed retrieval using wide-band GNSS signals; (2) add state parameters to EKF processing to account for the offsets in DDM power, delay and Doppler; (3) process more hurricane data sets and compare the results with different hurricane models to obtain a thorough evaluation of the performance of the EKF; (4) adjust and achieve an optimal setting of the statistical parameters in the EKF approach, including covariances of process noise, observation errors and initial state errors.

7. SUMMARY

The purpose of this dissertation was to develop and implement new models and algorithms for ocean surface wind speed retrievals using multi-frequency signals of opportunity. First, the history of ocean surface wind retrievals by reflectometry was reviewed as well as the fundamental measurement introduced. Then, the scattering model theory that the research is based on was illustrated, including the fundamental geometry, the bistatic scattering models and the ocean roughness models. The theory showed that the ocean scattering typically consists of both the coherent and non-coherent components and SSA is a more accurate model than KA-GO due to its consideration of both components and its validity for a wide range of wind speed or surface scattering conditions. Then, the techniques and key findings relevant to three major topics were then described.

First, a new geophysical model function was developed to extend the reflectometry technique to S-band communication signals. The cross correlation of the S-band reflected signal with the direct signal was used to generate a power v.s. delay waveform which was then fit to a forward scattering model (KA-GO) to estimate the ocean surface MSS. After generating MSS estimates, data acquired over the land, during aircraft banking, or in the storm eye were removed. Those conditions would degrade the sensitivity of the correlation waveforms to wind variations. Wind speed retrieved using the original Cox and Munk model was compared with the transformed flight-level wind speed which was considered to be the ground truth. A model was then fit to the relationship between the retrieved wind speed and ground truth as a correction to the Cox and Munk model. A linear relationship was found to fit the low wind region best. A logarithm function was applied to fit the high wind region. Last, data from GPS dropsondes were used to validate the correction model. Agreement of the

wind speed measurements between S-band and dropsondes was generally good. This confirmed the developed S-band geophysical model function.

Next, in order to improve the low wind speed retrieval, the SSA model was implemented and evaluated by comparison with the conventional KA-GO model. First, the 2017 Carolina Offshore airborne experiment was introduced where dual-pol reflected signals from L-band GNSS (Global Navigation Satellite System) and S-band SDARS (Satellite Digital Audio Radio Service) transmissions were collected. Then, preliminary MSS estimates from S-band and GNSS data were obtained under the KA-GO model, which were then converted to wind speeds using the empirical model functions. Agreement between wind speeds retrieved from the aircraft, CYGNSS and nearby buoys was generally close. Several problems were identified and possible solutions were tested. In order to improve the low wind speed retrieval, the SSA model was implemented. The simulated BRCS and DDM were found to present different features in comparison with those obtained with conventional KA-GO model. For evaluating the performance of the SSA model, especially in terms of the potential of improving the accuracy of low wind speed retrievals, the data collected in NRL experiments were reprocessed using the SSA-based scattering model and the Elfouhaily ocean wave spectrum model. In comparisons with NOAA buoy ground truth data, the SSA model achieved a better agreement in low wind retrievals than the KA-GO model for both the L- and S-band reflectometry data.

The advert of a spaceborne reflectometry system, represented by the CYGNSS constellation, launched in 2014, presented a new challenge to current wind speed retrieval algorithms designed for application to airborne platforms. In the last section, a new EKF-based multi-look DDM processing method was proposed which inverts the complete DDM to generate estimates of the wind field within a swath defined by the maximum DDM extent. In this method, the EKF was applied by exploiting the large overlap between sequential DDM's, to estimate the wind speed on a uniformly-gridded ocean surface. Simulated retrievals obtained at the specular point using this method met the CYGNSS measurement requirements and performed better than the

baseline algorithms. Applying the method to actual CYGNSS data showed that the EKF inversion algorithm improved the performance of the retrievals over the entire wind speed analysis range. For statistical evaluation, fourteen selected CYGNSS data tracks were processed covering wind speeds up to 40 m/s. For about 80% of the data set categorized as good cases, EKF achieved a mean bias of 0.84 m/s and RMSE of 3.03 m/s, while the two CYGNSS baseline algorithms obtained mean biases higher than 2 m/s and RMSEs higher than 4 m/s.

7.1 Future Work

The complexity of ocean wind remote sensing using SoOps makes it a field of research with many possible avenues of investigation. Many additional issues and approaches need to be addressed and studied to further improve technology development in this area. The remainder of this chapter briefly describes some specific potential research projects.

(1) Explore more possible signals of opportunity: wide-band L5 and E5 wind speed retrieval

Previous studies of ocean wind remote sensing with GNSS-R have been focused on the L1 GPS frequency band. However, it is expected that more accurate measurements can be obtained by using similar methods with wider bandwidth signals, such as the GPS L5 or Galileo E5 signals. A prototype data collection system was developed which could handle the necessary data sampling speeds for the L5 and E5 signals. This system uses a USRP X300 device configured to sample at 100 MHz. For future field experiments, data will be obtained by mounting the prototype data collection system on the National Oceanic and Atmospheric Administration (NOAA) Hurricane Hunter aircraft during the hurricane season, and wind speed retrieval will be performed by analyzing the DDMs generated by the receiver. A new L-band GMF will be developed based on the retrievals.

(2) Advancement and evaluation of the EKF-based wind speed retrieval method

The current version of EKF method includes only the gridded wind speed field as the unknown state parameters to be estimated. Other possible uncertainties such as the power and delay Doppler offsets should also be taken into account in future versions. We will also focus on parallel processing of the EKF method to optimize the computation efficiency. The current slower single process approach precludes its use as an operational retrieval method for user-oriented data release. Another possible future is to apply the general idea of EKF to the recently proposed GIG (Gamma-Inverse-Gamma) filter which was developed based on the assumptions of Gamma or Inverse Gamma probabilities instead of Gaussian statistics and would theoretically be better suited to retrieval of ocean surface wind than the Kalman Filter. As to evaluations, instead of data from selected tracks, a larger volume of CYGNSS datasets with various conditions will need to be processed to further verify the EKF method. Results will also be compared with different wind models such as GDAS and ECMWF in addition to HWRF, to allow a more thorough validation to be performed.

(3) S-band cutoff number of the Elfouhaily model

The cutoff number of the Elfouhaily model for L-band GPS signals has already been investigated through substantial theoretical and experimental work. The currently used model describes the value of the cutoff number as a function of frequency and elevation angle. However, its validity for frequencies other than L-band has not been experimentally demonstrated yet. We look to evaluate the model by analyzing actual MSS estimates from S-band signals, with the possibility of proposing a new S-band empirical cutoff number model, or developing an improved version of the general model combining both the L-band and S-band results.

(4) Machine learning

Machine learning methods could be explored for ocean wind retrieval. One potential application would be to design and train a neural network connecting the CYGNSS DDM and the ground truth wind speed to serve as the direct retrieval model in replacement of the current fitted GMF. Ancillary information such as elevation angle and delay and Doppler bin will also be needed as elements of the input CYGNSS data for training and applying the neural network.

A. S-BAND REFLECTOMETRY DATA PROCESSING

A.1 Background

The fundamental principle of sensing the surface roughness using reflectometry is based upon fitting a scattering model to the observed DDM. The DDM is generated through the cross-correlation of the baseband transmitted signal $s(t)$, with the reflected signal $s_r(t)$, at delays τ , and Doppler shifts, f. For GPS signals, the local signal can be generated with the PRN code. However, the data transmitted by a communication satellite are not a priori known, so in this case, the direct signal is often used to perform the correlation in replacement of the local copy.

A.2 Satellite Digital Audio Radio Service (SDARS) signal Structure

The SDARS system is a satellite-based digital broadcasting system. The two currently active geostationary satellites of the system are: "XM3" (Rhythm) located at 85^oW and "XM4" (Blues) located at 115^oW. The spectrum of SDARS spans between 2332.5 and 2345.0 MHz (S-band). Each SDARS satellite transmits two left hand circular polarization (LHCP) signals with quadrature phase shift keying (QPSK) modulation. Each signal transmission channel has a bandwidth of 1.886 MHz and a symbol rate of 1.64 Msps.

A.2.1 SDARS Received Signal Model

Assuming that the SDARS transmits random binary bits with a uniform distribution, the direct signal can be modeled as

$$S_d(t) = As(t)e^{-j2\pi f_c t} + \eta(t) \tag{A.1}$$

where A is the amplitude, f_c is the carrier frequency, $\eta(t)$ is Gaussian noise,and $s(t)$ is the baseband signal.

$$s(t) = \sum_{k=-\infty}^{\infty} Ae^{(\frac{\pi}{4}j+\frac{\pi}{2}a_k j)} p(\frac{t-kT_s}{T_s}) \tag{A.2}$$

where a_k represents the data in QPSK modulation (a_k = 0, 1, 2, 3), $p(\cdot)$ is a unit pulse and T_s is the symbol period (0.6098 s).

A.2.2 Self-Ambiguity Function (SAF): Theoretical Model

The theoretical model of the SAF for a coherent integration time T_i is expressed as

$$|\chi(\tau, f)|^2 = |\frac{1}{T_i}\int_0^{Ti} s(t)s^*(t-\tau)e^{-j2\pi ft}dt|^2 \tag{A.3}$$

which is approximated by

$$|\chi(\tau, f)|^2 \approx |\Lambda(\tau)|^2|S(f)|^2 \tag{A.4}$$

where $\Lambda(\tau)$ is the autocorrelation function and $S(f)$ is a sinc function

$$|S(f)|^2 = |sinc(fT_i)|^2 \tag{A.5}$$

A.3 Scattering Model

A scattering model based on KA-GO for the correlation waveform was developed for reflectometry [1], which is expressed as

$$< |Y_M(\tau, f_c; P_{\vec{v}})| >= \frac{T_i^2}{4\pi}\int\int \frac{D^2(\vec{\rho})}{R_0^2(\vec{\rho})R^2(\vec{\rho})}\frac{\pi|\Re|^2 q^4(\vec{\rho})}{q_z^4(\vec{\rho})}P_{\vec{v}}(-\frac{\vec{q}_\perp}{q_z})|\chi[\delta\tau(\vec{\rho}), \delta f(\vec{\rho})]|^2 d^2\vec{\rho} \tag{A.6}$$

where, $\chi[\delta\tau(\vec{\rho}), \delta f(\vec{\rho})]$is the SAF, and $D(\vec{\rho})$ is the antenna gain pattern. $R_0(\vec{\rho})$ is the distance to the transmitter, and $R(\rho)$ is the distance to the receiver. $\Re$ is the Fresnel reflection coefficient. $\vec{q}_\perp$ and q_z are the horizontal and orthogonal component of the scattering vector, respectively, and that is, $\vec{q} = (\vec{q}_\perp, q_z) = (q_x, q_y, q_z)$. $P_{\vec{v}}$ is the

Gaussian slope PDF related to the surface wind speed. $\vec{\rho}$ is a 2-D surface coordinate on the ocean surface. For this work, $P_{\vec{v}}$ is assumed to be a bivariate Gaussian function with two underdetermined parameters upwind MSS σ_u^2 and crosswind MSS σ_c^2 that are related to the ocean surface roughness.

$$P_{\vec{v}}(-\frac{\vec{q}_\perp}{q_z}) = \frac{e^{-\frac{1}{2}(\xi^2+\eta^2)}}{2\pi\sigma_u^2\sigma_c^2} \tag{A.7}$$

where $\xi = \frac{q_x/q_z}{\sigma_u}$ and $\eta = \frac{q_y/q_z}{\sigma_c}$. Here we assume that σ_u^2 and σ_c^2 are constrained by the relationship defined by the adjusted Cox and Munk model, so we obtain

$$\sigma_c^2 = 0.6076 \cdot \sigma_u^2 + 0.00135 \tag{A.8}$$

A.4 Signal Processing Procedure

The signal processing procedure is basically composed of 5 parts: raw data collection, filtering, cross-correlation, curve fitting and wind speed retrieval.

A.4.1 Raw Data Collection

In the NOAA hurricane mission, an S-band signal recorder was installed in the NOAA P-3 "Hurricane Hunter" aircraft to collect XM radio signals during the 2014 hurricane season which included 5 hurricanes: Arthur, Bertha, Cristobal, Dolly and Edouard. Direct and reflected XM signals were received by S-band RHCP and LHCP antennas, respectively. Amplified received RF signals were down-converted and digitalized by a USRP, and the data were saved to an external hard drive, with the whole process controlled by a single-board computer. a center frequency of 2342.205 MHz and a sampling frequency f_s of 4 MHz were used.

A.4.2 Filtering

The S-band recorder described above samples the XM radio signal and stores the raw data in the hard drive. The center frequency is set to the middle of the XM3 and

XM4 spectra, and the 4-MHz bandwidth spans the two XM components. Figure A.1 plots the spectrum of the raw data which clearly shows XM3 and XM4 located at each side. In order to split the XM3 and XM4 signals apart and process them separately, the collected data were passed through two 2-MHz digital bandpass filters. Figure A.2 shows the frequency response of the applied 2-MHz high-pass filter and the spectrum of the isolated XM3 signal.

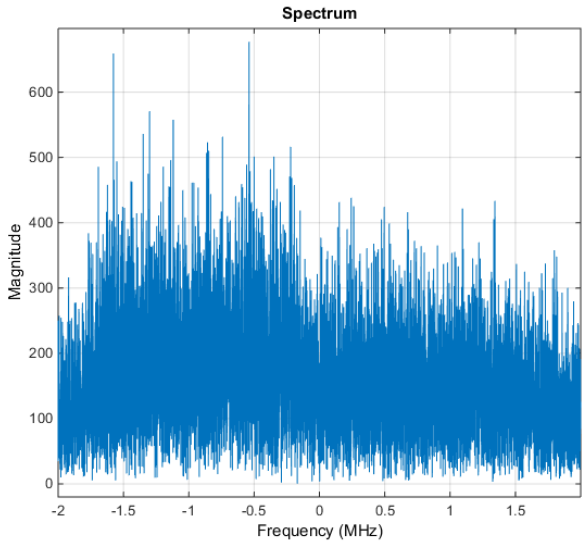

Figure A.1. The spectrum of collected raw data.

A.4.3 Cross-correlation

The next step involves correlation between the direct and reflect signals, which generates the DDM. Correlation takes the following form:

$$Y(\tau, f) = \frac{1}{T_i} \int_{Ti} S_d(t^{'}) S_r^*(t^{'} - \tau) e^{-j2\pi f t^{'}} dt^{'} \tag{A.9}$$

where $S_d(t)$ is the direct signal and $S_r(t)$ is the reflected signal. T_i is the integration time which is set to be 1 ms. τ is the time delay and f is the Doppler shift. For a static satellite and a typical aircraft velocity, the Doppler frequency variations over the glistening zone is negligible. As a result, a simplified 1-D correlation waveform

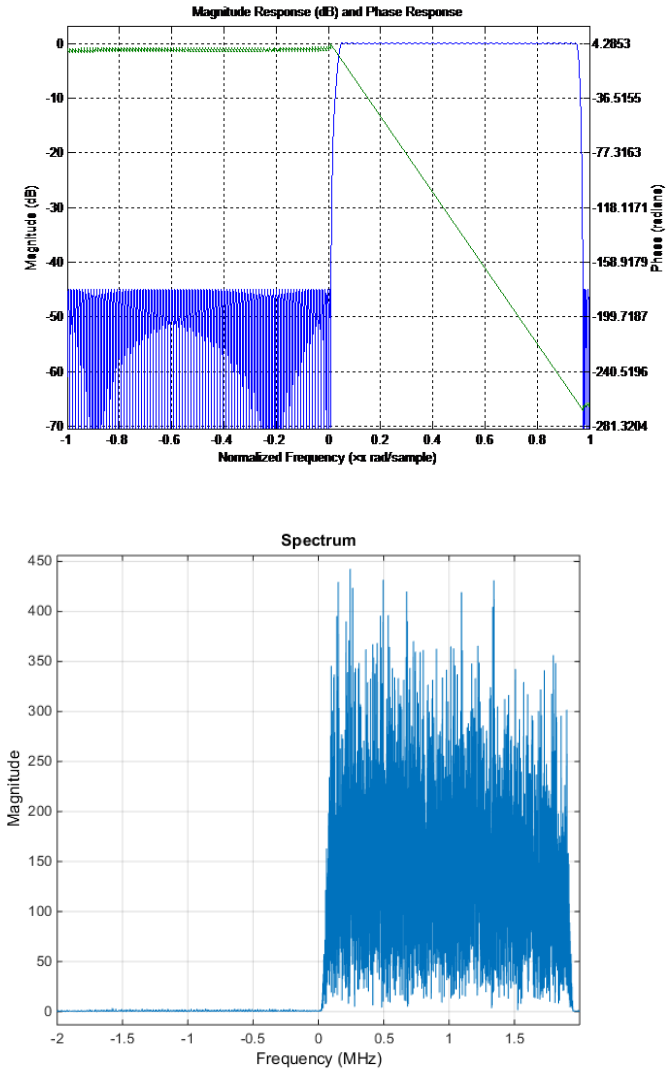

Figure A.2. Frequency response of applied 2MHz-bandwidth high-pass filter and the spectrum of isolated XM3 signal.

(delay map) can be applied which only reflects the correlation properties along the delay axis.

$$Y(\tau, f) = \frac{1}{T_i} \int_T i S_d(t^{'}) S_r^*(t^{'} - \tau) dt^{'} \tag{A.10}$$

Figure A.4.3 shows the correlation waveform for XM3 and XM4 signals collected simultaneously. The different delays of the two correlation waveforms are the results of different satellite-receiver geometries. One way to obtain the time delay is to

estimate it from correlation waveforms through the curve fitting process. We refer to this type of delay estimates as the experimental delay. Alternatively, the time delay can also be calculated from the true geometry between satellite and receiver, which we denote as the theoretical delay. The delay bias is defined as the difference between the two types of delays. Figure A.4.3 plots the theoretical delay and delay bias for the XM3 data. It can be observed that while the theoretical delay can reach up to 25 ms, the delay bias is always very close to zero. This confirms the consistency of our measured delay and the theoretical delay.

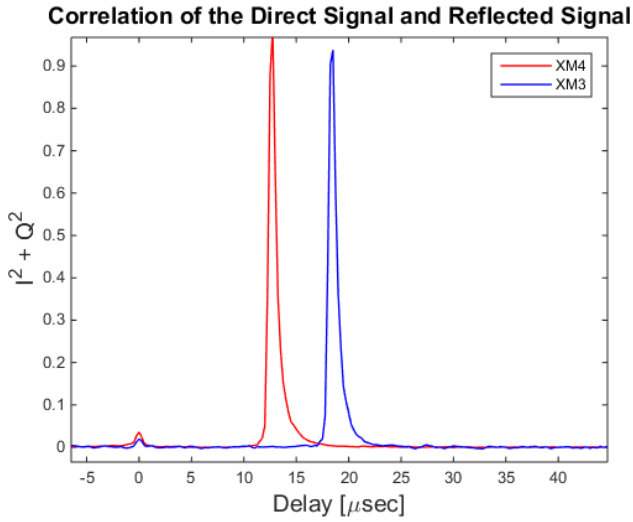

Figure A.3. Correlation waveforms of XM3 and XM4 signals.

The correlation waveforms obtained with a coherent integration time of 0.001 s were then processed with an incoherent integration time interval of 0.1 s. The noise floor, computed by averaging the correlation power outside the correlation peak, was subtracted from the complete waveform. Then, the waveforms were moved along the delay axis by the theoretical delay τ_t, so that the peak was centered around zero.

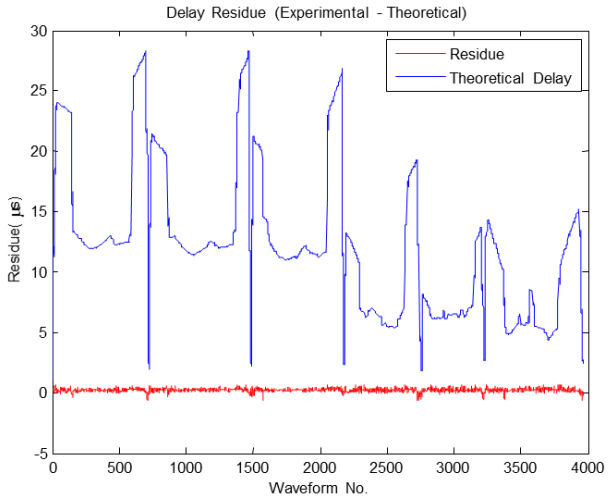

Figure A.4. Delay and delay residue of XM3 signal.

A.4.4 Curve Fitting

The surface roughness was then estimated by fitting the scattering model to the observed correlation waveform. The scattering model relates the waveform shape to the sea surface roughness parameterized as the MSS of the ocean surface. The model used here is the widely accepted geometric optics limit of the Kirchhoff approximation model (KA-GO), which is only applicable to strong diffuse scattering and high wind conditions.

The curve fitting process works by adjusting the MSS to minimize the cost function. We followed the approach of nonlinear least square estimation, with a three-element parameter vector consisting of upwind MSS σ_u^2, delay offset τ_0 and scale factor S. τ_0 accounts for small delay uncertainties, and S removes signal power variations. As noted above, we assume the upwind and crosswind MSS have the relationship defined by the Cox and Munk model, so crosswind MSS σ_c^2 can be easily derived from σ_u^2 through the formula $\sigma_c^2 = 0.6076 \cdot \sigma_u^2 + 0.00135$. Thus it is sufficient to include only one of the two MSSs in the parameter vector for estimation purposes. Interpolated wind direction data from HWRF, converted to the scattering plane, was incorporated

to transform the slopes to upwind and crosswind directions. The Doppler effect and antenna gain were considered uniform over the limited glistening zone.

Every 50 such waveforms obtained were processed as one batch to produce one MSS estimate, assuming the ocean surface roughness did not vary much during this period. Figure A.5 shows results of curve fitting and MSS estimation with data collected under different wind speed conditions. The MSS increases from 0.00292 to 0.0272 representing increasing ocean roughness and wind speed. Correspondingly, the waveforms show a progressively wider trailing edge with larger MSS.

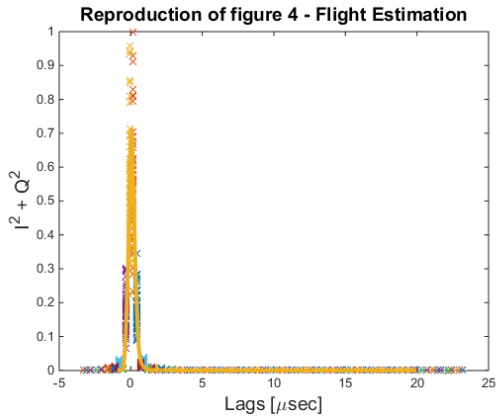

(a) MSS=0.0028

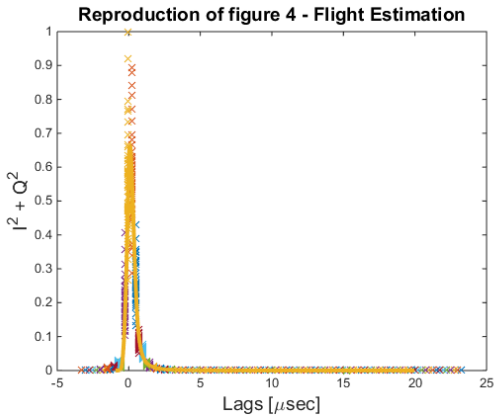

(b) MSS=0.0061

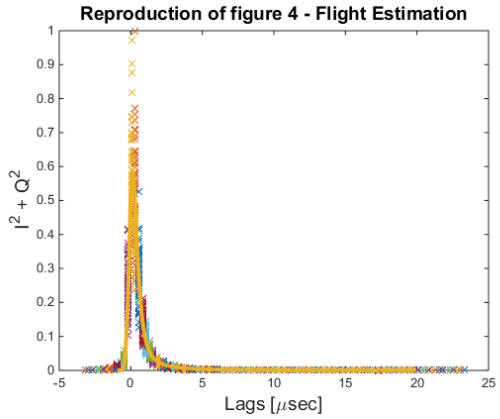

(c) MSS=0.0115

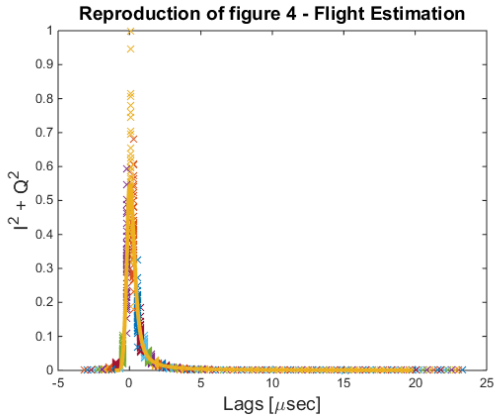

(d) MSS=0.0131

Figure A.5. Curve fitting and MSS estimation.

B. DERIVATION OF THE BISTATIC RADAR EQUATION

This chapter summarizes the derivation of the bistatic radar equation presented in [16].

The field radiated by a point source with horizontal and vertical coordinates, $\vec{r_0}$ and $z_0 > 0$, respectively, can be expressed as

$$\frac{e^{i(\omega/c)}R}{R} = \frac{i}{2\pi}\int \frac{d\vec{k}}{q_k} e^{i\vec{k}(\vec{r}-\vec{r_0})+iq_k(z_0-z)} \tag{B.1}$$

where

$$R = \sqrt{(\vec{r}-\vec{r_0})^2 + (z-z_0)^2} \tag{B.2}$$

and

$$q_k = \sqrt{\omega^2/c^2 - k^2} \tag{B.3}$$

$\vec{k}$ and q_k are horizaontal and vertical component of the wave vector, respectively.

Then, the incident field Ψ_{in} incident can be expressed as:

$$\Psi_{in}(\vec{r},z) = \frac{i}{2\pi}\sqrt{P_{tr}}\int d\vec{k_0} D_{tr}(\vec{k_0}) \frac{1}{q_{k_0}^{1/2}} e^{-i\vec{k_0}\vec{r_0}+iq_{k_0}z_0} \times \frac{1}{q_{k_0}^{1/2}} e^{i\vec{k_0}\vec{r}-iq_{k_0}z} \tag{B.4}$$

where P_{tr} is the transmission power of the source, $D_{tr}(\vec{k})$ is the antenna gain, and the integration variable $\vec{k}$ is replaced by $\vec{k_0}$. The last factor in (B.4) represents a single incident plane wave. The scattered field produced by such a wave can be expressed in terms of scattering amplitude $S(\vec{k},\vec{k_0})$. Then, using a superposition principle, the scattered field produced by Ψ_{in} can be expressed as

$$\Psi_{sc}(\vec{r},z) = \frac{i}{2\pi}\sqrt{P_{tr}}\int d\vec{k_0} D_{tr}(\vec{k_0}) \frac{1}{q_{k_0}^{1/2}} e^{-i\vec{k_0}\vec{r_0}+iq_{k_0}z_0} \times \int d\vec{k} D_{rec}(\vec{k}) \frac{1}{q_k^{1/2}} e^{i\vec{k}\vec{r}+iq_{k_0}z} S(\vec{k},\vec{k_0}) \tag{B.5}$$

where $D_{rec}(\vec{k})$ is the receiver antenna directivity.

Assume a narrow-band signal is transmitted, which has a center frequency ω_0 and envelope $a(t)$

$$a(t)e^{-i\omega_0 t} = \int \hat{a}(\omega)e^{-i\omega t}d\omega \tag{B.6}$$

where $\hat{a}(\omega)$ is the signal spectrum that is concentrated in the vicinity of ω_0. Note that both q_{k0} and q_k are the functions of the frequency. If the motion of the transmitter can be represented by a substitution

$$\vec{r_0} \to \vec{r_0} + \vec{u}^{(0)}t, \quad z_0 \to z_0 + u_z^{(0)}t \tag{B.7}$$

in (B.5), and, similarly, for $(\vec{r}, z)$. $\vec{r_0}$, $\vec{r}$, z_0, and z represent the coordinates of the transmitter and the receiver at $t = 0$; $\vec{u}^{(0)}$ and $u_z^{(0)}$ stand for the horizontal and vertical components of the transmitter velocity. $\vec{u}$ and u_z stand for the horizontal and vertical components of the receiver velocity. As a result, the envelope of the received field $\tilde{\Psi_{sc}}$ can be expressed as a function of time:

$$\begin{aligned}\widetilde{\Psi}_{sc} &= \Psi_{sc}(t)e^{-i\omega_0 t} \\ &= \frac{i\sqrt{P_{tr}}}{2\pi}\int \hat{a}(\omega)d\omega \int \frac{d\vec{k_0}}{q_{k_0}^{1/2}} D_{tr}(\vec{k_0}) \int \frac{d\vec{k}}{q_k^{1/2}} D_{rec}(\vec{k_0}) \\ &\times S(\vec{k}, \vec{k_0})e^{i\vec{k}\vec{r} - i\vec{k_0}\vec{r_0} + iq_k z + iq_{k_0} z_0 - i\Omega t}\end{aligned} \tag{B.8}$$

where

$$\Omega = \omega - \omega_0 + \vec{k_0}\vec{u_0} - q_{k_0}u_z^{(0)} - \vec{k}\vec{u} - q_k u_z \tag{B.9}$$

Then, (B.8) needs to be integrated over frequency ω. For this purpose, the frequency dependence in the exponent is represented as a linear function of ω by rescaling $\vec{k}$ and $\vec{k}_0$ by ω. D_{tr}, D_{rec}, and S vary much more slowly with respect to ω as compared to the phase term. Therefore, ω can be simply set as ω_0 in those functions. With (B.6), we can then calculate the integration and obtain

$$\begin{aligned}\widetilde{\Psi}_{sc}(t) =& \frac{i\sqrt{P_{tr}}}{2\pi}\int D_{tr}(\vec{k})D_{rec}(\vec{k}_0)S(\vec{k}, \vec{k}_0) \\ &\times exp[i\omega_0\tau_0(\vec{k}, \vec{k}_0) + i\Delta\omega(\vec{k}, \vec{k}_0)t] \\ &\times a[(1 - \Delta\omega(\vec{k}, \vec{k}_0)/\omega_0)t - \tau_0(\vec{k}, \vec{k}_0)]\frac{d\vec{k}\vec{k}_0}{\sqrt{q_k q_{k_0}}}\end{aligned} \tag{B.10}$$

where

$$\Delta\omega(\vec{k},\vec{k}_0) = \vec{k}\vec{u} + q_k u_z - \vec{k}_0\vec{u}^{(0)} + q_{k_0}u_z^{(0)}$$
$$\tau_0(\vec{k},\vec{k}_0) = \frac{\vec{k}\vec{r} + q_k z - \vec{k}_0\vec{r}_0 + q_{k_0}z_0}{\omega_0} \tag{B.11}$$

and q_k and q_{k_0} are evaluated at $\omega = \omega_0$.

The DDM is a cross correlation between the envelops of the received signal and the transmitted signal

$$Y(t,\tau,\omega_D) = \frac{1}{T_i}\int_0^{T_i} \tilde{\Psi}_{sc}(t+t')a^*(t+t'-\tau)e^{i\omega_D t'}dt' \tag{B.12}$$

where τ is time delay, ω_D is frequency offset, T_i is a coherent integration time and t is running time.

Substituting (B.10) into (B.12), we can obtain

$$\begin{aligned} Y(t,\tau,\omega_D) =& \frac{i\sqrt{P_{tr}}}{2\pi}e^{-i\omega_D t - i\delta\omega\tau}\int\int D_{tr}(\vec{k}_0)D_{rec}(\vec{k}) \\ &\times S(\vec{k},\vec{k}_0)exp[i\omega_0\tau_0(\vec{k},\vec{k}_0)] \\ &\times \chi(t-\tau,\delta\tau,\delta\omega,\beta)\frac{d\vec{k}_0 d\vec{k}}{\sqrt{q_k q_{k_0}}} \end{aligned} \tag{B.13}$$

where

$$\delta\tau = \beta\tau - \tau_0 \tag{B.14}$$
$$\delta\omega = -\Delta\omega - \omega_D \tag{B.15}$$
$$\beta = 1 - \frac{\Delta\omega}{\omega_0} \tag{B.16}$$

β considers the Doppler effect with respect to the envelope of the transmitted signal. $\delta\tau$, $\delta\omega$, and β also depend on $\vec{k}$ and $\vec{k}_0$ here. $\chi(\delta\tau,\delta\omega_*,\beta_*)$ is the Woodward ambiguity function (WAF)

$$\chi(t,\delta\tau,\delta\omega_*,\beta_*) = \frac{1}{T_i}\int_t^{T_i+t} a(\beta_* t' + \delta\tau)a^*(t')e^{-i\delta\omega_* t'}dt' \tag{B.17}$$

Now, we assume that the roughness is statistically homogeneous over the horizontal plane. Then, we average $|Y(\tau,\omega_D)|^2$ w.r.t. the statistical roughness ensemble. For

this purpose, we redefine integration variables $\vec{k}_0$ and k as $\vec{\kappa}_0^{'}$ and $\vec{\kappa}^{'}$, and $\vec{\kappa}_0^{''}$ and $\vec{\kappa}^{''}$, respectively, and add new variables $\vec{k}_0$, $\vec{k}$, $\vec{b}_0$, and $\vec{b}$. Their relationships are shown as follows:

$$\vec{\kappa}_0^{'} = \vec{k}_0 - \frac{\vec{b}_0}{2}, \quad \vec{\kappa}_0^{''} = \vec{k}_0 + \frac{\vec{b}_0}{2}, \quad \vec{\kappa}_0^{'} = \vec{k} - \frac{\vec{b}}{2}, \quad \vec{\kappa}^{''} = \vec{k}_0 + \frac{\vec{b}}{2}. \tag{B.18}$$

In (B.13), the statistical information of roughness is included in scattering amplitude S. We can obtain the following correlation expression based on the assumed statistical spatial homogeneity of roughness:

$$\overline{S(\vec{k} - \frac{\vec{b}}{2}) S^*(\vec{k} + \frac{\vec{b}}{2}, \vec{k}_0 + \frac{\vec{b}_0}{2})} = E(\vec{k}, \vec{k}_0; \vec{b}) \delta(\vec{b} - \vec{b}_0) \tag{B.19}$$

As χ varies slowly with respect to changes in $\vec{k}$ and $\vec{k}_0$, we can expand the exponent part into powers of $\vec{b}$ and retain the lowest order $O(\vec{b})$ terms

$$\begin{aligned} \vec{\kappa}^{'}\vec{r} - \vec{\kappa}_0^{'}\vec{r}_0 + q_{\kappa_0^{'}} z_0 + q_{\kappa^{'}} z - (\vec{\kappa}^{''}\vec{r}_0 + q_{k_0^{''}} z_0 + q_{k^{''}} z) \\ \approx (\vec{r}_0 - \vec{r} + \frac{\vec{k} z}{q_k} + \frac{\vec{k}_0 z_0}{q_{k_0}}) \vec{b} \end{aligned} \tag{B.20}$$

This approximation is only valid when the function χ has smooth variations with respect to its parameters.

With approximation (B.20), the integration over $\vec{b}$ produces a δ-function which is shown as follows:

$$\begin{aligned} \overline{|Y(\tau, \omega_D)|^2} = & P_{tr} \int\int |D_{tr}(\vec{k}_0) D_{rec}(\vec{k})|^2 E(\vec{k}, \vec{k}_0; 0) \\ & \times \langle |\chi(\delta\tau, \delta\omega, \beta)|^2 \rangle \delta(\vec{r}_0 - \vec{r} + \frac{\vec{k} z}{q_k} + \frac{\vec{k}_0 z_0}{q_{k_0}}) \\ & \times \frac{d\vec{k}_0 d\vec{k}}{q_{k_0} q_k} \end{aligned} \tag{B.21}$$

E in (B.21) contains both coherent and noncoherent components

$$E(\vec{k}, \vec{k}_0; 0) = |\overline{V}_{\vec{k}}|^2 \delta(\vec{k} - \vec{k}_0) + \frac{1}{4\pi} \frac{\sigma_0(\vec{k}, \vec{k}_0)}{q_k q_{k_0}} \tag{B.22}$$

where $\overline{V}_{\vec{k}}$ is an average reflection coefficient and $\sigma_0(\vec{k}, \vec{k}_0)$ is a standard BRCS per unit area. $\overline{V}_{\vec{k}}$ is related to the first statistical moment of the scattering amplitude

$$\overline{S(\vec{k}, \vec{k}_0)} = \vec{V}_{\vec{k}} \, \omega(\vec{k} - \vec{k}_0) \tag{B.23}$$

After substituting (B.22) into (B.21), we can obtain

$$\overline{|Y(\tau,\omega_D)|^2} = \overline{|Y(\tau,\omega_D)|_c^2} + \overline{|Y(\tau,\omega_D)|_{nc}^2} \tag{B.24}$$

where the expressions of the coherent and noncoherent components are expressed as:

$$\begin{aligned}\overline{|Y(\tau,\omega_D)|_c^2} =& P_{tr}\int |D_{tr}(\vec{k}_0)D_{rec}(\vec{k})|^2\langle|\chi(\delta\tau,\delta\omega,\beta)|^2\rangle \\ &\times |\bar{V}_{\vec{k}}|^2\delta(\vec{r}_0-\vec{r}+\frac{\vec{k}}{q_k}(z+z_0))\frac{d\vec{k}}{q_k^2}\end{aligned} \tag{B.25}$$

where $\sigma\tau$, $\sigma\omega$, and β are calculated at $\vec{k}=\vec{k}_0$, and

$$\begin{aligned}\overline{|Y(\tau,\omega_D)|_{nc}^2} =& P_{tr}\int\int |D_{tr}(\vec{k}_0)D_{rec}(\vec{k})|^2\langle|\chi(\delta\tau,\delta\omega,\beta)|^2\rangle \\ &\times \sigma_0(\vec{k},\vec{k_0})\delta(\vec{r}_0-\vec{r}+\frac{\vec{k}z}{q_k}+\frac{\vec{k}_0 z_0}{q_{k_0}})\frac{d\vec{k}_0 d\vec{k}}{q_{k_0}^2 q_k^2}\end{aligned} \tag{B.26}$$

After derivation, the coherent component is finally expressed as

$$\begin{aligned}\overline{|Y(\tau,\omega_D)|_c^2} =& P_{tr}|D_{tr}(\vec{n}_*,\omega_0)D_{rec}(\vec{m}_*,\omega_0)| \\ &\times \langle|\chi(\delta\tau,\delta w_*,\beta_*)|^2\rangle\frac{|\bar{V}(\vec{n}_{*\perp},\omega_0)|^2}{R_*^2}\end{aligned} \tag{B.27}$$

where

$$\delta\tau = \beta_*\tau - \frac{\omega_0}{c^2}\frac{z+z_0}{q_k} = \beta_*\tau - \frac{R_*}{c} \tag{B.28}$$

$$\Delta\omega_* = \frac{\omega_0}{c}\frac{(\vec{r}-\vec{r}_0)(\vec{u}^{(0)}-\vec{u})-(z+z_0)(u_z^{(0)}+u_z)}{R_*} \tag{B.29}$$

$$\delta\omega_* = \Delta\omega_* - \omega_D \tag{B.30}$$

$$\beta_* = 1-\frac{\Delta\omega_*}{\omega_0} \tag{B.31}$$

The subscript (*) means the corresponding parameters are related to the coherent component. ω_0 is the center frequency of the transmitted signal. P_{tr} is the transmission power. $(\vec{r}_0, z_0)$ and $(\vec{r}, z)$ are the horizontal and vertical coordinates of the transmitter and the receiver, respectively. D_{tr} and D_{rec} are, the transmitter and receiver antenna gain patterns, respectively. R is the distance between the transmitter and the specular image of the receiver:

$$R_* = \sqrt{(\vec{r}-\vec{r}_0)^2+(z+z_0)^2} \tag{B.32}$$

$\vec{m}_*$ is the unit vector pointing from the transmitter to the specular image of the receiver:

$$\vec{m}_* = (\vec{m}_{*\perp}, m_{*z}) = \frac{1}{R_*}(\vec{r} - \vec{r}_0, -z - z_0) \tag{B.33}$$

$\vec{n}_*$ is the unit vector pointing from the transmitter to the specular image of the receiver:

$$\vec{n}_* = (\vec{n}_{*\perp}, n_{*z}) = \frac{1}{R_*}(\vec{r} - \vec{r}_0, z + z_0) \tag{B.34}$$

$\vec{U}_0 = (\vec{u}^0, u_z^0)$ and $\vec{U} = (\vec{u}, u_z)$ are the velocity vectors of the transmitter and the receiver. Assuming roughness has a Gaussian statistics, $|\bar{V}(\vec{n}_{*\perp}, \omega_0)|^2$ can be expressed as

$$|\bar{V}(\vec{n}_{*\perp}, \omega_0)|^2 = exp(-4R_a^2)|V_F(\vec{n}_{*\perp}, \omega_0)|^2 \tag{B.35}$$

where V_F is the Fresnel reflection coefficient and

$$R_a = \frac{\omega_0}{c} n_{*z} \langle h^2 \rangle^{1/2} \tag{B.36}$$

is a Rayleigh roughness parameter.

The noncoherent component is expressed as

$$\begin{aligned} \overline{|Y(\tau, \omega_D)|^2_{nc}} = & \frac{P_{tr}}{4\pi} \int\int \frac{|D_{tr}(\vec{m}_\perp, \omega_0) D_{rec}(\vec{n}_\perp, \omega_0)|}{R_0^2 R^2} \\ & \times \langle |\chi(\delta\tau, \delta w, \beta)|^2 \rangle \sigma_0(\vec{n}_\perp, \vec{m}_\perp; \omega_0) d\vec{\rho} \end{aligned} \tag{B.37}$$

where

$$\delta\tau = \beta\tau - \frac{R_0 + R}{c} \tag{B.38}$$

$$\Delta\omega = \frac{\omega_0}{c} \frac{(\vec{\rho} - \vec{r}_0)\vec{u}^{(0)} - z_0 u_z^{(0)}}{R_0} - \frac{\omega_0}{c} \frac{(\vec{r} - \vec{\rho})\vec{u} + z u_z}{R} \tag{B.39}$$

$$\delta\omega = \Delta\omega - \omega_D \tag{B.40}$$

$$\beta = 1 - \frac{\Delta\omega}{\omega_0} \tag{B.41}$$

Here, $\vec{\rho}$ represents the position of a scattering element on the surface; $\vec{m}$ is the vector pointing from the transmitter to the scattering element on the surface and $\vec{n}$ is the vector from the scattering element on the surface to the receiver:

$$\vec{m} = (\vec{m}_\perp, m_z) = \frac{1}{R_0}(\vec{\rho} - \vec{r}_0, -z_0) \tag{B.42}$$

$$\vec{n} = (\vec{n}_\perp, n_z) = \frac{1}{R}(\vec{r} - \vec{\rho}, z) \tag{B.43}$$

R_0 is the distance between the scattering element and the transmitter, and R is the distance between the scattering element and the receiver:

$$R_0 = \sqrt{(\vec{\rho} - \vec{r}_0)^2 + z_0^2} \tag{B.44}$$

$$R = \sqrt{(\vec{\rho} - \vec{r})^2 + z^2} \tag{B.45}$$

C. DERIVATION OF THE EKF-BASED MULTI-LOOK DDM PROCESSING METHOD

This chapter summarizes the derivation of the EKF-based multi-look DDM processing method presented in [17].

C.1 Problem statement

The DDM is the fundamental measurement in GNSS reflectometry, which is generated by the cross-correlation between a local replica of the baseband transmitted signal, $u_L(t)$, and the reflected GNSS signal, $u(t)$, shifted to a Doppler frequency, f, with an integration time, T_I.

$$X(\tau, f, t) = \frac{1}{T_I} \int_{t-T_I}^{t} u(\gamma) u_L^*(\gamma + \tau) e^{-2\pi f \gamma j} d\gamma \tag{C.1}$$

Usually, we can assume a rough ocean surface which will result in a uniformly distributed phase of $X(\tau, f, t)$. Often, M power-DDMs are incoherently averaged to remove the phase variation and reduce the error.

$$Y(\tau, f, t_k) = \frac{1}{M} \sum_{q=(k-1)M}^{kM-1} |X(\tau, f, qT_I)|^2 \tag{C.2}$$

CYGNSS uses $T_I = 1$ ms and $M = 1000$. A commonly used KA-GO model relating the mean of $Y(\tau, f, t)$ to the ocean surface roughness is expressed as [1].

$$E\{Y(\tau, f, t)\} = \frac{P_t \lambda^2}{(4\pi)^3} \int\int \frac{G_t(\vec{\rho}) G_r(\vec{\rho})}{R_t^2(\vec{\rho}) R_r^2(\vec{\rho})} \left|\chi\left((\tau - \tau_s(\vec{\rho})), (f - f_s(\vec{\rho}))\right)\right|^2 \sigma_0\left(\vec{\rho}\right) d\vec{\rho}^2 + Y_n \tag{C.3}$$

where Y_n is the non-zero noise floor. The vector $\vec{\rho}$ represents a location on the mean ocean surface. $\sigma_0\left(\vec{\rho}\right)$ is the bistatic radar cross section (BRCS) of the ocean surface at this location. $\chi(\delta\tau, \delta f)$ is the ambiguity function of the GNSS signal. $\tau_s(\vec{\rho})$ is

the delay and $f_s(\vec{\rho})$ is the Doppler. $G_r(\vec{\rho})$, $G_t(\vec{\rho})$ are the receiver and transmitter antenna gains for specific locations on the ocean surface. $R_t(\vec{\rho})$ and $R_r(\vec{\rho})$ are the range between the transmitter and the mean ocean surface at the location $\vec{\rho}$, and the range between the receiver and mean ocean surface, respectively.

The observed DDM contains information about $\sigma_0(\vec{\rho})$, which is not generally invertible. In practice, one set of delay and Doppler will be mapped to two points on the ocean surface. A common approach is to constrain the retrieval within a region near the specular point and assume that the ocean roughness is uniform within this region. Under the KA-GO model, the BRCS $\sigma_0(\vec{\rho})$ can be expressed in terms of a wind-related variable, m, describing this surface, which does not vary with $\vec{\rho}$.

$$\sigma_0(\vec{\rho}, m) = \pi |\Re(\vec{\rho})|^2 \frac{q^4(\vec{\rho})}{q_z^4(\vec{\rho})} \wp_{\nabla\zeta}(\vec{s}(\vec{\rho}), m) \tag{C.4}$$

$\wp_{\nabla\zeta}(\vec{s}(\vec{\rho}), m)$ is the probability density function (PDF) of sea surface slopes evaluated at $\vec{s} = -\vec{q}_\perp / q_z$, and $\vec{q}(\vec{\rho})$ is the bisector

$$\vec{q}(\vec{\rho}) = \frac{2\pi}{\lambda}(\hat{g}(\vec{\rho}) - \hat{n}(\vec{\rho})) = \vec{q}_\perp + q_z \hat{k} \tag{C.5}$$

where $\hat{g}$ and $\hat{n}$ are unit vectors along the incident and reflected signal paths. $\vec{q}$ can be decomposed into horizontal component $\vec{q}_\perp$ and perpendicular component q_z.

C.2 Implementation

The observation equation or "forward model" in the EKF algorithm relates the state vector, $\mathbf{M}_k$, to the observation vector, $\mathbf{y}_k$, at time, t_k, which can be expressed as:

$$\mathbf{y}_k = \mathbf{h}(\mathbf{M}_k, t_k) + \epsilon_k \tag{C.6}$$

The covariance matrix of the observation error is obtained as $\mathbf{R}_k = E\left\{\epsilon_k \epsilon_k^T\right\}$. An *a priori* state estimate, $\mathbf{M}_0$, and its error covariance matrix, $\mathbf{P}_0$, are used to initialize the filter. The state vector is composed of MSS values, $M_{R,V}$, at discrete points

(R, V) within a $n_R \times n_V$ (12×12) grid at a 10-km resolution on the ocean surface, convering the entire glisening zone.

$$\mathbf{M} = \begin{bmatrix} M_{1,1} & M_{1,2} & ... & M_{1,n_V} & M_{2,1} & ... & M_{n_R,n_V} \end{bmatrix}^T \tag{C.7}$$

The observation vector, $\mathbf{y}_k$, consists of DDM samples with n_τ delay bins and n_f Doppler bins for each time step, k, with the noise floor $Y_n(t_k)$ substracted.

$$\mathbf{y}_k = \begin{bmatrix} Y(\tau_1, f_1, t_k) \\ \vdots \\ Y(\tau_1, f_{n_f}, t_k) \\ Y(\tau_2, f_1, t_k) \\ \vdots \\ Y(\tau_{n_\tau}, f_{n_f}, t_k) \end{bmatrix} - Y_n(t_k) \tag{C.8}$$

$\mathbf{h}()$ is the forward model which can be expressed as the numerical integration of (C.3) over the gridded surface wind field in $\mathbf{M}_k$, computed for each delay-Doppler pair (τ_k, f_j). The standard EKF algorithm is applied to sequentially process DDM observations, $\mathbf{y}_k$, updating the *a priori* state estimate, $\mathbf{M}_k^-$, and state error covariance, $\mathbf{P}_k^-$ to *a posteriori* state estimate, $\mathbf{M}_k^+$, and state error covariance $\mathbf{P}_k^+$. In this case, it is assumed that the wind field does not vary during the data collection period, so the state is modeled as a standard random walk process.

$$\mathbf{M}_{k+1}^- = \mathbf{M}_k^+ + \epsilon \tag{C.9}$$

$$\mathbf{P}_{k+1}^- = \mathbf{P}_k^+ + Q \tag{C.10}$$

where ϵ represents the process noise with a covariance matrix Q.

C.2.1 Forward Model

A discrete form of forward model is derived from (C.3) which converts the computation of the integral to a discrete sum over the 1 km $\times$ 1 km surface grid cells in the 90 km $\times$ 90 km surface area, represented by the indices (r, v). The state vector

$\mathbf{M}$ is composed of MSSs of 10-km grid points and the MSS vector $\mathbf{m}$ of the 1-km grid points is computed from $\mathbf{M}$ using the nearest interpolation. Each element of the forward model (C.6) can thus be expressed as the sum over the discrete surface points multiplied by the area of each cell $\Delta A = d^2$ with $d = 1000m$ in this case.

$$h(\tau_i, f_j, \mathbf{m}, t_k) = \sum_{r,v} B_{r,v}(t_k)\Xi_{r,v}(\tau_i, f_j, t_k)\wp_{\bigtriangledown\zeta}(\vec{s}_{r,v}(t_k), m_{r,v})\Delta A \tag{C.11}$$

The slope PDF is evaluated at the slope of the mid-point of each cell,

$$\vec{s}_{r,v}(t_k) = -\frac{\vec{q}_{\perp}(\vec{\rho}_{r,v}(t_k))}{q_z(\vec{\rho}_{r,v}(t_k))} \tag{C.12}$$

The MSS (i.e., the wind speed) $m_{r,v}$, the antenna gain $G(\vec{\rho})$, ranges R_t and R_r, the Fresnel reflection coefficient $\Re$, and the bisector $\vec{q}$ are all assumed uniform within the 10 km pixel. These terms will be evaluated at the mid-point of each surface pixel (r, v), and then incorporated into the computation of the coefficient $B_{r,v}(t_k)$.

$$B_{r,v}(t_k) = \frac{P_t\lambda^2}{(4\pi)^3}\frac{G_t(\vec{\rho}_{r,v}(t_k))G_r(\vec{\rho}_{r,v}(t_k))}{R_t^2(\vec{\rho}_{r,v}(t_k))R_r^2(\vec{\rho}_{r,v}(t_k))}\pi\left|\Re_{r,v}\right|^2\frac{q^4(\vec{\rho}_{r,v}(t_k))}{q_z^4(\vec{\rho}_{r,v}(t_k))} \tag{C.13}$$

where $\Xi_{r,v}$ is the power of the ambiguity function at the mid-point of each surface pixel.

$$\Xi_{r,v}(\tau_i, f_j, t_k) = \left|\chi\left((\tau_i - \tau(\vec{\rho}_{r,v}), (f_j - f(\vec{\rho}_{r,v})\right)\right|^2 \tag{C.14}$$

An isotropic normal distribution, a function of only the MSS, $m_{r,v}$, is assumed [49].

$$\wp_{\bigtriangledown\zeta}(\vec{s}_{r,v}(t_k), m_{r,v}) = \frac{1}{2\pi m_{r,v}}\exp\left(-\frac{\left|\vec{s}_{r,v}\right|^2}{2m_{r,v}}\right) \tag{C.15}$$

C.2.2 Jacobian

A partial derivative matrix $\mathbf{H}_k$ is required to update the state, $\mathbf{M}_k$, with each observation, $\mathbf{y}_k$.

$$\mathbf{H}_k = \frac{\partial\mathbf{h}(\mathbf{M}, t_k)}{\partial\mathbf{M}} \tag{C.16}$$

$\mathbf{H}_k$ is an $n_\tau n_f \times n_R n_V$ matrix for an $n_\tau \times n_f$ DDM and a $n_R \times n_V$ state of surface grid cells. The partial derivative with respect to the state vector $\mathbf{m}$ within the 1-km grid is calculated as

$$\frac{\partial h(\tau_i, f_j, \mathbf{m}, t_k)}{\partial m_{r,v}} = B_{r,v}(t_k)\Xi_{r,v}(\tau_i, f_j, t_k)\frac{\partial \wp_{\triangledown\zeta}(\vec{s}_{r,v}(t_k), m_{r,v})}{\partial m_{r,v}}\Delta A \tag{C.17}$$

Substituting (C.15), the partial derivative can be expressed as:

$$\frac{\partial h(\tau_i, f_j, \mathbf{m}, t_k)}{\partial m_{r,v}} = -B_{r,v}(t_k)\Xi_{r,v}(\tau_i, f_j, t_k)\frac{1}{2\pi m_{r,v}^2}\left(1 - \frac{|\vec{s}_{r,v}|^2}{2m_{r,v}}\right)\exp\left(-\frac{|\vec{s}_{r,v}|^2}{2m_{r,v}}\right)\Delta A \tag{C.18}$$

Since (C.18) is computationally expensive for a 1-km grid, the derivative matrix $\mathbf{H}_k$ in a 10-km grid is approximated by

$$\frac{\partial h(\tau_i, f_j, \mathbf{M}, t_k)}{\partial M_i} = 100\frac{\partial h(\tau_i, f_j, \mathbf{m}, t_k)}{\partial m_j} \tag{C.19}$$

where the term 100 is added due to the increase of the differential area from ΔA to $100\Delta A$. m_j is the nearest point to M_i in the 1-km grid.

C.3 Algorithm Summary

The state is a field of ocean surface MSS in 10 km $\times$ 10 km pixels defined in the Lat/Lon frame. Overlapping observations are processed at a rate of once per second (1 Hz). The size of the state is expanded from 10-km grid to the 1-km grid, as required by the forward model, using a nearest-neighbor interpolation Extensive testing showed that, for wind speed up to 50 m/s, convergence is reached with a 7 DDM sequence, so this number was selected as a reasonable value to assure convergence under most conditions. In addition, multiple sequences, for example one from DDM 1 to DDM 7 followed by one from DDM 2 to DDM 8 will provide different estimates of the same geo-referenced wind speed. It was found that averaging all of the wind speed estimates corresponding to the same Lat/Lon grid point reduced the total RMSE further, in comparison to a "non-overlapping" approach where only one wind speed estimate is used.

With these considerations clarified, the complete EKF-based wind retrieval algorithm is summarized below. This algorithm will operate on sequences of $n_{seq} = 7$ DDMs at a time. Required metadata includes: the receiver and transmitter positions and velocities, specular point location, incidence angle and antenna gain. At iteration $k = 0$, the *a priori* MSS $\mathbf{M}_0$ (10 km resolution) obtained from the FDS (Fully Developed Sea) estimate is used to initialize the state. Each subsequent time step, $t_k, k = 1...n_{seq} - 1$, consists of the following operations:

1. DDM observations are represented by $n_\tau n_f \times 1$ vector $\mathbf{y}_k$.

2. The 10-km resolution state vector in specular frame $\mathbf{M}_k^-$ at t_k is obtained from the state vector in lat/lon frame $\mathbf{M}_{k(ll)}^-$ using the nearest-neighbor interpolation.

3. The 10-km resolution state vector, $\mathbf{M}_k^-$, is interpolated onto the 1-km grid, $\mathbf{m}_k^-$.

4. the 1-km state vector $\mathbf{m}_k^-$ and metadata are used to evaluate the observation equation (forward model), $\mathbf{h}(\mathbf{m}_k^-, t_k)$ from Equation (C.11). Coefficients $B_{r,v}(t_k)$ is computed at the middle point of each pixel (r, v).

5. Jacobian of the forward model, from Equation (C.19) is computed using the 10-km state vector, $\mathbf{M}_k^-$. $n_p = n_R \times n_V$ is the dimension of the state.

$$\mathbf{H}_k = \begin{bmatrix} \frac{\partial h(\tau_1, f_1, \mathbf{M}_k^-, t_k)}{\partial M_1} & \cdots & \frac{\partial h(\tau_1, f_1, \mathbf{M}_k^-, t_k)}{\partial M_{n_p}} \\ \vdots & \cdots & \vdots \\ \frac{\partial h(\tau_1, f_{n_f}, \mathbf{M}_k^-, t_k)}{\partial M_1} & \cdots & \frac{\partial h(\tau_1, f_{n_f}, \mathbf{M}_k^-, t_k)}{\partial M_{n_p}} \\ \frac{\partial h(\tau_2, f_1, \mathbf{M}_k^-, t_k)}{\partial M_1} & \cdots & \frac{\partial h(\tau_2, f_1, \mathbf{M}_k^-, t_k)}{\partial M_{n_p}} \\ \vdots & \cdots & \vdots \\ \frac{\partial h(\tau_{n_\tau}, f_{n_f}, \mathbf{M}_k^-, t_k)}{\partial M_1} & \cdots & \frac{\partial h(\tau_{n_\tau}, f_{n_f}, \mathbf{M}_k^-, t_k)}{\partial M_{n_p}} \end{bmatrix}_{\mathbf{M}_k^-} \tag{C.20}$$

6. The weighted data covariance matrix, $\mathbf{R}_k$, is obtained by an empirical function evaluated with the antenna gain in the direction of the specular point.

7. The EKF update equations (C.21), (C.22) and (C.23) are applied to compute the a posteriori state vector, $\mathbf{M}_k^+$ and covariance matrix, $\mathbf{P}_k^+$.

$$\mathbf{K}_k = \mathbf{P}_k^- \mathbf{H}_k^T (\mathbf{H}_k \mathbf{P}_k^- \mathbf{H}_k^T + \mathbf{R}_k)^{-1} \tag{C.21}$$

$$\mathbf{M}_k^+ = \mathbf{M}_k^- + \mathbf{K}_k (\mathbf{y}_k - \mathbf{h}(\mathbf{M}_k^-)) \tag{C.22}$$

$$\mathbf{P}_k^+ = (\mathbf{I} - \mathbf{K}_k \mathbf{H}_k) \mathbf{P}_k^- \tag{C.23}$$

8. The *a priori* state and covariance at step $k+1$ are obtained by

$$\mathbf{M}_{k+1}^- = \mathbf{M}_k^+ \tag{C.24}$$

$$\mathbf{P}_{k+1}^- = \mathbf{P}_k^+ + Q \tag{C.25}$$

   where Q is the covariance matrix of the process noise.

9. The a prior state vector at step k in lat/lon frame $\mathbf{M}_{k+1(ll)}^-$ is obtained from the state vector in specular frame $\mathbf{M}_{k+1}^-$ using the nearest-neighbor interpolation method. Then, the algorithm returns to step (1).

At step $n_{seq} = 7$, the last estimate $\mathbf{M}_{n_{seq}(ll)}^+$, obtained from $\mathbf{M}_{n_{seq}}^+$, is converted to wind speed using the Katzberg model [12], and the final wind speed estimates in geodetic coordinates are thus obtained. A new sequence of DDMs is then processed, which will produce multiple wind speed estimates for a given latitude and longitude. These overlapping estimates are simply averaged In the current algorithm.

REFERENCES

[1] V. U. Zavorotny and A. G. Voronovich. Scattering of GPS signals from the ocean with wind remote sensing application. *IEEE Transactions on Geoscience and Remote Sensing*, 38(2):951–964, 2000.

[2] J. L Garrison, S. J Katzberg, and M. I. Hill. Effect of sea roughness on bistatically scattered range coded signals from the Global Positioning System. *Geophysical Research Letters*, 25(13):2257–2260, 1998.

[3] J. L. Garrison and S. J. Katzberg. The application of reflected GPS signals to ocean remote sensing. *Remote Sensing of Environment*, 73(2):175–187, 2000.

[4] J. L. Garrison, A. Komjathy, V. U. Zavorotny, and S. J. Katzberg. Wind speed measurement using forward scattered GPS signals. *IEEE Transactions on Geoscience and Remote Sensing*, 40(1):50–65, 2002.

[5] E. Cardellach, G. Ruffini, D. P. Gonzalez, A. Rius, A. Komjathy, and J. L. Garrison. Mediterranean Balloon Experiment: Ocean wind speed sensing from the stratosphere, using GPS reflections. *Remote Sensing of Environment*, 88:351–362, 12 2003.

[6] S. Lowe, J. Labrecque, C. Zuffada, L. J. Romans, L. Young, and G. Hajj. First spaceborne observation of an Earth-reflected GPS signal. *Radio Science*, 37:7–1, 01 2002.

[7] S. Gleason, M. Adjrad, and M. S. Unwin. Sensing ocean, ice and land reflected signals from space: Results from the UK-DMC GPS reflectometry experiment. In *Proceedings of ION GNSS 18th International Technical Meeting of the Satellite Division*, pages 1679–1685, Long Beach, CA, 2005.

[8] C. Ruf, M. Unwin, J. Dickinson, R. Rose, D. Rose, M. Vincent, and A. Lyons. CYGNSS: Enabling the future of hurricane prediction. *IEEE Geoscience and Remote Sensing Magazine*, 1(2):52–67, 2013.

[9] R. Shah, J. L. Garrison, and M. S. Grant. Demonstration of bistatic radar for ocean remote sensing using communication satellite signals. *IEEE Geoscience and Remote Sensing Letters*, 9(4):619–623, 2012.

[10] C. Cox and W. Munk. Measurement of the roughness of the sea surface from photographs of the Sun's glitter. *Journal of the Optical Society of America*, 44(11):838–850, 1954.

[11] T. M. Elfouhaily, B. Chapron, and K. Katsaros. A unified directional spectrum for long and short wind-driven waves. *Journal of Geophysical Research*, 102(C7):15781–15795, 1997.

[12] S. J. Katzberg, O. Torres, and G. Ganoe. Calibration of reflected GPS for tropical storm wind speed retrievals. *Geophysical Research Letters*, 33(18), 2006.

[13] S. J. Katzberg and J. Dunion. Comparison of reflected GPS wind speed retrievals with dropsondes in tropical cyclones. *Geophysical Research Letters*, 36(17):L17602, 2009.

[14] H. Zhang, J. L. Garrison, R. Wijekularatne, and J. G. Warnecke. S-band ocean reflectometry in high winds. In *Proceedings of 2016 IEEE International Geoscience and Remote Sensing Symposium (IGARSS)*, pages 2009–2012. IEEE, 2016.

[15] A. G. Voronovich and V. U. Zavorotny. The transition from weak to strong diffuse radar bistatic scattering from rough ocean surface. *IEEE Transactions on Antennas and Propagation*, 65(11):6029–6034, 2017.

[16] A. Voronovich and V. Zavorotny. Bistatic radar equation for signals of opportunity revisited. *IEEE Transactions on Geoscience and Remote Sensing*, 56(4):1959–1968, 2018.

[17] F. Huang, J. L. Garrison, N. Rodriguez-Alvarez, A. J. OBrien, K. M. Schoenfeldt, S. C. Ho, and H. Zhang. Sequential processing of GNSS-R delay-Doppler maps to rstimate the ocean surface wind field. *IEEE Transactions on Geoscience and Remote Sensing*, under review, 2018.

[18] M. Martin-Neira. A passive reflectometry and interferometry system (PARIS): Application to ocean altimetry. *ESA Journal*, 17(4):331–355, 1993.

[19] M. Martin-Neira, M. Caparrini, J. Font-Rossello, S. Lannelongue, and C. S. Vallmitjana. The PARIS concept: An experimental demonstration of sea surface altimetry using GPS reflected signals. *IEEE Transactions on Geoscience and Remote Sensing*, 39(1):142–150, 2001.

[20] A. Komjathy, V. U. Zavorotny, and P. Axelrad. GPS signal scattering from sea surface: Wind speed retrieval using experimental data and theoretical model. *Remote Sensing of Environment*, 73(00):162–174, 2000.

[21] A. Komjathy, D. Armatys, M.and Masters, P. Axelrad, V. Zavorotny, and S. Katzberg. Retrieval of ocean surface wind speed and wind direction using reflected GPS signals. *Journal of Atmospheric and Oceanic Technology*, 21(3):515–526, 2004.

[22] S. Gleason. *Remote sensing of ocean, ice and land surfaces using bistatically scattered GNSS signals from low Earth orbit.* Phd thesis, University of Surrey, 2006.

[23] M. P. Clarizia, C. P. Gommenginger, S. T. Gleason, M. A. Srokosz, C. Galdi, and M. Di Bisceglie. Analysis of GNSS-R delay-Doppler maps from the UK-DMC satellite over the ocean. *Geophysical Research Letters*, 36(2), 2009.

[24] D. Gebre-Egziabher and S. Gleason. *GNSS applications and methods.* Artech House, 2009.

[25] S. Gleason. Towards sea ice remote sensing with space detected GPS signals: Demonstration of technical feasibility and initial consistency check using low resolution sea ice information. *Remote Sensing*, 2(8):2017–2039, 2010.

[26] S. Gleason. Space-based GNSS scatterometry: Ocean wind sensing using an empirically calibrated model. *IEEE Transactions on Geoscience and Remote Sensing*, 51(9):4853–4863, 2013.

[27] M. Unwin, S. Duncan, P. Jales, P. Blunt, and M. Brenchley. Implementing GNSS reflectometry in space on the TechDemoSat-1 mission. In *Proc. Institute Navigation*, pages 1222–1235, 2014.

[28] C. S. Ruf, R. Atlas, P. S. Chang, M. P. Clarizia, J. L. Garrison, S. Gleason, S. J. Katzberg, Z. Jelenak, J. T. Johnson, S. J. Majumdar, et al. New ocean winds satellite mission to probe hurricanes and tropical convection. *Bulletin of the American Meteorological Society*, 97(3):385–395, 2016.

[29] M. P. Clarizia, V. Zavarotny, and C. Ruf. Level 2 wind speed retrieval algorithm theoretical basis document. *CYGNSS Project Document 148-0138*, Rev 5, 17 Aug. 2018.

[30] J. L. Garrison. A statistical model and simulator for ocean-reflected gnss signals. *IEEE Transactions on Geoscience and Remote Sensing*, 54(10):6007–6019, 2016.

[31] F. T. Ulaby, R. K. Moore, and A. K. Fung. *Microwave remote sensing: Active and passive. Volume II: Radar remote sensing and surface scattering and emission theory.* Artech House, 1986.

[32] C. A. Balanis. *Advanced engineering electromagnetics.* John Wiley & Sons, 1999.

[33] R. D. De Roo and F. T. Ulaby. Bistatic specular scattering from rough dielectric surfaces. *IEEE Transactions on Antennas and Propagation*, 42(2):220–231, 1994.

[34] P. Beckmann and A. Spizzichino. The scattering of electromagnetic waves from rough surfaces. *Norwood, MA, Artech House, Inc., 1987, 511 p.*, 1987.

[35] A. G. Voronovich. *Wave scattering from rough surfaces*, volume 17. Springer Science & Business Media, 2013.

[36] A. Voronovich. Small-slope approximation for electromagnetic wave scattering at a rough interface of two dielectric half-spaces. *Waves in random media*, 4(3):337–368, 1994.

[37] T. T. Wilheit. A model for the microwave emissivity of the ocean's surface as a function of wind speed. *IEEE Transactions on Geoscience Electronics*, 17(4):244–249, 1979.

[38] J. L. Garrison, J. K. Voo, S. H. Yueh, M. S. Grant, A. G. Fore, and J. S. Haase. Estimation of sea surface roughness effects in microwave radiometric measurements of salinity using reflected global navigation satellite system signals. *IEEE Geoscience and Remote Sensing Letters*, 8(6):1170–1174, 2011.

[39] H. Zhang, J. L. Garrison, and D. M. Burrage. Ocean Roughness and wind measurements with L- and S-band signals of opportunity (SoOp) reflectometry. In *Proceedings of 2018 IEEE International Geoscience and Remote Sensing Symposium (IGARSS)*, pages 3177–3180. IEEE, 2018.

[40] E. W. Uhlhorn, P. G. Black, J. L. Franklin, M. Goodberlet, J. Carswell, and A. S. Goldstein. Hurricane surface wind measurements from an operational stepped frequency microwave radiometer. *Monthly Weather Review*, 135(9):3070–3085, 2007.

[41] B. W. Klotz and E. W. Uhlhorn. Improved stepped frequency microwave radiometer tropical cyclone surface winds in heavy precipitation. *Journal of Atmospheric and Oceanic Technology*, 31(11):2392–2408, 2014.

[42] J. Sapp, S. Alsweiss, Z. Jelenak, and P. Chang. Stepped frequency microwave radiometer retrieval error characterization. In *Proceedings of 2017 IEEE International Geoscience and Remote Sensing Symposium (IGARSS)*, pages 271–274. IEEE, 2017.

[43] L. Bernardet, V. Tallapragada, S. Bao, S. Trahan, Y. Kwon, Q. Liu, M. Tong, M. Biswas, T. Brown, D. Stark, et al. Community support and transition of research to operations for the hurricane weather research and forecasting model. *Bulletin of the American Meteorological Society*, 96(6):953–960, 2015.

[44] J. L. Franklin, M. L. Black, and K. Valde. GPS dropwindsonde wind profiles in hurricanes and their operational implications. *Weather and Forecasting*, 18(1):32–44, 2003.

[45] C. S. Ruf, S. Gleason, and D. S. McKague. Assessment of CYGNSS wind speed retrieval uncertainty. *IEEE Journal of Selected Topics in Applied Earth Observations and Remote Sensing*, (99):1–11, 2018.

[46] A. G. Voronovich and V. U. Zavorotny. Full-polarization modeling of monostatic and bistatic radar scattering from a rough sea surface. *IEEE Transactions on Antennas and Propagation*, 62(3):1362–1371, 2014.

[47] A. G. Voronovich and V. U. Zavorotny. Theoretical model for scattering of radar signals in Ku- and C-bands from a rough sea surface with breaking waves. *Waves in Random Media*, 11(3):247–269, 2001.

[48] T. Wang, V. U. Zavorotny, J. Johnson, C. Ruf, and Y. Yi. Modeling of Sea State Conditions for Improvement of CYGNSS L2 Wind Speed Retrievals. In *Proceedings of 2018 IEEE International Geoscience and Remote Sensing Symposium (IGARSS)*, pages 8288–8291. IEEE, 2018.

[49] D. Hauser, G Caudal, S. Guimbard, and A. A. Mouche. A study of the slope probability density function of the ocean waves from radar observations. *Journal of Geophysical Research: Oceans*, 113(C2), 2008.

VITA

Han Zhang is from Liaocheng, Shandong, China, where he completed his high school education in June 2007. In 2011, he received his Bachelor's degree in Electrical Engineering from Chang'an University, Xi'an, Shaanxi, China. He was then enrolled in the Graduate School of Beihang University (formerly known as Beijing University of Aeronautics and Astronautics) for his Master's degree. During his time at Beihang, he worked under the guidance of Professor Yankong Kou. He received his Master's degree in Electrical Engineering in January 2014. In the spring and summer of 2014, he worked as an intern on software development and PC testing for two companies in Beijing. In August 2014, he went to Purdue University for his doctoral degree and joined the Radio Navigation Lab (RNL) under the supervision of Professor James L. Garrison. His research interests are in the area of new models and algorithms for remote sensing of ocean surface wind using multi-frequency signals of opportunity.